KU LEUVEN

FACULTY OF SCIENCE

Mass separation of ^{225}Ac for medical applications:

First proof of principle at CERN-MEDICIS

Michael HEINES

Supervisor: Prof. T.E. Cocolios
Institute for nuclear and radiation physics

Mentor: J.D. Johnson
Institute for nuclear and radiation physics

Thesis presented in partial fulfillment of the requirements for the degree of Master of Science in Physics

Academic year 2020-2021

Mass separation of ^{225}Ac for medical applications:

First proof of principle at CERN-MEDICIS

Michael HEINES

Examination committee:
Prof. Piet Van Duppen (chairman)
Prof. Riccardo Raabe (secretary)
Prof. Mieke De Cock
Prof. Christ Glorieux
Prof. Margriet Van Bael
Prof. Thomas Van Riet

Dissertation presented in partial fulfillment of the requirements for the degree of Master of Science in Physics

June 2021

Preface

The goal of this general research is to optimize the ^{225}Ac production using uranium and thorium targets. However, this thesis focuses on two collections performed at CERN-MEDICIS in which no such targets were present. Their goal was to study the effusion and ionization efficiency, as they provide an upper limit to the maximal achievable efficiency in future works. The ^{225}Ac obtained from the collection was laser ionized and mass separated, before being implanted on zinc-coated gold foils. These were sent to IKS for detailed activity measurements. Three different setups were used, which probed different aspects of the ^{225}Ac decay chain. Consequently independent activity measurements were obtained.

Due to the pandemic, this academic year has been turbulent for everyone. Travel restrictions and changing rules concerning the occupation in the lab and offices have impacted the Master thesis of many students. Therefore, I would like to give a special thanks to my promotor Thomas Elias Cocolios and my mentor Jake David Johnson. Both of them often pointed me in the right direction and they were always open to discuss results. Besides providing excellent guidance, they made a great effort to ensure my thesis could proceed in a matter that was as normal as possible. Furthermore, I would like to express my thanks to Charlotte Duchemin and Reinhard Heinke for performing the experimental work collections at MEDICIS. Thirdly, I want to thank the members of the Interdisciplinary Research group from IKS that helped with proofreading sections of the thesis and the experimental work on the activity measurements, in particular Wiktoria Wojtaczka and Kristof Dockx. Finally, I would like to express my gratitude towards my friends and family that listened to be rambling about my thesis contents, or even helped by reading through certain sections. Among these are my fellow Master of Physics students and flatmates Brecht Biesmans and Midas Segers, who helped me find countless errors in my code and discussed the physical understanding of some intermediate results with me.

Abstract

Due to its promise as a medical radioisotope, global demand for ^{225}Ac is beyond the current possible production rate [1, 2, 3]. Several new techniques have already been proposed to increase the production, but further research is required [1, 4]. For its use in treatment, other isotopes, that could potentially be harmful, have to be removed. This purification can be achieved with several methods, but the most promising are chemical separation and mass separation. While the former generally has a higher efficiency, the latter is known for the high isotopic purity that can be achieved with it. Within the scope of this general research lies MED-024, which is an experimental campaign that is investigating the production and mass-separation of ^{225}Ac. In this thesis, the focus will be on characterising the ISOL process efficiency of two specific collections. Both of these used a nitrate solution of ^{225}Ac, with known activity, obtained from the Joint Research center (JRC) in Karlsruhe (Germany). The first run dried the solution on a rhenium foil directly. On the other hand, the second evaporated the ^{225}Ac on a thorium-dioxide felt, where it was assumed that the ^{225}Ac would be distributed homogeneously throughout the porous target material, though without penetrating the target grains. These runs mainly concentrate on the ionization and separation efficiency of ^{225}Ac offered by the laser ionization setup at CERN-MEDICIS. Zinc-coated gold foils were implanted with mass-separated ^{225}Ac and sent to IKS for a detailed activity analysis.

Three different techniques were used to measure the activity at different times, which enabled the end of collection activity to be determined by extrapolation. These methods were single γ-ray spectroscopy, γ-γ coincidence measurements and α-spectroscopy. Each of these has its own advantages and disadvantages. For the α-spectroscopy, more accurate geometric efficiency calculations were required. For this, three models were created. The first of these is a semi-analytical method, in which the source distribution is assumed. Once the geometric efficiency is put in terms of an integral that can not be solved analytically, numerical Monte Carlo techniques were used. The other two models (NRAM and FNM) started from a more numerical basis. SRIM was used to model the stopping and redirection of α-particles and recoiling daughter nuclei within and out of the sample. The NRAM uses extrapolation of the particle trajectories in combination with assumptions on probabilities of physical processes once the particles leave the sample. The FNM, on the other hand, models the entire source-detector geometry directly.

The resulting collection efficiencies were equal to 9.77(19) % for the first collection and 8.99(48) % for the second. These are only lower bounds to the best achievable efficiency, as the optimization of the setup was performed during the collection and the samples were temporarily removed for mass scans. Furthermore, the second collection had to be ended before saturation was reached. The results from the second run indicate that the effusion efficiency is negligible.

Layman Summary

As many diseases have become easier to treat due to advancements in modern medicine, cancer has become one of the leading causes of death. Almost 10 million people die of cancer every year, from which approximately 90% are caused by so-called micrometastatic cancers. Currently, these types of cancers are treated with chemotherapy or radiation treatment based on β-emitters. These methods take a heavy toll on patients and are not always effective. Even while using specialized techniques, radiation therapy damages a lot of healthy cells. However, a promising technique is to use α-emitting atoms instead, as the cell damage is 1000 times more localized. These α-emitters can be coupled to *targeting molecules* that preferentially attach to the cancer cells. These molecules circulate through the body until it finds the cancer cells and latches on to it. By doing this, the radiation can be targeted directly to the cancer cell. Using this technique, the healthy cells remain nearly unaffected. There are several radioactive elements that are potential candidates, among which is actinium-225 (^{225}Ac), which will be the main focus of this thesis. While promising results have been obtained, there are some issues left to be resolved.

One of these problems is that the supply is insufficient to treat many patients. If this radioactive element is to be used, alternative production methods have to be explored. Several methods have been proposed based on irradiating specific targets with protons to achieve reasonable amounts of this element. However, other isotopes (same element with different amounts of neutrons), that can potentially be harmful, are also produced. Therefore, these should be separated from the desired material. In this general research, the focus lies on the proton irradiation of uranium and thorium targets. However, no such target was present during the experiments discussed in this thesis. After this irradiation, the radioactive material has to be extracted from the target. By heating the target, the radioactive elements are effused. Next, the unwanted isotopes can be removed by using lasers and a big magnet, before they are *caught* on a sample. The main focus of this thesis was on measuring what fraction can be recovered from the separation process.

The collections discussed in this thesis only reflect part of the separation process, which is why it will in future research provide an upper limit of the fraction that can be extracted. By measuring the activity of the samples, it is possible to infer how much of the isotope was caught. Three different methods were used to accurately determine how much activity was present, such that this number could be compared with the amount that was put in the setup. By comparing these values with how much was present at the start, the recovered fraction can be calculated. It was concluded that 9.77(19)% and 8.99(48)% of the radioactive element of interest was collected on the foil in the first and second collection respectively.

List of abreviations

- ADC: Analog-to-Digital Convertor
- CERN: European Council for Nuclear Research
- DAQ: Data Acquisition system
- EOC: End Of Collection
- FNM: Full Numerical Model
- HPGe: High purity germanium
- IKS: Institute for nuclear and radiation physics
- ISOL: Isotope Separation On Line
- ISOLDE: Isotope Seperator On Line Device
- ITER: International Thermonuclear Experimental Reactor
- JRC: Joint Research Center
- MEDICIS: Medical Isotopes Collected from ISOLDE
- NRAM: Numerical Recoil Analysis Model
- PA: Preamplifier
- PET: Positron Emission Tomography
- PIPS: Passivated Implanted Planer Silicon
- PSB: Proton synchrotron booster
- RNG: Random Number Generator
- SA: Shaping Amplifier
- SRIM: Stopping Range of Ions in Matter
- SSSM: SRIM Supporting Software Module
- TAT: targeted alpha therapy

Contents

1 Introduction

Ever since their discovery, radioactive isotopes have played a large role in both modern applications, for example in the medical field, and techniques that can be used in fundamental research. From the unveiling of the nucleus by Rutherford to the parity violation of madame Wu, these isotopes have allowed scientists to develop an understanding of what happens on the scale of the nucleus. In turn, the nucleus has proven to be a remarkably good probe for fundamental physics, in particular the strong interaction. This knowledge has allowed many applications to arise over the years for both research purposes and societal use. The former consists of techniques such as emission channeling, while the latter consists mostly of energy production and medical applications. On the side of energy production, the production share coming from nuclear fission has decreased steadily over the last 20 years. Even so, it is still responsible for a major part of energy production. In 2020, nuclear fission was responsible for 23.25% of the electricity production in Europe, and 39.33% in Belgium. These values were once as high as 30.78% in Europe (1996), and 67.14% in Belgium (1986) [5]. Projects such as thorium reactors and nuclear fusion reactors (ITER, expected to finish construction in 2025) could in the future provide the world with a source of nearly limitless clean energy produced with no to very little waste [6, 7]. Medical applications on the other hand, such as PET scans and radiation therapy, are currently indispensable. One of the most common examples of the latter is the use of β-emitters for radio-immunotherapy. After using this for many years, it was only in 1995 that an α-emitter was first used in a patient. If the state-of-the-art research continues, this sector could very well rely even more on radioactive isotopes in the future. A lot of promise lies in treating certain distributed cancers with using α-emitters, which is referred to as Targeted Alpha Therapy (TAT).

In contrast to current radiation therapies, in which mainly β- or γ-radiation is applied from outside the body, TAT couples a radioactive isotope to a targeting molecule and attacks cancerous cells from inside of the body. These molecules can be anti-bodies or peptides that have preferential binding to the cells of interest. When the molecules circulate in the lymph or cardiovascular system, they bind to the receptors of the cells of interest and are subsequently internalized. The circulation time and bio-distribution is referred to as pharmacokinetics. As α-particles transfer their energy in a very short range, the micrometastases receive a large dose while the neighbouring healthy cells only receive a minor dose. This is also the exact reason why α-particles are not used to radiate from outside the body. The small penetration depth would leave the cancer cells nearly unaffected, while the healthy cells would sustain a lot of damage. Due to the high probability of double strand breaks to cell DNA caused by the alpha emitters, reproduction of these cells is prevented. The chemical knowledge and control of molecules has reached a stage in which these targeting molecules can be relatively well created and controlled. However, this requires an adequate amount of knowledge about the isotope or molecule that it needs to couple to [1]. Due to several complications, the choice of radioactive isotope is rather tricky.

Two main aspects determine if the isotope is suitable, namely the lifetime and the toxicity of the isotope and its daughter nuclei. If the lifetime is too short compared to the time required for pharmacokinetics, the isotope will decay before it reaches the cancer cell, thus only damaging healthy cells. On the other hand, very long lifetimes imply that a larger amount of the material is required for the same activity. This also increases the dose to the patient as the radioactive material may remain in the body for a longer time. If the activity is not sufficiently high, the cancer cells will be able to repair and reproduce faster than that they are destroyed. Besides that, the radio-ligand complex will have a higher probability of breaking down after a certain time. Thus using a radio-isotope with a long lifetime increases the chances that the isotope will break free and accumulate in undesirable places in the body due to biological transport mechanisms.

The concept of toxicity is also important, as the isotope would damage the parts of the body it travels through after decaying. Besides the main isotopes, its daughter nuclei should also satisfy the second condition, implying that none of the significant branchings should lead to toxic byproducts. The lifetime of the daughter nuclei does not have to be as long, as those decays will barely occur in the journey to the cell. As it turns out, not many α-decaying isotopes satisfy these conditions, leaving only a handful of possibilities. With a half-life of 9.92 days, ^{225}Ac is a suitable candidate and is the focus of this thesis. In its decay chain, four consecutive α-decays and two β-decays occur, which makes it more effective against cancer cells. Besides that, ^{225}Ac is a generator of ^{213}Bi, which itself is a promising candidate for TAT [8]. Although limited by the supply of this isotope, several studies have managed to bind ^{225}Ac to ligands such as forms of acetic acid resulting in a stable complex [1, 9, 10]. Preclinical studies using ^{225}Ac have obtained remarkable results, in particular for castration-resistant metastatic prostate cancer [2, 3]. Even though the results are promising, a lot of work is still needed to treat all micrometastatic cancers, which contribute to 90% of global cancer deaths. Furthermore, large-scale clinical trials have only been performed on a ^{223}Ra-based TAT, for which $^{223}RaCl_2$ is FDA approved (Xofigo) [11, 12].

Besides the use as a medical isotope, actinium is also one of the isotopic chains that can be used for nuclear structure research. There are indications that certain heavy exotic nuclei, including ^{225}Ac, undergo electric octupole deformation (pear-shaped nuclei). In nuclei for which such an octupole deformation is present, any possible electric dipole moment is expected to be amplified. This would be useful for the study of charge-parity violation implying physics beyond the standard model [13]. Besides that, an inverted odd-even staggering occurs in the charge radii, which might be linked to the octupole shape [14]. The results of these studies on the actinium isotopic chain could provide adaptations to the current nuclear models or even to the current standard model [1].

There are two main factors that limit the progress of further development on the work on ^{225}Ac. The first is its purification of co-produced isotopes (either stable or unstable) [15]. Different actinium isotopes that cannot be easily removed, such as ^{227}Ac, could cause major drawbacks for medical applications. First of all, the toxicity is a necessary point of investigation. More importantly, the isotopes impact on waste handling prevents the use of Ac-based radiopharmaceuticals in Europe, unless the product is free of ^{227}Ac [1]. The second issue lies in the production of the isotope. Currently, there is only a very small amount of ^{225}Ac available, which is mostly eluted from ^{233}U-stocks [1]. More is required if it is to be used for the treatment of several frequently occurring cancers. With the current supply, less than 1000 patients could be treated per year, which would make even clinical trials difficult to perform [1]. While current production is largely based on extraction from ^{233}U, several other production paths are currently being explored. Many of the most promising techniques are based on irradiation of ^{226}Ra targets with low energy protons to create ^{225}Ra, which is in turn a parent nucleus of ^{225}Ac (half-life of 14.9 days) [1, 4].

In this general research, the goal is to investigate the production and purity of ^{225}Ac obtained by another promising method, namely high-energy proton irradiation of thorium or uranium targets. For the purification purposes, the ISOL method was chosen for its high isotopic purity. However, this will induce a series of losses. First of all, there are losses from diffusion and effusion out of the thick target, followed by ionization losses. Finally, there are some minimal losses in the beam transport following the ionization. If this method is to be used for the production of ^{225}Ac, the losses should not reduce the activity significantly compared to other methods (such as radiochemical separation). Within the general research looking into optimisation of the production of ^{225}Ac lies MED-024, which focuses on the ionization efficiency. While the efficiency will be studied in this thesis, no definite result on the isotopic purity could be provided, as no ^{227}Ac was present during the collections. To obtain the collection efficiency, the activities of the obtained samples had to be measured. To do this, three measurement techniques were used, namely single γ-ray spectroscopy (lead castle setup), γ-γ coincidence measurements (coincidence setup) and α-spectroscopy of a long decay chain (α-chamber setup).

outline

In Chapter 2, the preparation of the samples at MEDICIS will be discussed, followed by a brief overview of the spectroscopy techniques applied at IKS in Chapter 3. In Chapter 4, the single γ-ray spectroscopy will be discussed. After this, Chapter 5 will treat the γ-γ coincidence measurements. Following this, the α-spectroscopy is discussed together with the calculations and simulations for its geometric efficiency in Chapter 6. Finally, the results obtained from the different experimental techniques are compared in Chapter 7 and a short conclusion is given in Chapter 8. All of the code written for this thesis can be found on Github [16].

2 ^{225}Ac Mass Separation at CERN-MEDICIS

During standard on-line production, the general procedure of isotope collection at MEDICIS consists of four major steps. The first step is to create the isotope of interest. For the operation of ISOLDE, the Proton Synchrotron Booster (PSB) provides about 50% of its high energy ($1.4\,GeV$) protons in the form of a beam with intensity up to $2\mu A$. These subsequently impinge on the specially-developed ISOLDE targets to induce spallation, fission and fragmentation reactions. While some protons participate in these reactions, most are unaffected and thus pass through the target [17]. To utilize these remaining protons, a parasitic target can be placed approximately $500\,mm$ behind the ISOLDE targets. This process can be used to create radioactive isotopes that remain in the target. The parasitic target is kept in that position for a couple of hours, depending on the used target and the desired isotopes. After this, the target, containing the produced isotopes and their daughter nuclei is moved by a Kuka robotic arm to the MEDICIS frontend.

This entire first step was not performed for MED-024. During the CERN Long Shutdown 2 (2019-2020), MEDICIS accepted external sources, that did not require the usual radiation, for ionization and mass separation experiments. For MED-024, external sources with known activities were used. The ^{225}Ac was deposited onto a thin rhenium foil within a tantalum boat. This is subsequently loaded into the tantalum target container, which in turn is inside the target unit. A picture of the target container inside the target unit is shown in Figure 2.1 (a). In both runs performed during this campaign, a nitrate solution of ^{225}Ac was obtained from eluting a ^{229}Th generator at JRC Karlsruhe (Germany). For the first run, this solution was dried on the rhenium foil directly. For the second run, the eluant was evaporated in a ThO_2 felt. It was thought that the ^{225}Ac was well-distributed within the ThO_2 microstructure, although it was assumed that the ^{225}Ac did not penetrate into the target grains during the process. After these procedures, the target boats were sent to MEDICIS for the collection of mass-separated ^{225}Ac.

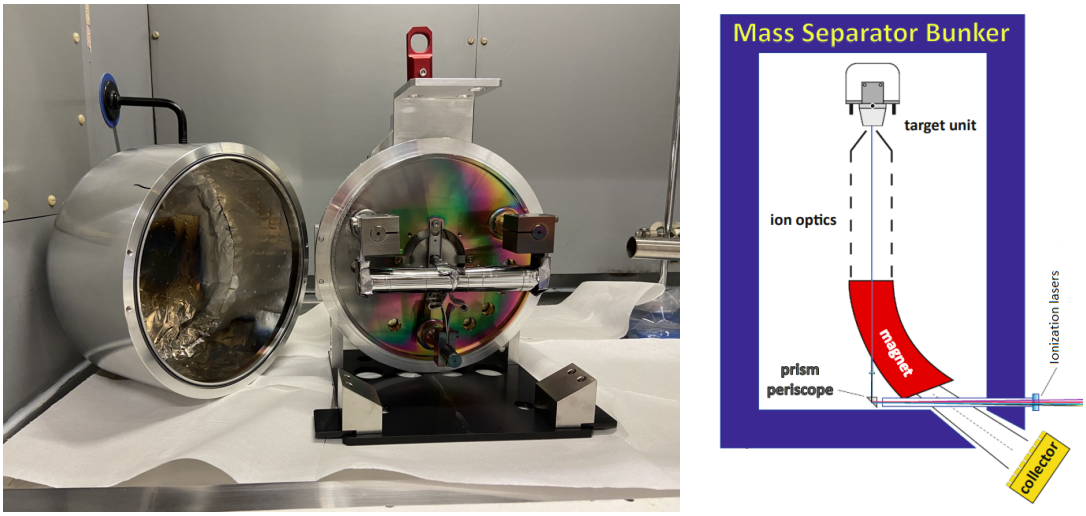

(a) (b)

Figure 2.1: (a) Picture of the target on a sample boat and (b) The used experimental setup for mass separation at MEDICIS, adapted from [18].

During the collection the second step can be initiated, namely creating an atomic vapor. The target is heated such that the radioactive isotopes effuse out of the target (if one is present). Subsequently, the isotopes migrate towards an ion source via a heated transfer line. The third step is to use lasers to ionize the ^{225}Ac. To do this, the elements are selectively ionized using three lasers, of wavenumbers 22801.1, 23545.9 and 21992.7 nm^{-2}, corresponding to wavelengths in the near UV. While the first laser is used for a ground step excitation, the other two excite the atoms into autoionizing states. The final step is to mass separate the isotopes using a dipole magnet and implant them on a sample. To do this, the ions are first accelerated by a $60V$ electrode. By sending the isotopes through a magnetic field, they can be mass separated, providing an isotopically pure beam. After this, the isotopes of interest can be implanted on the sample(s) of interest, which in this case were zinc-coated gold foils. A graphic representation of the experimental setup shown in Figure 2.1 (b).

For the first run, 30 MBq of ^{225}Ac has been eluted on 19/10/2020, while the second run eluted 15 MBq on 30/11/2020. Both of these had a purity of over 99.98% as measured by γ spectroscopy at the Joint Research Center (JRC) of the European Commission. While the initial activity was higher for the first run, the time between the elution and the collection was also longer. At the time of the collection, the activities were 10.6 and 9.33 MBq for the first and second runs respectively. While the exact details of the beam current obtained for a specific temperature goes beyond the scope of this thesis, an important result was that the second run required a significantly higher temperature to get the ^{225}Ac out of the target. The first collection used applied electric currents between 600-720 A, corresponding to 1920-2275°C showing a significant beam current before the start of the actual collection at about 500 A. The major part of the collection was performed at 1920° for the implantation of the M108 sample, while the applied electric current was increased to 2275° for the M118 sample. On the other hand, the second run required electric currents between 630-810 A, corresponding to 1980-2460°C. For this collection, a significant beam current appeared only at 790 A (2400°). The currents used to heat the targets were increased over time for both collections. A total of three samples were made over the collections, two for the first one (M108 and M118) and one for the second (M120). For the transport of the foils to the Institute for nuclear and radiation physics (IKS), a brief measurement had to be made of the activities by radioprotection. These provided the activities and collection efficiencies shown in Table 2.1. It should be noted that these do not correspond to the values for the activity at the end of the collection. The first collection samples were measured about a day and two days for the M118 and M108 respectively, while the second collection sample (M120) was measured less than an hour after the end of the collection (EOC).

Table 2.1: Initial estimates of the sample activities, obtained by γ-spectroscopy using the 218 keV energy peak from ^{221}Fr performed by CERN γ-spec.

Foil	EOC Time	γ-spec Time	Activity (kBq)	Efficiency at measurement (%)	Efficiency at collection (%)
M108	4 Nov 11:00	6 Nov 9:51	947(72)	8.90(68)	10.18(78)
M118	5 Nov 13:40	6 Nov 8:51	65.0(50)	0.65(5)	0.69(6)
M120	9 Dec 15:00	9 Dec 15:42	813(62)	8.71(67)	8.77(67)

Besides this, the activity was monitored on-line by a Kromek detector placed in the collection chamber and by measuring the ion current. The Kromek detector is a semi-conducting crystal that detects γ-radiation without the need for cryogenic cooling. In these measurements, it measured the 440 keV energy peak from ^{213}Bi. The ^{225}Ac activity from the integrated ion currents and ^{213}Bi activity as measured by the Kromek detector are shown in Figure 2.2. The sole purpose of these measurements was to indicate when the activity became saturated. The latter did not happen in the second collection, as it had to be ended prematurely.

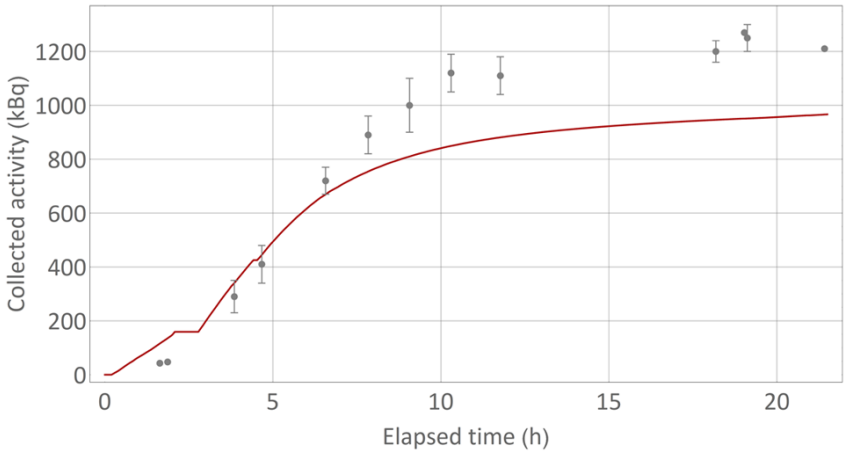

(a)

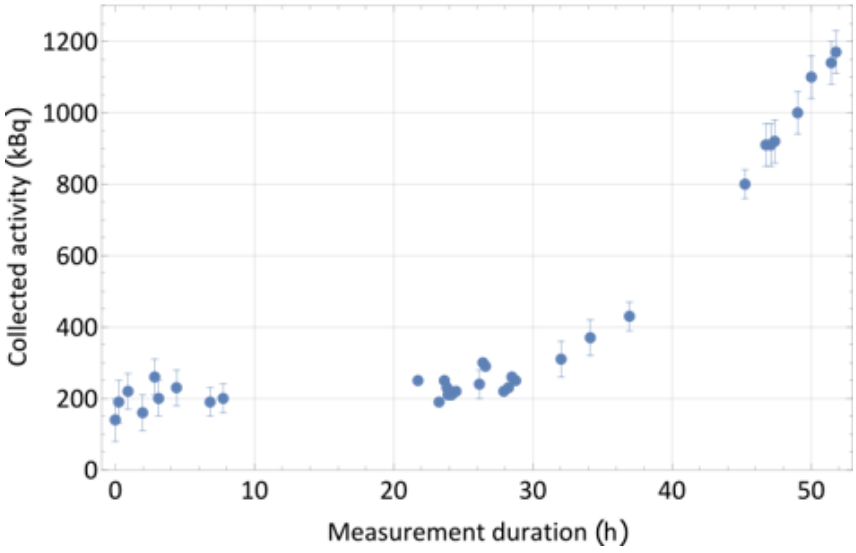

(b)

Figure 2.2: Activity measurements of (a) the first collection, using both the Kromek detector and integrated ion currents and (b) the second collection using only the Kromek detector.

After some initial time, in which optimization was performed, the activity starts to increase. For the first run, the activity had saturated after approximately 20 hours of collecting and subsequently the collection was stopped. As the second run required longer to optimize, it did not saturate.

3 Spectroscopy of the ^{225}Ac Decay Chain

The experimental work at IKS was mainly focused on measuring this activity more accurately using different techniques to avoid systematic errors. For this, three different experimental setups were used to independently measure the activity of ^{225}Ac obtained from MEDICIS. Although ^{225}Ac itself decays almost exclusively via α-decay, there are a number of γ lines throughout the chain which allow for γ-spectroscopy techniques to be used. The decay chain of ^{225}Ac is shown in Figure 3.1 while some more information on the present isotopes is provided in Table 3.1. ^{209}Bi is essentially stable, as its half-life is roughly one billion times the age of the universe. To even prove that it is not stable, De Marcillac et al. had to cool $Bi_4Ge_3O_{12}$ detectors down to 20 mK [19].

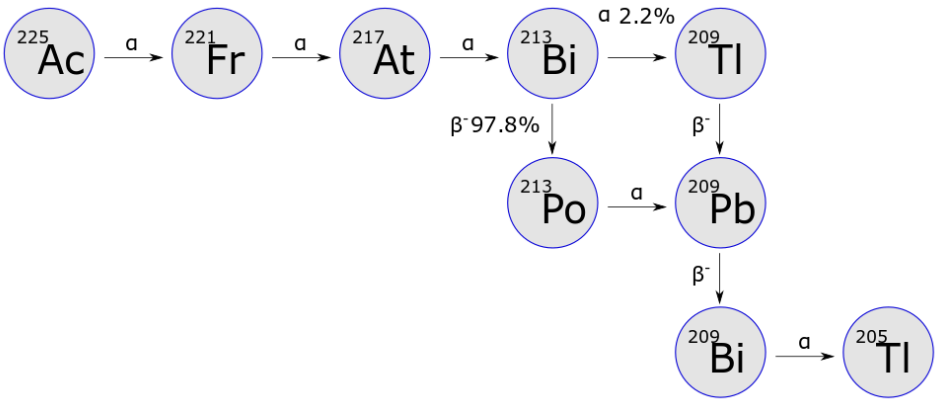

Figure 3.1: The decay chain for ^{225}Ac.

Table 3.1: Information about the present isotopes

Isotope	Half-life	Dominant decay
^{225}Ac	9.9203(3) d	α
^{221}Fr	4.9(2) m	α
^{217}At	32.3(4) ms	α
^{213}Bi	45.59(6) m	β
^{209}Tl	2.162(7) m	β
^{213}Po	3.72(2) μs	α
^{209}Pb	3.234(7) h	β
^{209}Bi	2.01(8) $\times 10^{19}$ y	α
^{205}Tl	/	Stable

Two of the setups focused on the γ-particles emitted by the daughter isotopes. One of these was the *lead castle setup*, which measures γ radiation with a very low background environment using a high purity germanium (HPGe) detector. For the analysis, two major peaks were chosen. The first is the 218.12(2) keV peak with an intensity of 11.4(3)% following the decay of ^{221}Fr to an excited state of ^{217}At via α-decay. The second peak of interest is the 440.45(1) keV peak with an intensity of 25.49(15)% following the β-decay of ^{213}Bi.

Besides this, the *coincidence setup* was used to measure peaks that occur in coincidence with efficiency-free activity measurements using two HPGe detectors. Two sets of coincidences were chosen for the analysis. The first consists of an 807.36(1) keV and a 292.80(1) keV photon following the β-decay of ^{213}Bi [20]. This occurs in approximately 0.2% of the decays. The second set of coincidences consists of the 465.14(1) keV and a 1567.08(2) keV photon following the β-decay of ^{209}Tl [21]. While this provides a coincidence in approximately 96% of the decays, the low branching for α-decay from ^{213}Bi towards ^{209}Tl decreases this to 2.1%. Furthemore, the lower detection efficiency at the higher energies decrease the relative number of coincidences by roughly a factor 2. The intensities for individual and coincidence γ-radiation are shown in Table 3.2. Here I_{12} is calculated by multiplying I_1 with $\frac{I_2}{I_{in}}$, where I_{in} is the branching running towards the state (including electron conversion).

Table 3.2: γ energies and intensities for the coincidences of interest. For ^{209}Tl, the intensities were calculated using the electron conversion coefficients.

Isotope	E_1 (keV)	E_2 (keV)	I_1 (%)	I_2 (%)	I_{12} (%)	$I_{12}/(I_1 I_2)$
^{213}Bi	807.36(1)	292.80(1)	0.292(12)	0.429(7)	0.216(14)	173(14)
^{209}Tl	465.14(1)	1567.08(2)	96.0(11)	99.663(7)	95.7(11)	1.00(2)

Lastly, the α-*chamber setup* was used to perform α spectroscopy using a Passivated Implanted Planar Silicon (PIPS) detector. The most significant α-intensities and their corresponding energies are shown in Table 3.3.

Table 3.3: Most significant α-intensities and energies for the most significant finestructure decays [20, 22, 23, 24].

^{225}Ac Intensity (%)	50.7(15)	18.1(20)	9.32(12)	8.6(9)
^{225}Ac α-Energy (keV)	5830(2)	5792.5(22)	5732(2)	5790.6(22)
^{221}Fr Intensity (%)	83.3(7)	15.1(2)	/	/
^{221}Fr α-Energy (keV)	6341.0(13)	6126.3(15)	/	/
^{217}At Intensity (%)	99.9(1)	/	/	/
^{217}At α-Energy (keV)	7066.9(16)	/	/	/
^{213}Bi Intensity (%)	91.55(11)	8.45(11)	/	/
^{213}Bi α-Energy (keV)	5875(4)	5558(4)	/	/
^{213}Po Intensity (%)	100	/	/	/
^{213}Po α-Energy (keV)	8376(3)	/	/	/

As the α-particle energies following the decays of ^{225}Ac and ^{213}Bi are too similar to be resolved, the the focus of the analysis was on the α-particle energies following the decays of ^{221}Fr, ^{217}At and ^{213}Po. As a point source approximation is not sufficient for these measurements, additional models had to be made. These consisted of both semi-analytical models and numerical models, whose main purpose was to properly characterize the geometric efficiency of the setup. These are possibly different for the individual isotopes.

Even though saturation has been reached at the time of the measurements, the activity of the different isotopes is not entirely the same. To obtain the ^{225}Ac activity, a purely physical correction factor comes into play. The activity of the daughter isotopes lags behind slightly, causing it to be higher than that of the parent nucleus. This result is known as Bateman's equations which in saturation are given by Eq. (3.1). Here A_i and τ_i denote the activity and the half-life of the i'th nucleus in the chain respectively. The relation for the activity fractions between daughter and parent nuclei was first proven by Harry Bateman in 1908 [25]. It can be obtained by taking the Laplace transform of the rate equations. However, the proof will not be given here. The Bateman correction factors for all the present isotopes are shown in Table 3.4.

$$\frac{A_D}{A_1} = \prod_{i=2}^{D} \frac{\tau_1}{\tau_1 - \tau_i} \tag{3.1}$$

Table 3.4: Bateman correction factors for the present isotopes.

Isotope	Bateman correction
^{225}Ac	1
^{221}Fr	1.00034(8)
^{217}At	1.00034(14)
^{213}Bi	1.00355(20)
^{213}Po	1.00355(27)
^{209}Tl	1.00370(33)
^{209}Pb	1.01752(42)

The correction factors are generally negligible and only increase significantly at 2 specific isotopes, namely ^{213}Bi and ^{209}Pb, because their lifetimes are significantly larger than the other daughter isotopes. Another observation is that the error increases as later isotopes in the decay chain are studied. Again, this is expected, as it becomes dependent on the half-lives of all preceding decays. Besides that, a determination of the times of the measurement has to be obtained. Certain measurements were made over several hours, and in some cases even nearly entire days. Even though the lifetime of the isotope is rather large (9.92 days), a less accurate method would be to simply take the median time for the measurement. As the decay is exponential, the mean time will be larger than the median time. A short derivation for the value of the mean time as a function of the initial time and measurement time is given in Appendix A. The particularities of the spectroscopy setups will now be discussed in more detail.

4 Single γ-ray Spectroscopy in a Lead Castle

4.1 Concepts and Calibration

4.1.1 Experimental setup

A lead castle setup is an ideal environment for the measurement of strong energy peaks as the background is minimal. The concept is that a sample is put at a fixed distance from a detector surrounded by lead shielding. This way, natural/background effects are minimized. The particular setup used HPGe detectors with integrated preamplifiers, which are cooled with liquid nitrogen to reduce noise to very low levels. A picture of the lead castle and a schematic overview of a similar detector (different model but from the same manufacturer) is shown in Figure 4.1. The detector in the lead castle setup used a vertical pointing crystal instead of a horizontal one.

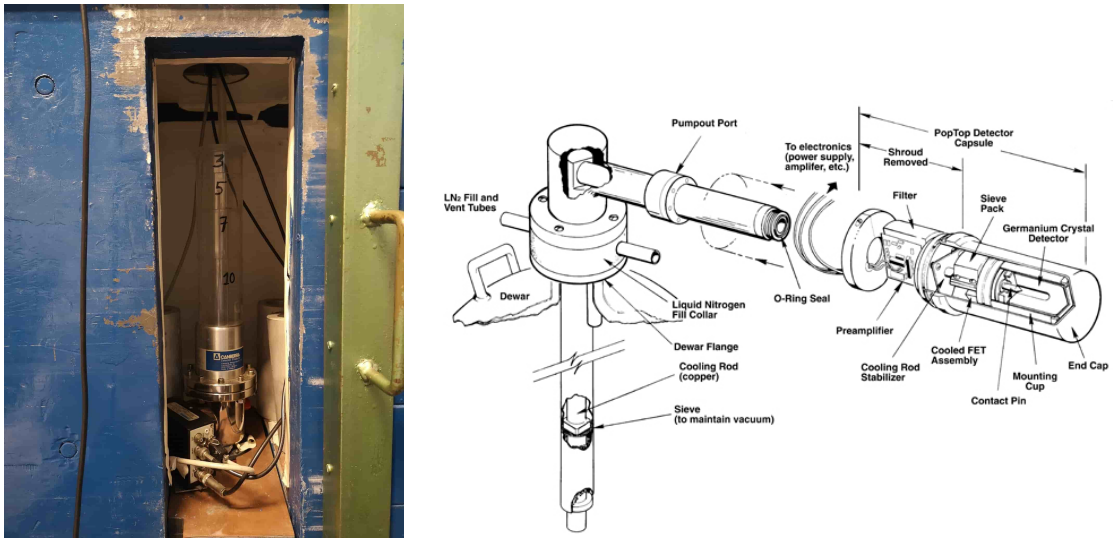

(a) (b)

Figure 4.1: a) Picture of the lead castle setup, showing the detector inside the lead shielding and b) Graphic representation of a similar HPGe detector [26].

It is also possible to examine small peaks, but these will provide worse statistics and are sometimes even suppressed by the Compton continuum of other peaks. In this setup, a sample was placed at a fixed distance and the spectra were measured over several hours to obtain sufficient statistics. As this technique assumes a constant activity over the measurement period, the measurement time should be sufficiently small compared to the half-life of the parent nucleus (^{225}Ac). The latter is because analog electronics do not keep information about the specific events, but only the spectrum over a given period. For our measurement, this half-life is 9.92 days, which allows long measurements without reducing the accuracy significantly.

In order to obtain the actual activity, a series of steps needs to be taken. First, an energy calibration has to be made, in order to convert the channel numbers from the spectrum into actual energy units using known ^{133}Ba, ^{60}Co and ^{152}Eu sources. After that, the total efficiency response of the detector has to be estimated as a function of energy, which again uses these known sources. Subsequently, the background is subtracted, which takes into account the natural radioactivity remaining in the spectrum. In reality, this fluctuates a bit with the weather, but this effect is rather small. After this, the count rates can be obtained by using a Gaussian fitting on linear background for the peaks of interest. The units of the fitting parameters should be in channel numbers, as otherwise the bins would be discarded. Furthermore, additional correction factors can be introduced which deal with imperfections of the setup. The final obtained activity for a single peak (A_E) at energy E is then given by Eq. (4.1). Here σ_E and N_E denote the standard deviation and height of a single peak at energy E obtained by fitting on the background-subtracted spectrum. Furthermore, ε_E denotes the efficiency at a given energy and c_i is the i'th correction factor.

$$A_E = \frac{\sqrt{2\pi}\sigma N_E}{\varepsilon_E} \prod_i c_i \tag{4.1}$$

This setup used an analog data acquisition system (DAQ) using the electronic scheme shown in Figure 4.2. The preamplifier (PA) is directly coupled to the detector. Following this, the signal is altered by a shaping amplifier (SA) which transforms the pulses to near Gaussian shapes before being sent into an analog-to-digital converter (ADC). Finally, the signal is interpreted by the computer. The evolution of the pulse shape is shown above the electronic scheme. For safety reasons, the substrate itself was kept in a vial. This way, contamination risks are reduced while particles that recoil out of the substrate are stopped in the glass. Unless specifically mentioned otherwise, the measurements were performed with the amplifier set to a gain of 20 and a shaping time of 2 μs. The gain is chosen such that the peaks of interest, as well as most of the calibration peaks, are visible in the spectrum. Small gains allow a larger energy range to be visible, but also cause the number of bins at a specific energy to be lower. The choice of shaping time should maximize the Gaussian shape of the peaks, which was determined by students in the scope of the *Research Methods in Nuclear Physics* course.

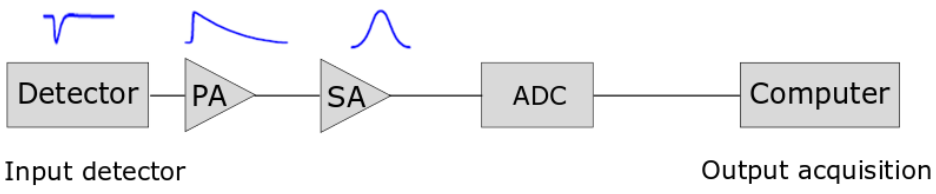

Figure 4.2: Electronic scheme of the lead castle setup. The detector signal is fed into a PA directly. After this, it is shaped by a SA before having its energy analyzed by an ADC. Finally, the energy spectrum is sent to the computer. The pulses were adapted from [27].

4.1.2 Energy Calibration

The distance from the edge of the detector to the bottom of the vial, was ($25 \pm 0.01\,cm$), which is obtained by stacking small plastic rings on top of each other. Even though this distance is relatively well known, the distance from the edge of the detector to the germanium crystal is not well documented. Schematics of a very similar detector of the same manufacturer provide 0.5 cm, which will be assumed to be the same as for the used detector. At the time of the calibration measurements, the ^{133}Ba, ^{60}Co and ^{152}Eu sources had activities of 27.600 kBq, 10.556 kBq and 26.430 kBq with uncertainties of 3%, 4.8% and 10% respectively. However, since the ^{60}Co source provided a clear systematic shift in the efficiency response compared to the other sources, it was remeasured. This was done using efficiency free activity measurements, as discussed in Chapter 5. The new determined activity was 19.9 kBq with a relative uncertainty of 3.4%. While the ^{133}Ba and ^{60}Co sources only undergo β-decay, ^{152}Eu also has γ radiation following electron capture. The theoretical data on the used calibration peaks is given in Table 4.1 together with a number assignment for easier representation.

Table 4.1: Theoretical data and emitted count rate for the calibration peaks.

Peak number	Energy (keV)	Intensity (%)	Origin	Emitted count rate (kBq)
1	80.9979(11)	32.9(3)	^{133}Baβ^+	9.08(36)
2	121.7817(3)	28.53(16)	^{152}EuEC	7.54(41)
3	244.6974(8)	7.55(4)	^{152}EuEC	2.00(11)
4	276.3989(12)	7.16(5)	^{133}Baβ^+	1.976(74)
5	302.8508(5)	18.34(13)	^{133}Baβ^+	5.06(19)
6	344.2785(12)	26.59(20)	^{152}Euβ^-	7.03(39)
7	356.0129(7)	62.05(19)	^{133}Baβ^+	17.13(57)
8	383.8485(12)	8.94(6)	^{133}Baβ^+	2.467(91)
9	411.1165(12)	2.237(13)	^{152}Euβ^-	0.591(32)
10	443.9606(16)	2.827(14)	^{152}EuEC	0.747(40)
11	778.9045(24)	12.93(8)	^{152}Euβ^-	3.42(19)
12	867.380(3)	4.23(3)	^{152}EuEC	1.118(62)
13	964.057(5)	14.51(7)	^{152}EuEC	3.83(21)
14	1085.837(10)	10.11(5)	^{152}EuEC	2.67(15)
15	1112.076(3)	13.67(8)	^{152}EuEC	3.61(20)
16	1173.228(3)	99.85(3)	^{60}Coβ^+	19.87(70)
17	1332.492(4)	99.9826(3)	^{60}Coβ^+	19.90(69)
18	1408.013(3)	21.90(9)	^{152}EuEC	5.52(29)

The fitting procedure was performed by restricting the domain around the peak and fitting the remaining spectrum to a Gaussian + Linear background model. Obtained peak positions and absolute efficiencies are shown in Table 4.2, while the most important parts of the calibration spectra are shown in Figure 4.3.

Table 4.2: Data obtained from fitting the spectrum around a peak using a Gaussian + Linear fitting model. The peak number corresponds to those indicated in the spectra.

Peak number	Channel	Countrate (/s)	Total efficiency (%)
1	/	5.87(16)	0.0646(43)
2	/	8.335(48)	0.1105(65)
3	171.599(7)	1.76(2)	0.0882(57)
4	223.476(5)	1.63(2)	0.0825(41)
5	266.777(4)	3.85(3)	0.0761(35)
6	334.581(5)	4.589(3)	0.0653(37)
7	353.768(3)	11.12(6)	0.0649(25)
8	399.325(7)	1.51(2)	0.0612(31)
9	444.01(3)	0.34(2)	0.0575(65)
10	497.83(2)	0.43(1)	0.0570(44)
11	1046.25(1)	1.02(2)	0.0298(23)
12	1191.05(3)	0.303(9)	0.0271(23)
13	1349.589(9)	0.95(2)	0.0248(19)
14	1549.13(4)	0.61(4)	0.0228(28)
15	1591.98(2)	0.78(1)	0.0216(15)
16	1692.073(4)	3.81(2)	0.01915(63)
17	1953.032(4)	3.42(2)	0.01716(58)
18	2076.771(5)	0.9856(5)	0.01787(95)

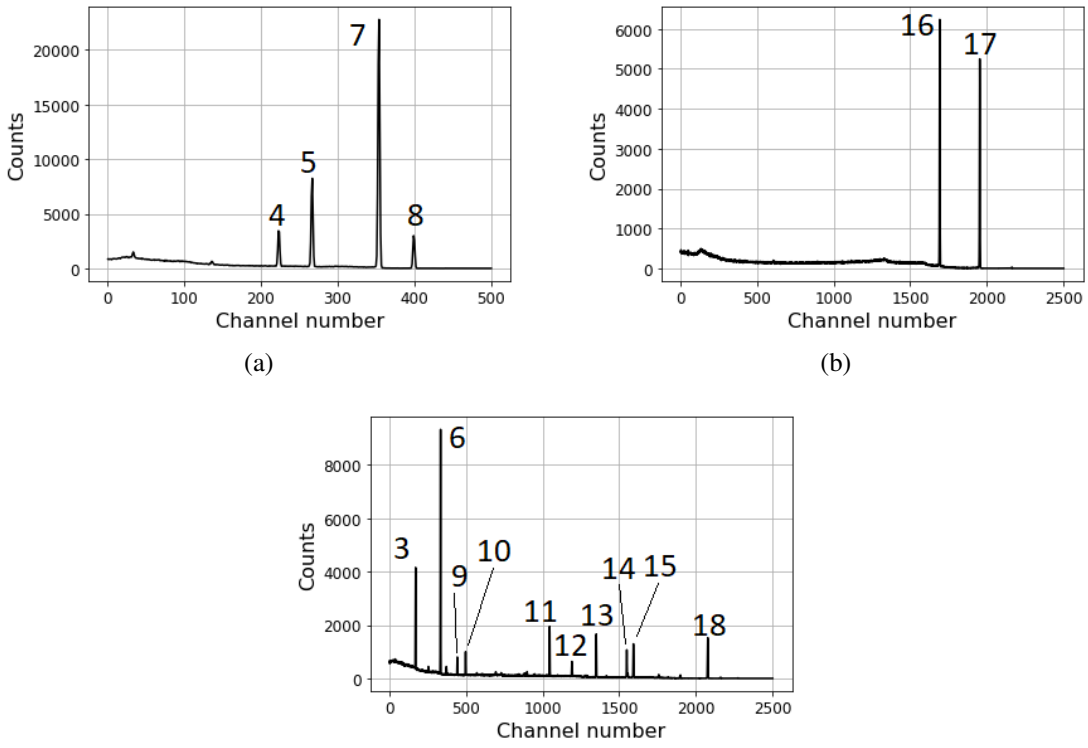

(a) (b)

(c)

Figure 4.3: Energy spectra for a) ^{133}Ba, b) ^{60}Co and c) ^{152}Eu spectra measured for durations of 5941.79 s, 5979.87 s and 6127.39 s respectively.

The 81 keV peak from ^{133}Ba and 122 keV peak from ^{152}Eu are not shown in this spectrum and their channel number is not shown in the table, as they required an amplification gain of 50 to become visible. The only use for these peaks was additional fitting points for the absolute efficiency response determination. For the 81 keV peak, two Gaussians were used instead of one as the 79 keV is in partial overlap. The relative size and positions of these Gaussians matched the expected behavior. The peaks with higher intensity are in general larger, but the efficiency becomes lower for higher energy peaks. The spectrum for ^{60}Co nicely shows the Compton continuum and Compton edge on the low energy side of the peaks. The ^{152}Eu spectrum, on the other hand, shows that for low energy peaks, linear background subtraction is required. This background is not globally linear, but in first approximation, it is in the peak region.

The obtained fits for the energy calibration (both linear and quadratic) are shown with their residues in Figure 4.4 while the obtained fit parameters are shown in Table 4.3. For both fits, the χ^2_{red} is extremely small, therefore the quadratic fit is likely due to overfitting. For the linear fit, χ^2_{red} is small since it describes the measured data points accurately. For the residues of the linear fit, it can be seen that a slight parabolic behavior remains, while the residues of the quadratic fit are quite randomly distributed. The latter improves the fit slightly, but since the maximal discrepancy between the different models is only about 0.05 keV in the window for which data points were measured, it will in practice not change anything.

Assuming a detection resolution of about 1 keV, this discrepancy between the models is negligible. Therefore the linear fit is sufficient. Besides that, the only real purpose of the calibration is for the identification of the peaks of interest. A very precise calibration, in general, doesn't improve the guess for the peak locations, as the peaks can shift slightly during the measurements.

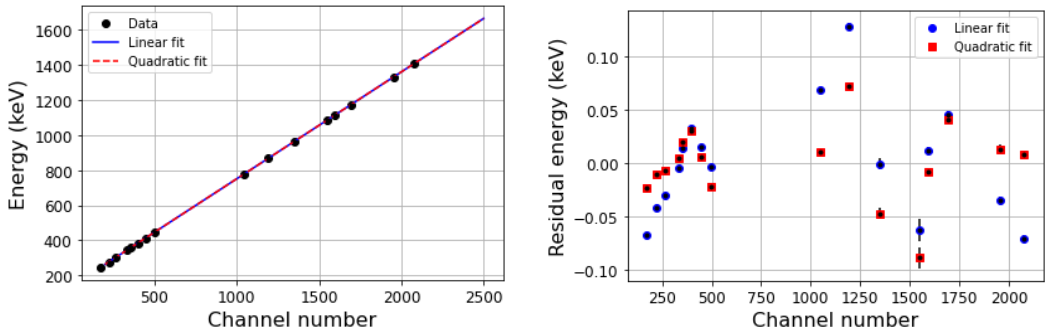

(a) (b)

Figure 4.4: Resulting best fits for linear and quadratic fit functions. (a) The energy and (b) The residual energy plotted against the channel number. The fits are in near-perfect overlap and the error bars are not clearly visible, as they are very small.

Table 4.3: Resulting fit parameters for the Linear and Quadratic model. Here a, b and c denote the proportionality factor of the zeroth, first and second powers of the channel number.

Parameter	Linear	Quadratic
a	139.983(24)	139.897(29)
b	0.610611(21)	0.610885(74)
c	0	-1.30(35)
χ^2_{red}	0.00300009	0.00153670

4.1.3 Efficiency response function

The next thing to do is to make a fit for the absolute efficiency response. This function maps count rates at a given energy into activities. The fit function used for the efficiency is given in Eq. (4.2), which is a polynomial of the logarithm of the energy. The polynomial was truncated after the cubic term, to avoid overfitting with an increasingly complex function. Different models, such as the Weibull model [28], could potentially describe the mapping better in certain cases, but require a larger number of data points to obtain accurate fits.

$$f = \frac{1}{E}\left[a + b\ln(E) + c\ln(E)^2 + d\ln(E)^3\right] \tag{4.2}$$

The resulting fit is shown with its residues in Figure 4.5 while the fit parameters are given in Table 4.4. The error bars of the data points do not include systematic contributions due to uncertainty of the source activity, as they were treated separately. To do this, the assumption was made that the systematic errors and the uncertainty propagated from the parameters are not correlated. The systematic error can in that case be calculated for a set of points using Monte-Carlo methods. The activities of the sources were samples 10^4 times from normal distributions with mean 1 and standard deviations equal to the relative uncertainty on the individual source. The sampled activity is then equal to the obtained random number multiplied by the quotes activity. For each of these generated *triplets*, the fit is performed and its value is kept in 100 equally spaced values for the energy, leading to a $10^4 \times 100$ array. For each of these points, the values corresponding to the index at 15.9% and 84.1% are saved in separate lists. The entries in these lists correspond to the $mean \pm 1\sigma$ efficiencies at each of the 100 points. This is the 1σ systematic error interval due to uncertainty on the sources. When the systematic error and the error obtained from propagating the fitting parameters are added in quadrature, they can be plotted to create a 1σ error region. The error on the fit is heavily dominated by a systematic error caused by the uncertainty of the calibration source activity. At the energies of interest, namely 218 keV and 440 keV, this error from propagating the fitting parameters was only 0.11% and 0.068% respectively.

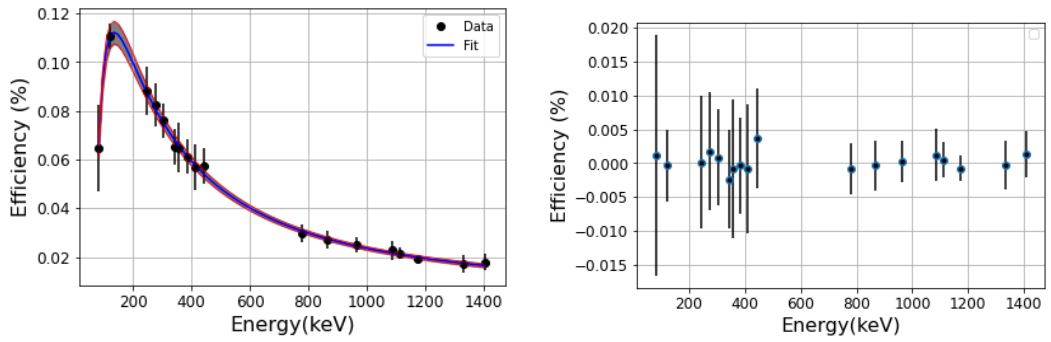

(a) (b)

Figure 4.5: Resulting best fit (a) and residues (b) for the absolute efficiency of the lead castle setup. In (a), the grey colored zone is the error region, the red lines present the edges of this error region and the blue line represents the actual fit.

Table 4.4: Resulting fit parameters for the efficiency.

Parameter	Value
a	-409(55)
b	189(30)
c	-27.5(51)
d	1.32(30)
χ^2_{red}	0.07042503

The residues of the fit are seemingly randomly distributed about 0 and the reduced χ^2 is close to $\frac{1}{N}$, indicating it is a good fit. As the error on the activity measurements will be dominated by the error on the efficiency, these must be as low as possible. To obtain results for the same setup with a smaller error, the calibration sources should either be known to better precision, or more independent sources could be used. By using the 81 and 122 keV peaks, the shape of the fit is already more reliable in the maximal efficiency region. Besides that, they allow interpolation instead of extrapolation for one of the peaks of interest in the ^{225}Ac decay chain (218 keV). As the fitting uncertainty is also largest in the low energy regime, it would be beneficial to measure more sources with peaks around this energy. The obtained values for the absolute efficiency at the peaks of interest are given in Table 4.5. As the systematic errors are not completely symmetric, a one standard deviation error interval is provided instead of the conventional Gaussian error.

Table 4.5: Obtained absolute efficiencies for the peaks of interest in the ^{225}Ac decay chain.

Energy (keV)	Efficiency (%)	Relative error (%)
218.12	0.0948	[-3.5, +3.6]
440.45	0.0543	[-2.9, +3.0]

4.1.4 Geometry correction

The measurements were performed with the foils at an angle of about 63° inside the vial, causing the average source-detector distance to be slightly larger than the distance for which the efficiencies are obtained with the calibration sources. The latter will induce a small negative systematic shift in the efficiencies, and thus a correction factor larger than 1 in the final activity results. The additional *effective distance* is then in first order the height difference of the bottom of the vial to the center of the foil. A graphical representation for this geometrical problem is given in Figure 4.6. The resulting additional height H is given by Eq. (4.3). A derivation for this formula is provided in Appendix B. The measured and calculated values for these distances are shown in Table 4.6. In this formula, t denotes the thickness of the vial bottom.

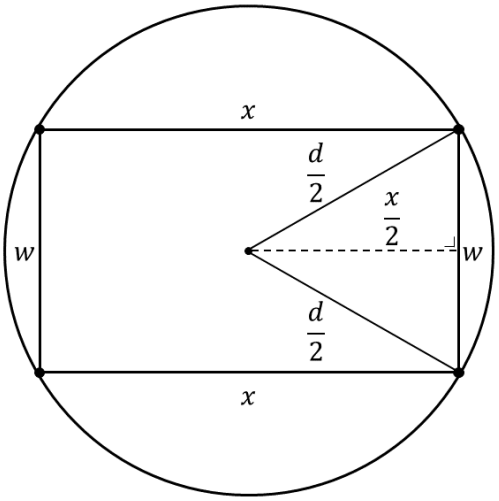

Figure 4.6: Top view geometry of the vial with a rectangular foil. x is the projection of the length of the foil on the bottom of the vial, w is the width of the foil and D is the diameter of the vial.

$$H = t + \frac{1}{2}\sqrt{l^2 + w^2 - D^2} \tag{4.3}$$

	t	l	w	D	x	H
length (mm)	1.3(2)	25.5(5)	15.1(2)	27.3(1)	5.8(6)	7.1(8)

Table 4.6: Obtained distances for the vial geometry

The additional distance is thus equal to 5.8(6) mm. The correction factor is obtained by taking the fractions of the solid angles at distances with and without the correction. The distance from the vial bottom to the germanium crystal is equal to $25.5 \pm 0.01\,cm$, which is calculated by using the values mentioned earlier. The correction factor is thus equal to 1.0565(33) or about 5.7%. This correction is rather large, and thus very important to take into account for reliable results. For this factor, a point source approximation was used, but there is possibly quite a bit of spread. A more rigorous way to make the correction would be to integrate a weighting factor $\frac{1}{(r+h)^2}$ multiplied by the source distribution over dh, where h is the distance between the bottom of the vial and a given point on the sample. As r becomes much larger than the range of values for h, the higher-order correction terms cancel, which provides the point source approximation.

The peaks that were studied with the lead castle setup are shown in Table 4.7 together with their Bateman correction factor, the counts per ^{225}Ac decay and their approximate channel. It should be noted that the uncertainties for counts per ^{225}Ac decay are 2.72% and 0.83% for the 218 keV and 440 keV peak respectively. These are affected by the half-lives, the branching ratios and the intensities. In the final result, they will lead to another systematic error, although these are almost fully uncorrelated to one another, as the decay paths don't influence each other. Assuming no further corrections have to be made, the preliminary activity can be calculated. These will correspond to the time of the EOC at MEDICIS, and can subsequently be used to obtain the activity at the EOC and the collection efficiency.

Table 4.7: Peaks of interest in the ^{225}Ac decay chain with their Bateman correction factors, counts emitted per decay of ^{225}Ac and approximate channel.

Energy (keV)	Bateman correction	counts per ^{225}Ac(%)	Approximate channel
218.12(2)	1.000343(81)	11.40(31)	128
440.45(1)	1.00355(21)	25.46(21)	493

4.2 Experimental Results

4.2.1 Obtaining the EOC activity

Once the calibration is finished, a program was created to obtain the ^{225}Ac activity at a given time. As the peaks can shift slightly between measurements, this had to be a dynamic fitting program. The program analyzed a range around the expected peak position, the maximum value inside this interval was then used to create a new interval centered around the true peak. This way, the initial values of the fit are adapted and the presence of nearby peaks can be suppressed without losing the peak of interest. When this is subsequently iterated over all data files, a list of count rates for the different peaks is obtained over a range of times since the EOC. The measurements started approximately 12 days after the EOC, because the samples had to be transported to IKS. Applying the calibration results and correction factors obtains values for the activity at a given point in time. These are then used to fit an exponentially decaying function $A(t) = A_0 e^{-\lambda t}$, with time 0 defined as the EOC. Due to systematic effects, the results from the different peaks are slightly different. For a better analysis, the data points were fitted separately. The obtained fit parameters are given in Table 4.8, while the resulting exponential decay fits are shown in Figure 4.7.

parameter	M108 (218 keV)	M108 (440 keV)	M118 (218 keV)	M118 (440 keV)
A_0 (kBq)	1060	971	87.7	69.3
error (%)	[-4.70, 4.77]	[-3.39, 3.47]	[-4.98, 5.04]	[-3.16, 3.25]
$\lambda\,(day^{-1})$	0.0693(8)	0.0695(8)	0.0800(6)	0.0724(3)
χ^2_{red}	0.07912361	0.14639101	1.65577188	0.50285249

Table 4.8: Fitting results for the activity of the lead castle measurements.

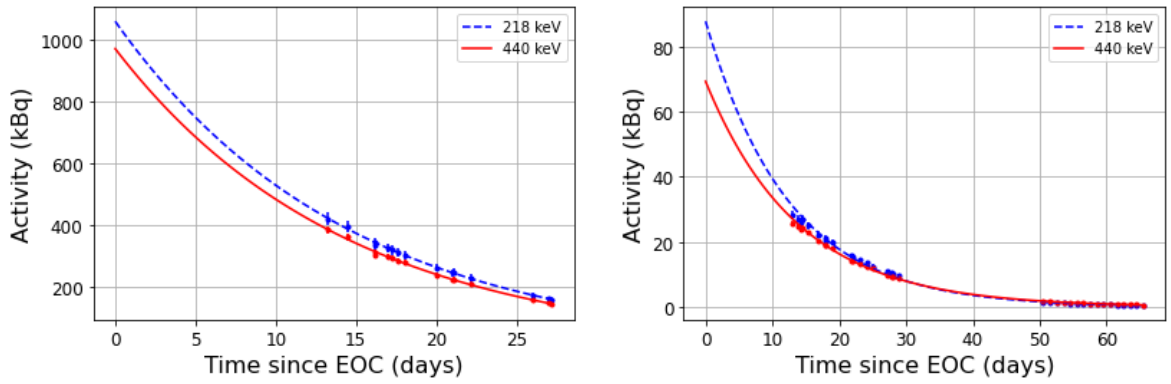

(a) (b)

Figure 4.7: Exponential decay fit for (a) M108 and (b) M118.

There are several contributions that lead up to the final error. First of all, correlated systematic errors are coming from the efficiency fitting. Next, there is the correlated systematic error coming from the vial geometry correction. Furthermore, the uncertainties on literature values of lifetimes, branching ratios and intensities, lead to uncorrelated systematic errors. Changing these values would result in shifting of all the present points by a constant factor. Therefore, they all had to be treated as systematic errors. Taking the quadrature of these systematic errors provides the total systematic error on the data points. On individual data points, there is still some uncertainty coming from the error on the count rates in the order of a percent, but these will not affect the initial activity result significantly. The last contribution to the final error would be the uncertainty from the fitting parameters on the initial activity, henceforth referred to as the fitting uncertainty, which is mainly limited by the number of data points. All of the errors and uncertainties are given in Table 4.9.

Table 4.9: Uncertainties and systematic errors for the lead castle setup.

Type	M108 (218 keV)	M108 (440 keV)	M118 (218 keV)	M118 (440 keV)
Total efficiency	[-3.48%, 3.57%]	[-2.90%, 3.00%]	[-3.48%, 3.57%]	[-2.90%, 3.00%]
Vial geometry	0.32%	0.32%	0.32%	0.32%
Intensities	2.72%	0.83%	2.72%	0.83%
Total systematic	[-4.43%, 4.50%]	[-3.04%, 3.13%]	[-4.43%, 4.50%]	[-3.04%, 3.13%]
Fitting	1.57%	1.48%	2.26%	0.87%
Total	[-4.70%, 4.77%]	[-3.39%, 3.47%]	[-4.98%, 5.04%]	[-3.16%, 3.25%]

For M108, these values seem reasonably good, having half-lives matching the value measured by Kossert et al. [29] (0.06989(22) day^{-1}) within less than one standard deviation and excellent χ^2_{red}. Besides this, something that can be used as a reference, is the fact that they are in relatively good agreement with the estimates from the other setups, which will be discussed later in this thesis. However, one needs to be careful not to focus too much on these results. This would lead us to work towards corrections pushing the results towards the expected values, which would defeat the purpose of independent measurements. The values of M118, on the other hand, have half-lives that exceed the value from [29] and the χ^2_{red} is rather large.

The residues and relative residues of the fits are shown in Figure 4.8. It is expected that the average magnitude of the residues would decrease exponentially, while the relative residues should be approximately normally distributed. While the residues and relative residues follow the expected behavior for the M108 sample, a clear systematic effect is apparent for the M118 sample. Two distinct behaviors are present, corresponding to before and after the sample was moved to another setup. The exact cause of this trend is unclear but is likely caused by human error, either in the analysis or during the measurements. As these anomalous data points are made after the edges of the foil were straightened to fit in the α-chamber setup, it is possible that the additional effective distance decreased slightly compared to the other measurements. The latter would lead to a higher efficiency response, and thus a lower activity. For future works, it could be better to straighten the foils before any measurements are made. This second measurement period is also the cause of the poor agreement in the decay constant. Even though the spread of the residues is significantly smaller than the error bars, this does necessarily mean the error bars are too large. Systematic errors, such as on the efficiency response, would not increase the spread, but instead, shift all values by a constant factor.

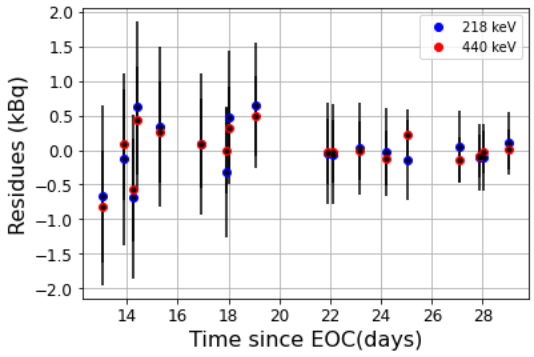

(a) Residues M108

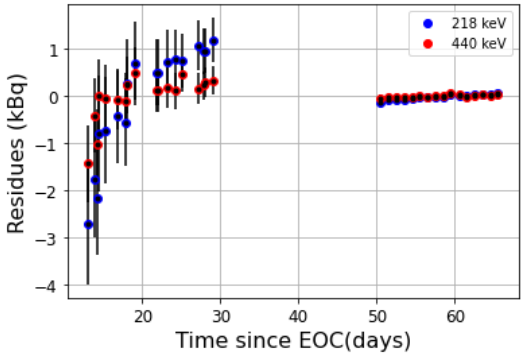

(b) Residues M118

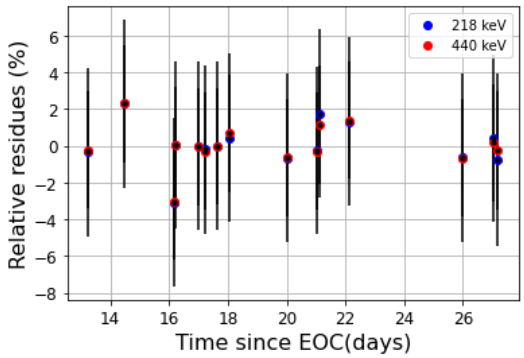

(c) Relative residues M108

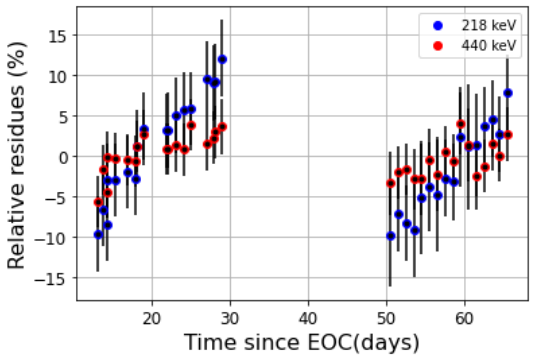

(d) Relative residues M118

Figure 4.8: Residues and relative residues for the exponential decay fitting.

When the fitting for M118 is performed for only the first measurement period, a more reliable result is obtained. The fit is shown in Figure 4.9, the residues are shown in Figure 4.10 and the obtained activity fit results are shown in Table 4.10. The relative error on the activity has been reduced, as has its value. Furthermore, the χ^2_{red} has improved significantly and the decay constant compares well to literature [29]. As the systematic effect in the residues has disappeared, these values were used for further analysis.

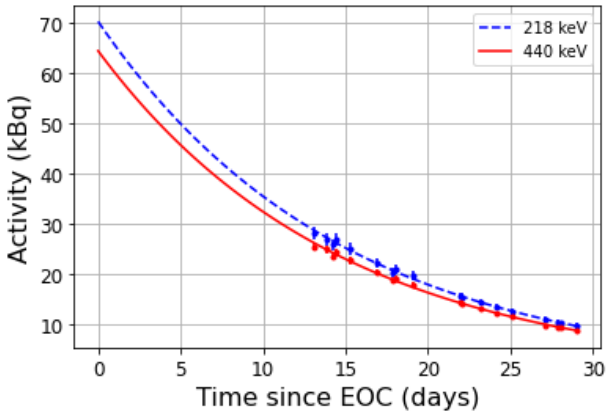

Figure 4.9: Exponential decay fit for M118 using only the data points of the first measurement period.

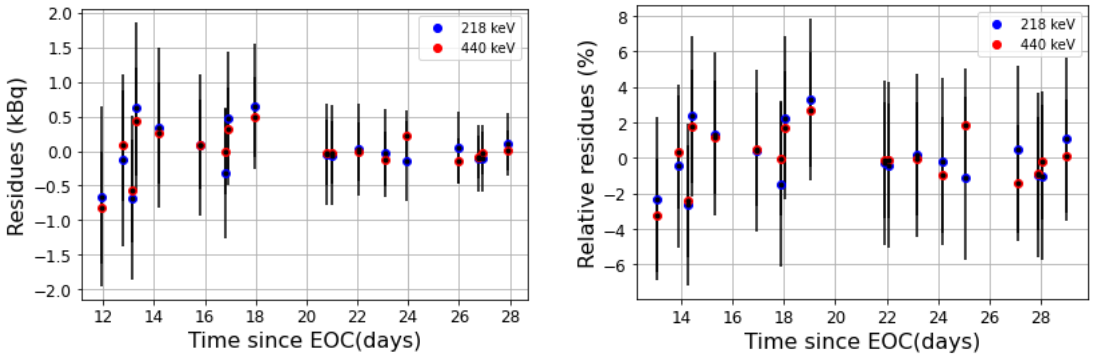

(a) (b)

Figure 4.10: (a) Residues and (b) relative residues for the exponential decay fit of the first measurement period of M118.

Table 4.10: Fitting results for the activity of the first measurement period of M118.

parameter	218 keV	440 keV
A_0 (kBq)	70.3	64.5
Correlated error (%)	[-3.50, 3.59]	[-2.92, 3.02]
Uncorrelated error (%)	3.14	1.69
Total error (%)	[-4.70, 4.77]	[-3.38, 3.46]
$\lambda\,(day^{-1})$	0.0683(8)	0.0696(7)
χ^2_{red}	0.12816865	0.23440565

4.2.2 Dead time and pile-up

For this type of setup, two corrections are usually performed. The first is called the dead time correction, which occurs because a detector can not detect a new particle in a short time window after another particle. For this, the decaying source-method was used to estimate the dead time and the so-called non-paralyzable model was used for the correction factors. The details of which are explained thoroughly in literature [30]. In the decaying source model, the count rate multiplied by $e^{\lambda t}$ is plotted against the count rate for the measurements. This was done for the high activity sample (M108), as this should in theory provide the largest difference. If there is no dead time, this should provide a constant function equal to the activity at $t = 0$, as the count rate itself is given by $c_0 e^{-\lambda t}$. If there is significant dead time, this becomes a linearly decreasing function (in first order). The dead time is in that case given by Eq. (4.4). The resulting fit is shown in Figure 4.11 while the fitting results are given in Table 4.11.

$$\tau_{dead} = -\frac{slope}{intercept} \tag{4.4}$$

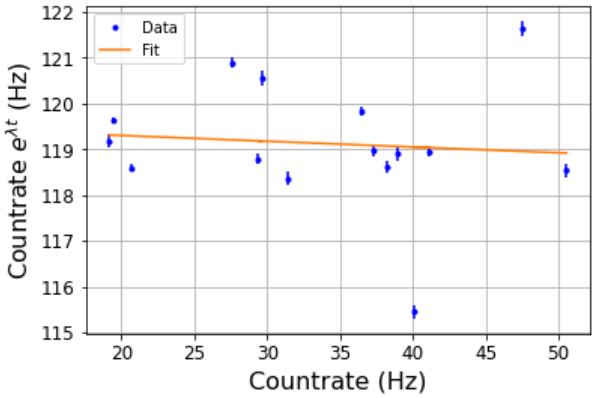

Figure 4.11: Fit for the estimation of the dead time using the M108 measurements.

Table 4.11: Obtained parameters from the dead time fitting.

Parameter	Value
χ^2_{red}	2.09457639
intercept	119.6(15) Hz
slope	-0.013(41)
τ_{dead}	105(336) μs

The obtained dead time was 105 μs, with an uncertainty of 319%. The order of magnitude is certainly realistic for HPGe detectors (order 1-100 μs) [31]. Using the non-paralyzable model, the dead time and adds a correction factor $1/(1-m\tau)$, where m is the total count rate in the detector and τ is the dead time. As it acts the same on both peaks, and no significant coincidences occur with these peaks, this should not cause a systematic shift between the two.

The large uncertainty on the dead time is mainly caused by the low number of data points in combination with the near-constant values over the measurement period. This large uncertainty implies that there is only 63% confidence that the slope is negative. As the dead time correction will be relatively small (0.1-1%) compared to other corrections, and the uncertainty on the dead time is very large, it was assumed that dead time does not affect the count rates significantly. To study the dead time more accurately, more data points should be used. This should preferably be done with high count rates on a relatively fast decaying source.

The second correction that is often applied, is to account for potential pile-up. This effect is caused by 2 subsequent events in the detector whose signals are not fully resolved. This causes an incorrect channel number to be assigned to the peak. If pile-up is present, the peak will be smeared, causing the Gaussian fit on a small range to differ significantly from the Gaussian fit on a larger range. To investigate the effect, the fitting was performed on a range of approximately $[-3\sigma, 3\sigma]$ and compared to the fit in the range of $[-10\sigma, 10\sigma]$. Due to the low number of channels in the peak, the fitting of the narrow range provided large errors. If the ratio of the integrals obtained from the fits differs significantly, pile-up has to be taken into account. The resulting fractions were plotted in Figure 4.12. The peak itself contains a small number of bins and in each of these, there is a non-linear behavior. This causes the narrow fit to have a large error.

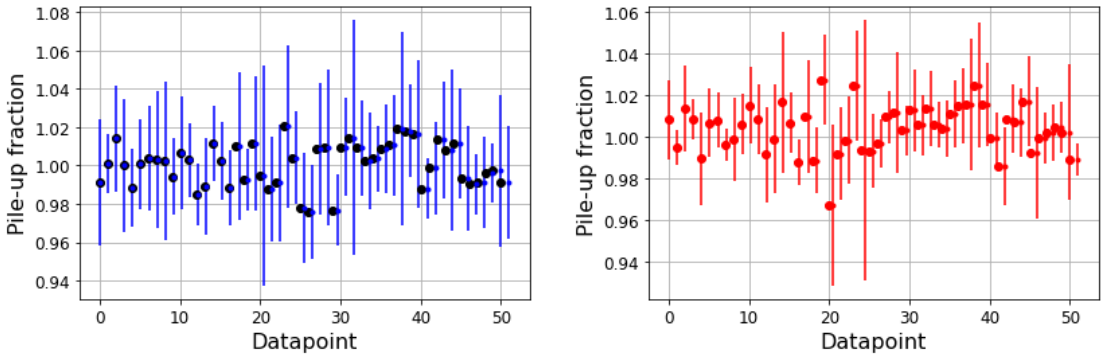

(a) (b)

Figure 4.12: Pile-up fraction for (a) the 218 keV peak and (b) the 440 keV peak.

As the pile-up fraction is not significantly different from 1, and there is no decreasing trend, it was assumed this difference was caused by the low number of data points in the $[-3\sigma, 3\sigma]$ interval (only 8). This combined with a Gaussian + Linear background fit, which has 4 parameters, results in an overfit. For future works, this could be improved by a higher gain during the measurements. The Gaussian is also fitted well in the large range, having less than 0.3% propagated uncertainty on the Gaussian parameters. Even though the activity was in the order of 100 kBq, the low efficiency of the setup causes both dead time and pile-up not to have a significant effect. The count rate in the detector was 275 counts per second at the start of the M108 measurements. This implies the average time separation between events is about 3.6 ms. The length of the pulses (after the preamplifier) is in the order of a couple of microseconds. This is approximately 3 orders of magnitude smaller than the average spacing, implying its effect would be minor.

4.2.3 Mean EOC activity

Once these corrections were obtained, two distinct initial activities remained. To get a final result for the initial activity, a weighted average has to be taken. The weightings are chosen to be the inverse of the variance of the activity for each of the two peaks. As slightly asymmetric error intervals are present, the symmetric standard deviations are taken to be the mean of the absolute values of the positive and negative standard deviations. The weighted average is then given by Eq. (4.5). Here A_i and V_i denote the mean activity at EOC and variance of the i'th peak. As the weightings are larger for the 440 keV peak than for the 218 keV peak, the mean value of the collection activity will be close to that obtained from the latter of the two peaks. The weighted sum provides ^{225}Ac activities of 1002 kBq and 66.5 kBq for M108 and M118 respectively.

$$< A >= \frac{\frac{A_1}{V_1} + \frac{A_2}{V_2}}{\frac{1}{V_1} + \frac{1}{V_2}} \tag{4.5}$$

To estimate the error on this average, the correlated and uncorrelated contributions should be considered separately. As the energies are relatively close to each other, it was assumed that the error from the efficiency was fully correlated. Furthermore, the vial geometry is the same for each peak activity and thus is fully correlated. As the γ-intensities are independent of the preceding decay pathway in parent isotopes, the error from the intensities is completely uncorrelated. Finally, the error obtained from propagating the fitting parameters was assumed to be uncorrelated as well. The variances are shown in Table 4.12 together with the variances of the correlated and uncorrelated contributions.

Table 4.12: Relative Total, correlated and uncorrelated variances for the lead castle measurements.

Variance	M108 (218 keV)	M108 (440 keV)	M118 (218 keV)	M118 (440 keV)
Total	2.23×10^{-3}	1.17×10^{-3}	2.24×10^{-3}	1.17×10^{-3}
Correlated	1.26×10^{-3}	0.89×10^{-3}	1.26×10^{-3}	0.89×10^{-3}
Uncorrelated	0.99×10^{-3}	0.29×10^{-3}	0.99×10^{-3}	0.29×10^{-3}

To propagate the variance on the mean (V_A), Eq. (4.6) was used. This accounts for the correlations between the activity of the two peaks (A_1 and A_2). In this formula, V_i and w_i denote the total variance and the weighting factor of the i'th peak. Besides this, σ_i and S_i represent the uncorrelated and correlated standard deviations.

$$\begin{aligned} V_A &= \left(\frac{\partial A}{\partial A_1}\right)^2 V_1 + \left(\frac{\partial A}{\partial A_2}\right)^2 V_2 + 2\frac{\partial A}{\partial A_1}\frac{\partial A}{\partial A_2} Cov(A_1, A_2) \\ &= \frac{1}{(w_1+w_2)^2}\left[w_1^2\sigma_1^2 + w_2^2\sigma_2^2 + w_1^2 S_1^2 + w_2^2 S_2^2 + 2w_1 w_2 S_1 S_2\right] \\ &= \frac{1}{(w_1+w_2)^2}\left[w_1 + w_2 + 2w_1 w_2 S_1 S_2\right] \end{aligned} \tag{4.6}$$

$$\implies \sigma_A = \frac{1}{w_1 + w_2}\sqrt{w_1 + w_2 + 2w_1 w_2 S_1 S_2} \tag{4.7}$$

Inserting the previously obtained values into Eq. (4.7) provides 3.54% and 3.51% errors on the weighted sum for M108 and M118 respectively. The mean EOC activity results for the lead castle setup are shown in Table 4.13.

Table 4.13: EOC ^{225}Ac activity estimates from the lead castle setup, obtained via fitting with a free half-life.

Foil	Initial activity (kBq)	Relative error (%)
M108	1002	3.53%
M118	66.5	3.52%

To conclude the lead castle measurements, the fit was performed again with a fixed half-life. This will cause the relative error on the activity extrapolation to be slightly smaller, as the error from the propagation of the fitting parameter reduces. The fitting results are shown in Table 4.14, the resulting fit is shown in Figure 4.13 and the residues are shown in Figure 4.14.

Table 4.14: Fitting results for the activity of the lead castle measurements using a fixed half-life.

parameter	M108 (218 keV)	M108 (440 keV)	M118 (218 keV)	M118 (440 keV)
A_0 (kBq)	1072	979	72.6	66.1
error (%)	[-4.45, 4.52]	[-3.06, 3.15]	[-4.45, 4.53]	[-3.07, 3.16]
χ^2_{red}	0.07681656	0.13892331	0.07681656	0.26407615

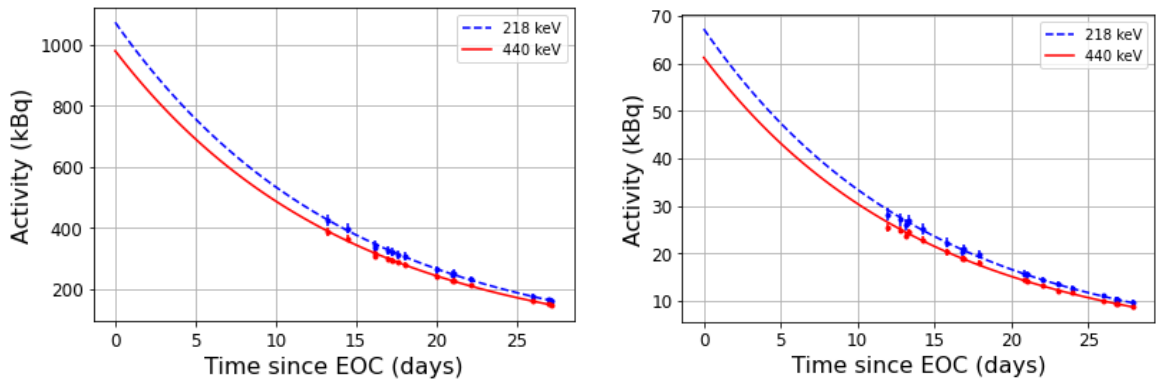

(a) (b)

Figure 4.13: Exponential decay fit for (a) M108 and (b) M118 using a fixed half-life.

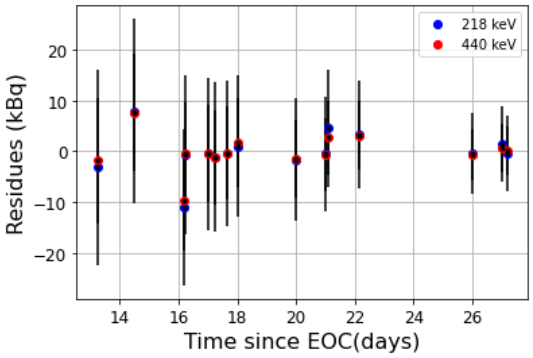

(a) Residues M108

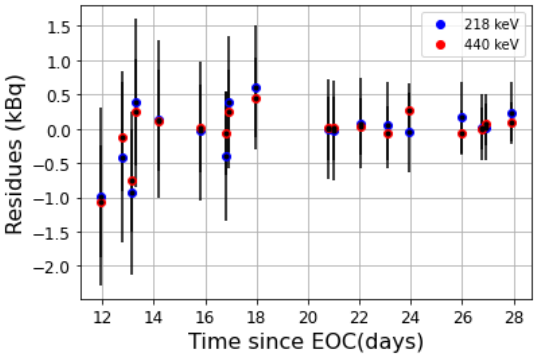

(b) Residues M118

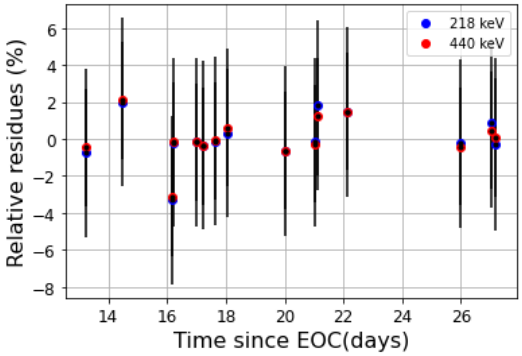

(c) Relative residues M108

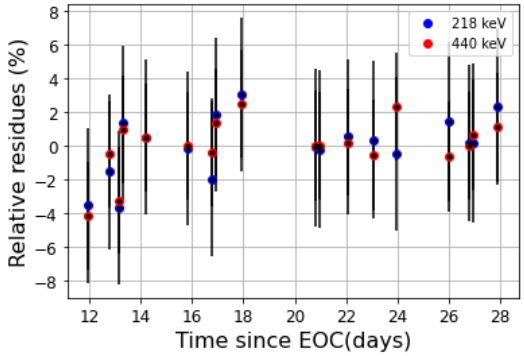

(d) Relative residues M118

Figure 4.14: Residues and relative residues for the exponential decay fitting using a fixed half-life.

Similar to before, the residues are randomly distributed and decreasing in magnitude over time, while the relative residues remain approximately constant in magnitude over time. Using these results, the error can be propagated again using Eq. (4.6). The mean EOC activity results for the lead castle setup using a fixed half-life are shown in Table 4.15.

Table 4.15: EOC ^{225}Ac activity estimates from the lead castle setup, obtained via fitting with a fixed half-life.

Foil	Initial activity (kBq)	Relative error (%)
M108	1009	3.33%
M118	68.2	3.33%

From these values, an important remark has to be made. There is a clear systematic effect between the 218 and 440 keV results. This could have been caused by a combination of systematic error on the efficiency, the theoretical branchings and corrections that are different for the two peaks. The relative difference of the activities was 8.68% and 8.95% for the M108 and M118 sample respectively. The fact that the difference is not the same for the different foils indicates that an activity-dependent correction could be (at least partially) responsible for the discrepancy. In reality, the systematic effect on the total efficiency is partially positively correlated, but let's for a moment assume it is not. When the fully positively correlated error of the vial geometry is left out, new error intervals can be obtained. By estimating the activity values as Gaussian distributed with a standard deviation equal to the mean of the remaining error interval, the overlapping fraction between the Gaussians can be calculated. Using the overlap function in python obtains roughly 22.5% and 12.8% for M108 and M118 respectively. Therefore, we can say with 77.5% and 81.2% reliability that these values are systematically different beyond the current errors that were considered. The overlap between the Gaussians is shown in Figure 4.15.

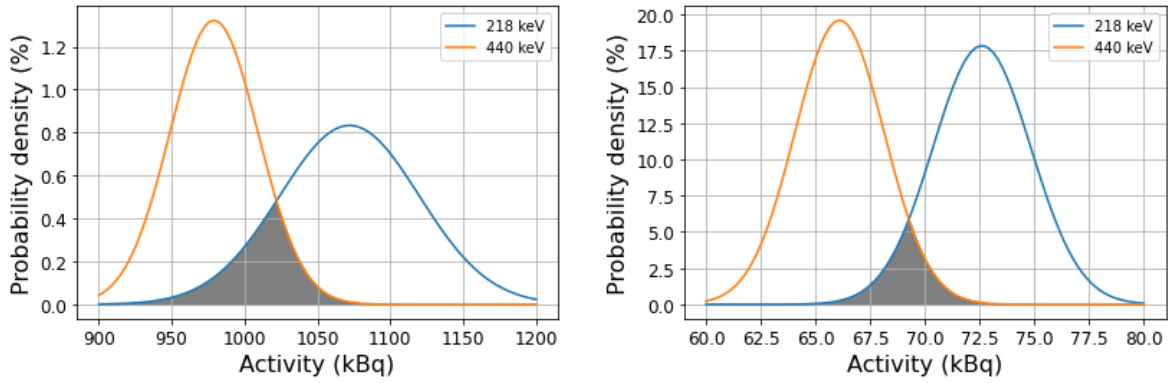

(a) (b)

Figure 4.15: Overlapping fraction of the activity obtained from the different peaks for (a) M108 and (b) M118.

5 γ-γ Coincidence Measurements

5.1 Concepts and Calibration

Contrary to the lead castle setup, the coincidence setup does not require a very low background to accurately determine an activity. Good statistics ($\frac{1}{\sqrt{N}} << 1$) can be obtained by measuring the frequency of γ-photons in coincidence with sufficiently high intensity in the same cascade. By combining the count rates in a very specific way, as shown in Eq. (5.1), an activity can be obtained that does not depend on the efficiency.

$$
\begin{aligned}
N_1(E_1) &= A\, I_1\, \varepsilon_1(E_1) \\
N_2(E_2) &= A\, I_2\, \varepsilon_2(E_2) \\
N_{12}(E_1,E_2) &= A\, I_{12}\, \varepsilon_1(E_1)\, \varepsilon_2(E_2) \\
\\
\Longrightarrow \frac{N_1(E_1)N_2(E_2)}{N_{12}(E_1,E_2)} &= A\frac{I_1 I_2}{I_{12}} \\
\Longrightarrow A &= \frac{N_1(E_1)N_2(E_2)}{N_{12}(E_1,E_2)}\frac{I_{12}}{I_1 I_2}
\end{aligned}
\tag{5.1}
$$

Here $N_i(E)$ is the count rate of photons of energy E in detector i, A is the activity of the source, I_i is the γ-intensity of the i'th peak, $\varepsilon_i(E)$ is the total efficiency response at energy E in detector i, I_{12} is the intensity of the coincidences (which is not necessarily equal to $I_1 I_2$) and $N_{12}(E_1,E_2)$ is the rate of coincidences for a photon with energy E_1 in detector 1 and E_2 in detector 2. This method of measuring the activity is called *efficiency-free activity measurements*. As can be seen in Chapter 4 and Chapter 6, spectroscopy techniques are often limited by the accuracy of the efficiency. Therefore, this method provides a major advantage. The only major downside of these measurements is that the count rate for true coincidences is usually rather small, in the order of 0.2% and 2% for ^{213}Bi and ^{209}Tl respectively. Consequently, only the high activity foils (M108 and M120) were measured using this setup.

The typical efficiencies that are relevant are the intrinsic, geometric and electronic efficiency. However, besides just cancelling these, effects such as pile-up and dead time do not influence the activity either. In this context, dead time changes both the single count rates and the coincidence count rates in Eq. (5.1). The proof for dead time is shown in Appendix C. In reality, there are still corrections coming from the angular correlation between photons. As mentioned in Chapter 3, there are two sets of coincidences that are of interest, following the β-decay of ^{213}Bi and ^{209}Tl. The former consists of one transition that is a mixture of M1 and E2, while the multipolarity of the second was not found in literature. The transitions that make up the ^{209}Tl coincidences are both E2 radiation, indicating no correction is present.

A picture and a schematic representation of the coincidence setup is shown in Figure 5.1. The foil is placed at point A, similarly to the lead castle setup inside the vial to reduce contamination risks. For this setup, two HPGe detectors (at point B and C) were used which are directly coupled to preamplifiers and kept at cryogenic temperatures. From now on these will be referred to as detector 0 and detector 1 respectively. The amplified signal is then used as input for the data acquisition system, which is represented by the grey box D. Finally, the data is interpreted by the computer.

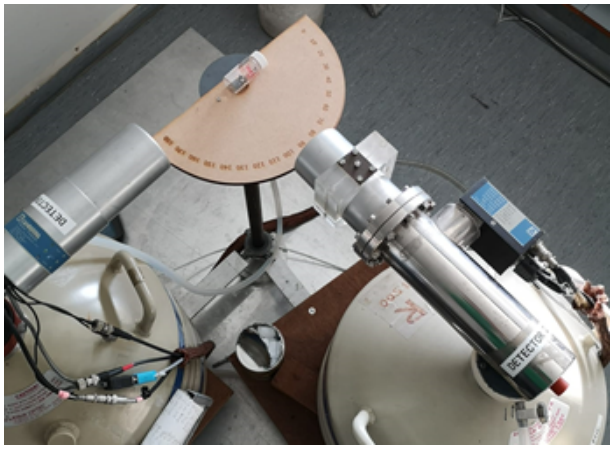

(a)

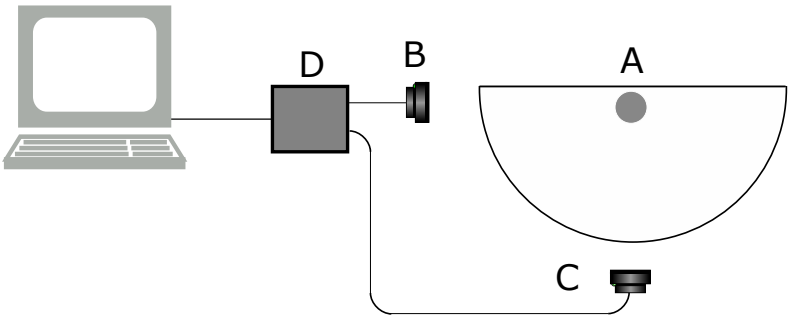

(b)

Figure 5.1: (a) Picture of the detectors and surface on which the foils were placed, and (b) Graphic representation of the coincidence setup.

The arrangement used a digital data acquisition system (Caen N6724) and the electronic scheme are shown in Figure 5.2. Using a digital acquisition system means that components such as discriminators, shaping amplifiers and coincidence units are replaced by a single digital unit [32]. After the preamplifiers, the signals are directly passed into the digitizer.

As this setup is also used for the measurement of angular correlation experiments, one of the detectors is movable. For the purpose of this experiment, the different detectors were kept at an angle of 90° for all of the measurements. With this angle, all cosine terms for the angular correlation cancel out, only leaving sine terms. These sine terms appear when two different types of multipolarities are in coincidence (magnetic and electric). When the lowest order multipole radiations are of the same type, this correction will be rather small, as seen by using Weiskopf estimates. Using typical values provides that the M3-to-E2 transition rate fraction is between 10^{-6} and 10^{-7}. On the other hand, if a mixing between M1 and E2 is present, a slight asymmetry will need to be taken into account due to the phase difference.

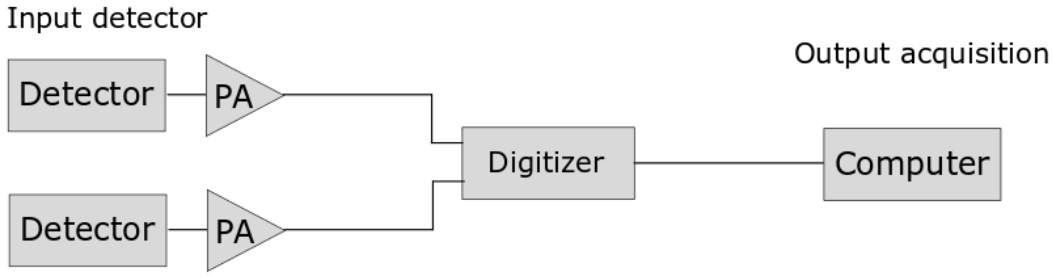

Figure 5.2: Electronic scheme of the coincidence setup

Similar to Chapter 4, the Bateman equations have to be used to obtain the ^{225}Ac activity. As the ^{209}Tl half-life is small compared to that of ^{213}Bi, the correction factors will be nearly identical for these two isotopes (only a factor 1.00015 different). The decay schemes of ^{213}Bi and ^{209}Tl are thoroughly discussed in literature [20, 21]. The decay scheme of these isotopes is much more complicated than for example ^{60}Co, since instead of two photons, there is an entire spectrum present. While the ^{209}Tl γ-decay of interest is E2-E2, the multipolarities of the ^{213}Bi are not well-investigated in literature. Furthermore, only a small fraction of the ^{213}Bi decays passes through the state in which the second coincidence photon is emitted. As the intensity of that peak is not equal to the probability of a photon being emitted from that state, $I_{12} \neq I_1 I_2$. Therefore, the fraction of intensities in Eq. (5.1) no longer cancels out. In ^{60}Co and ^{209}Tl, essentially all of the decays pass through the state from which the second photon can be emitted. However, for ^{213}Bi this is only 0.56% of the decays. The general form of I_{12} is given by (5.2). In this equation, I_1 and I_2 denote the γ-intensity of the individual photons, while B_i is the branching of an individual state i towards the state from which the second photon is emitted. The latter has to be summed over all feeding state. The fraction is equal to the probability of decaying via γ-decay provided that the atom is in the excited state that can emit the secondary coincidence photon. Or equivalently, the probability of emitting the second photon after the first has been emitted.

$$I_{12} = I_1 \frac{I_2}{\sum_i B_i} \tag{5.2}$$

5.2 Remeasuring the ^{60}Co source

As mentioned in Chapter 4, the ^{60}Co source of approximately 10.6 kBq was measured again using the efficiency-free activity measurement technique. The activity of the source was flagged as unreliable due to a discrepancy in the efficiency response. The values for the absolute efficiency were substantially higher than peaks at similar energies from different sources. As it is a homemade source, it is possible that the quoted activity was an estimate based on chemical reaction dynamics. The decay of ^{60}Co also provides a more simple case, such that the procedure that was used for the activity measurements on the sample can be explained. The decay scheme of ^{60}Co is shown in Figure 5.3. As the 2+ isomer has a short lifetime compared to the age of the source, no significant fraction is present at this point. In the decay, most of the branching goes to the second excited state via β-decay. From this state, a photon is emitted at 1.17 MeV to de-excite towards the first excited state. As this state is very short-lived (ps), a second photon with energy 1.33 MeV is send out in near coincidence to de-excite towards the ground state. In this particular decay, I_{12} is equal to $I_1 I_2$, as all of the decays pass through the first excited state. In the analysis, it is possible to set energy gates around the individual coincidence photon energies.

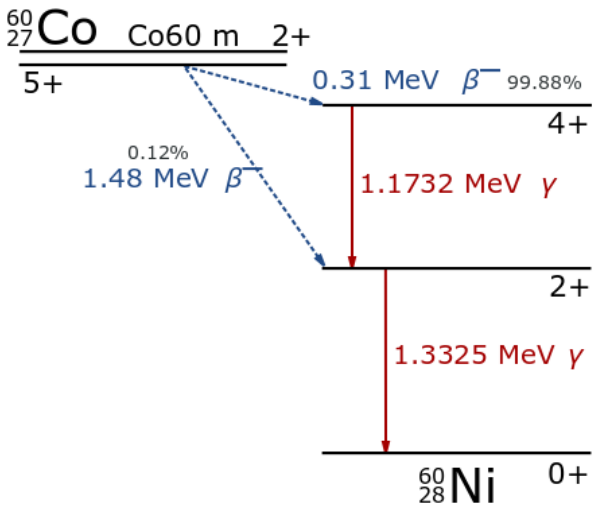

Figure 5.3: Simplified schematic representation of the decay of ^{60}Co to ^{60}Ni. Adapted from [33].

The characterization of the coincidence window was performed with a 201 kBq ^{60}Co source. The time difference between events was plotted for a single energy gate and a double energy gate in Figure 5.4 (a). From this plot, a coincidence window of 200 ns on both sides can be visually estimated. By doing this, background coincidences are suppressed as much as possible, without losing true coincidences due to timing gate discrimination. This window is much larger than the actual time difference between the emission of the photons, which is due to the poor timing of HPGe detectors. As two energy gates decreased the number of counts significantly, the energies present in the single gated coincidences were plotted in Figure 5.4 (b).

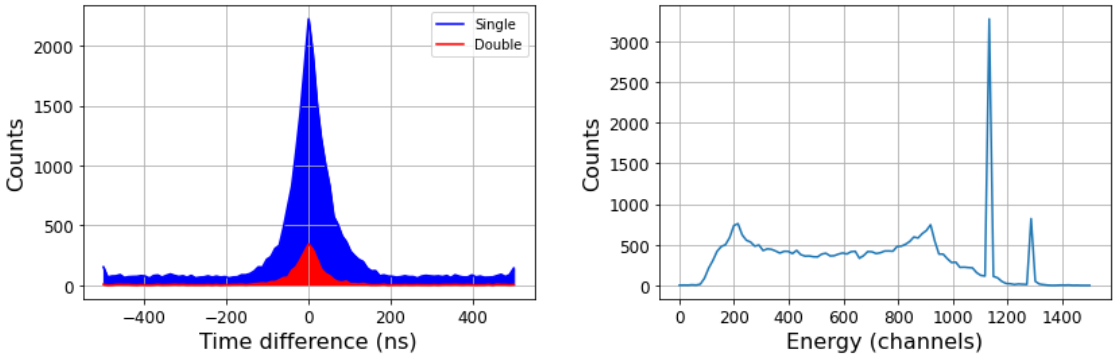

(a) (b)

Figure 5.4: a) Coincidences as a function of time difference for a single (blue) and double (red) energy window. b) Energy of the coincidence particles after a 1332 keV trigger photon.

Besides the expected coincidence peak around channel 1150, a Compton continuum is present as well as a smaller high energy peak. The former of these is mainly coming from photons that are true coincidences, but that lost energy due to Compton scattering. The high energy peak, on the other hand, is not a real coincidence. This is a part of the *activity-dependent random* coincidences. These random coincidences are caused by two decays happening around the same time. The first photon of a particular decay is triggering the coincidence window, while the second photon is coming from a different atom decaying at nearly the same time. This provides an approximately constant background, whose fraction to the true number of coincidences is proportional to the activity of the source. When the coincidence counts are taken, this background should be estimated outside the coincidence window. Subsequently, the expected fraction inside the coincidence window should be subtracted to obtain the true coincidences. For the singly energy-gated graph in Figure 5.4 (a), the constant background is approximately 100 counts per histogram bin. While this fraction is very significant for this high activity source, leading up to 8% of the total coincidences (doubly gated), it is estimated to only be 0.4% for the 10.6 kBq source.

If the source had been measured using this technique several half-lives ago, the fraction of random coincidences to true coincidences could have been high. This would imply an increased coincidences count rate, and therefore a decreased measured activity. To obtain a relative uncertainty on the activity similar to that of the other sources, Poisson statistics implies that between 500-600 true coincidences would have to be measured, corresponding to an error between 4% and 4.5%. Using quick activity estimates, it was concluded that a measurement of 5 days would be required to obtain sufficient statistics. With the subtracted random coincidences, the activity for a ^{60}Co source is given by Eq. (5.3). In this equation, N_1 and N_2 are the count rates of the individual peaks in a respective detector, obtained by fitting with a Gaussian+Linear fitting function. Furthermore, N_{12} and N_{rand} are the total coincidence count rate and the random coincidence count rate respectively.

$$A = \frac{N_1 N_2}{N_{12} - N_{rand}} \tag{5.3}$$

The number of counts of the correct energies, obtained from the fitting, was equal to 2756385 and 2717342 for the first and second detector respectively. The total amount of coincidences within a 200 ns window, was equal to 877. As the individual peak counts are several orders of magnitude larger than the number of true coincidences, the final error will be heavily dominated by the number of true coincidences. By now, the random coincidences were only equal to approximately 7 counts in the coincidence window. The number of total coincidences is almost twice the amount that was initially expected. Besides that, the background fraction is roughly equal to 0.8%, which is also twice the value that was predicted. By dividing by the length of the measurement and using Eq. (5.3), a value of 19.9 kBq was obtained. Using Poisson statistics, a relative error of 3.4% was estimated. This new estimate reduced the residuals of the data points from the ^{60}Co source in the efficiency response fit, shown in Figure 4.5, indicating that the measurement is indeed correct.

5.3 Analysis of the foil data

As the peaks of interest have low intensity, it will in some cases be hard to differentiate them from the background using similar fitting strategies as before. ROOT was used for the analysis, which allowed for the background to be estimated with a specialized function and subtracted from the original spectrum. While this impacts the fit for the individual count rates, it does not for the coincidence count rates. This is the case because there is no way to differentiate which photons have undergone Compton scattering. The background subtraction for one of the measurements is shown on logarithmic scale in Figure 5.5. Here the red line represents the estimated background. The remaining spectrum is shown on a linear scale in Figure 5.6.

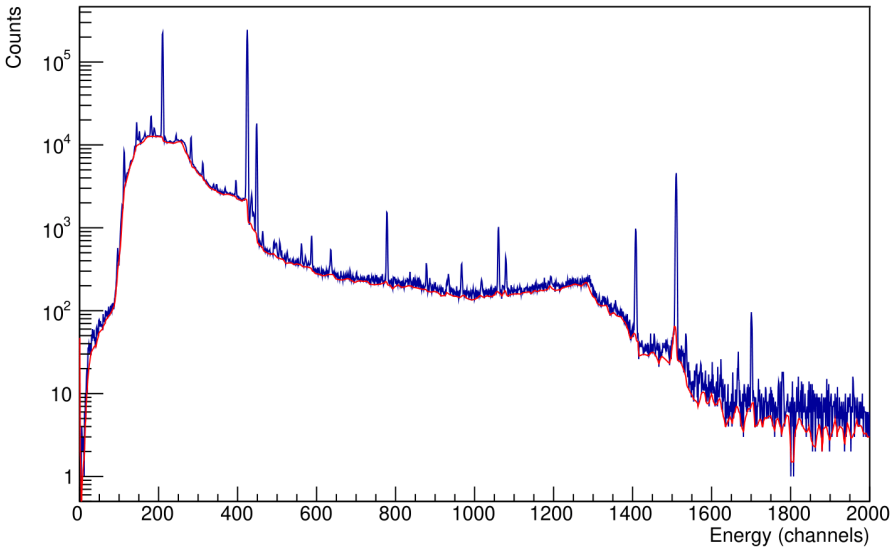

Figure 5.5: Background estimation on logarithmic scale for a sample spectrum.

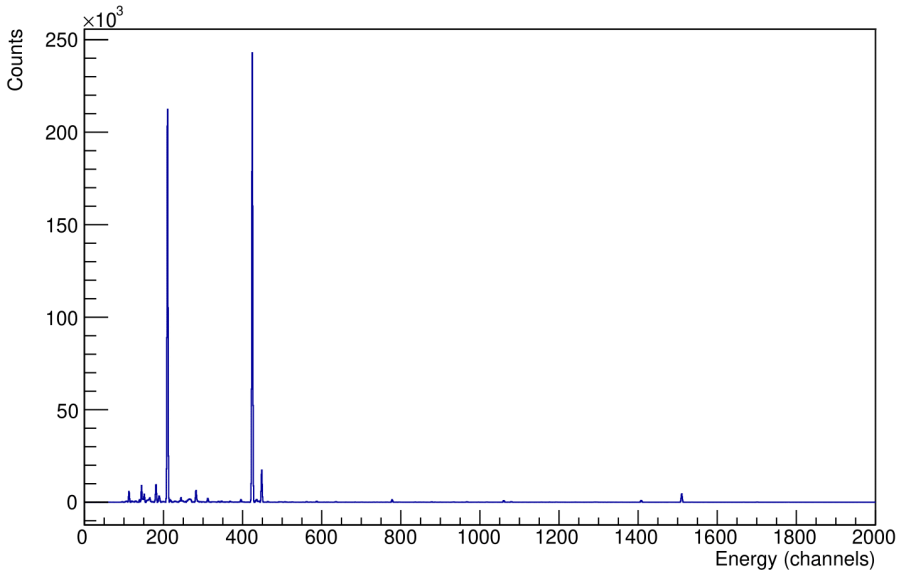

Figure 5.6: Spectrum remaining after background subtraction, shown on linear scale.

The background subtraction leaves a very clean spectrum, only consisting of peaks. Because of this, the bin integral was taken instead of the Gaussian integral. The uncertainty estimation on this is performed by Poisson statistics, which is negligible compared to the uncertainty on the coincidence counts. As the coincidence setup uses peaks with low intensities, and the channel numbers shift over different measurements, there is no use to make a single energy calibration and apply it to all measurements. If this would be done and a part of a strong peak appears in the predefined range for the desired peak, the integral will drastically increase. This would mainly cause a problem for the 465 keV peak, as it is only 25 keV away from the strong 440 keV peak (about 25 channels). This leaves little leeway for the channel shifting before dramatically wrong values are obtained. Therefore, a completely different approach was used. As seen in the lead castle setup, a linear calibration is often extremely good. By taking the highest peaks of the background-subtracted spectrum in specific regions and assigning them with the energies 218 and 440 keV, a quick linear energy calibration can be performed for each individual file, which is accurate up to about 3 channels. When this is done, a window of 10 channels on each side can be chosen without other peaks entering this integration domain. The bin with the maximal number of counts is stored as the true peak position. This is then used as the central bin for the coincidences, around which the energy window is set.

For the coincidences, the events in the first detector were analysed first. If the energy is within one of the windows for a photon of interest, the 10 events before and after that one are further considered as secondary events. This value was chosen such that a potential coincidence photon is statistically essentially always in this interval. After this, three properties of these secondary events are investigated. The particle can only be a coincidence when the detector in which the particle is detected is different from the primary event. Furthermore, the secondary particle has to be within the coincidence window and the energy matches the expected window for the photon which is in coincidence with the primary particle. When all of these conditions are met, the number of coincidences is increased by one.

Due to switching between setups and refilling of liquid nitrogen for the cooling of the detectors, the measurements were made in several batches. As the file size was limited to 50 MB, each of them consisted of several files. For each batch of measurements, the files concatenated in a chain, which contained all of the events in that batch. To obtain multiple data points per chain, they were split up into parts containing at least several coincidences. If the number of events is kept fixed, the relative uncertainty remains roughly the same, while the number of data points within a chain decreases. To obtain more data points for later measurements, Eq. (5.4) was used. Here N_0 is the number of events per data point in the first batch, N_{batch} is the number of events per data point at a specific batch, t_{batch} is the time the batch of measurements was started with respect to the EOC and t_0 is the time the first batch of measurements was started with respect to the EOC. Ideally, this 1/2 exponent would be removed, as the absolute errors would in that case remain the same for all data points. However, since some files had almost no coincidences in this case, this was adapted.

$$N_{batch} = N_0 \left(e^{\lambda (t_0 - t_{batch})} \right)^{1/2} \tag{5.4}$$

The main drawback of this method for the ^{225}Ac is that the coincidence intensities are very low (0.2% and 2% for ^{213}Bi and ^{209}Tl respectively). As a counting experiment is performed, Poisson statistics are again applied. Similarly to the ^{60}Co-remeasurement, N_1 and N_2 have insignificant relative errors compared to N_{12}. To give a reference, to obtain an uncertainty of 10% on a single measurement point, 100 counts are required. When taking into account absolute detection efficiencies in the order of 0.1% for both detectors, the necessary emitted count rate increases to approximately 10^8. To use as much of the data as possible, both detector combinations are used. That is, both detectors can detect the trigger photons. These are not systematic errors, like the efficiency in the other setups. This implies that through many data points, the residues are approximately normally distributed. This in turn will cause the obtained initial activity to have a smaller overall uncertainty. Having taken all of these aspects into account, the only major systematic effect that needs to be considered are angular correlation between the photons and the literature uncertainties on the lifetimes, branching ratios and intensities. Unlike for the previous setup, there is in fact some minor correlated effect in these errors, as a change in branching ratio towards ^{213}Bi immediately reduces the branching to ^{209}Tl.

5.4 Experimental Results

5.4.1 Coincidence contributions

Contrary to the ^{60}Co measurements, the intensities (per decay of ^{225}Ac) of coincidences in the ^{209}Tl- and ^{213}Bi relaxation are only about 2% and 0.2% respectively. The maximal random-to-true coincidence fraction can be estimated using the activity the foils had at the start of the IKS measurements (10 days after EOC for M108), which was approximately 500 kBq. These random coincidences have the same efficiency as the true coincidences, implying the relative count rates are not efficiency dependent. The fraction of random-to-true coincidences is equal to the count rate of two decays happening within the coincidence window. By fixing the center of the coincidence window to the first event, the second has a 400 ns window. This results in about 0.4% and 0.04% of the total coincidences coming from random events, which is negligible. Besides these random coincidences, another possible contribution is from background coincidences. This effect is caused by a second set of coincidences, for which part of the response (e.g. the Compton continuum) is inside the energy window of the coincidences of interest. The energy of these background coincidences can be both from the main peak and the Compton continuum. As an energy window was set on each of the photons, and no significant coincidences were present with similar energy combinations, this was assumed to be zero. In scenarios where this is not the case, the coincidence energy spectrum can be drawn. This way, multiple peaks can be fitted, which can provide an estimate for the background-to-true coincidences.

Due to the complexity of the spectrum, the photon energies that are in coincidence with the trigger photons are not solely in the energy range of the secondary coincidence photon. The photon energies that are in coincidence with the trigger photon for the ^{213}Bi and ^{209}Tl decay are shown in Figure 5.7 and Figure 5.8 respectively.

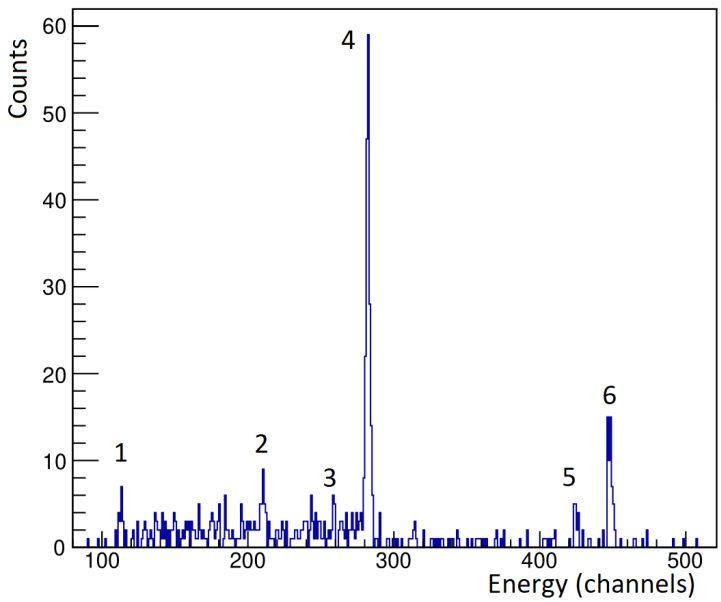

Figure 5.7: Channel numbers of coincidence photons following an 807 keV photon (corresponding to the ^{213}Bi trigger photon).

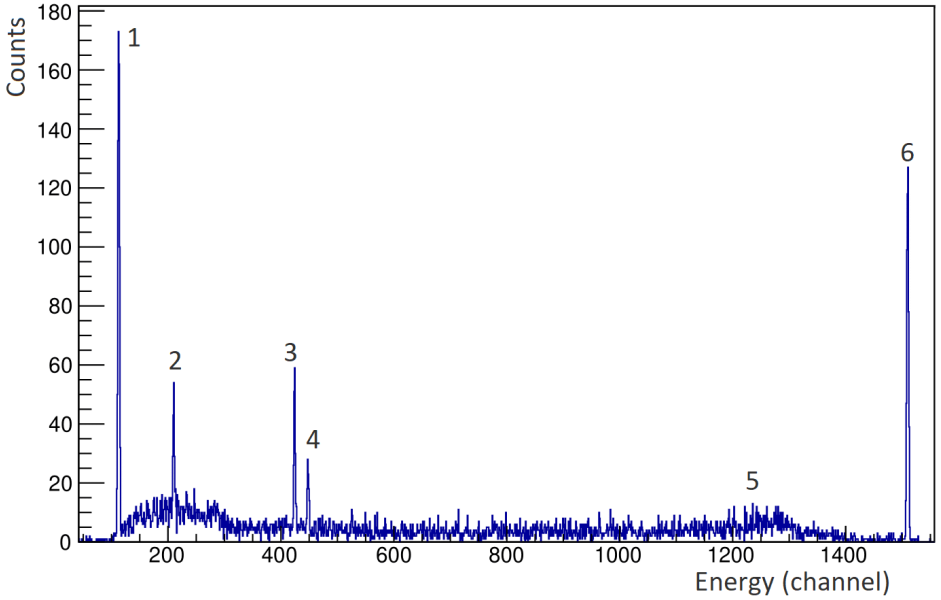

Figure 5.8: Channel numbers of coincidence photons following a 465 keV photon (corresponding to the ^{209}Tl trigger photon).

The channel number and energy in keV for these spectra are nearly the same. For the ^{213}Bi decay, 6 structures can be noticed in the coincidence energy spectrum. First of all, there is a peak around 293 keV (4), which is the expected coincidence energy. Furthermore, the Compton continuum of this peak is present as well (3). Around 218 keV (2) and 440 keV (4), small peaks are present. These are from random coincidences with the high-intensity peaks. Finally, there are peaks around 117 keV (1) and 465 keV (5). These are background coincidences following the 1567 keV photons originating from ^{209}Tl that deposited 807 keV in the detector after undergoing Compton scattering. This can be interpreted as a *false trigger* of the first photon.

In the ^{209}Tl decay, again 6 structures are present in the coincidence energy spectrum. Firstly, there is the 1567 keV peak (6) and its Compton continuum (5). Similar to the previous spectrum, random coincidences are present at 218 keV (2) and 440 keV (3). At the 465 keV, the energy of the trigger photon, another peak is present (4). This peak is present because the trigger photon was actually a Compton scattered 1567 keV photon. Finally, there is an intense peak at 117 keV. This is a true coincidence with both the 465 keV and 1567 keV photons. Even though there are a lot of coincidence counts, this coincidence is unsuitable for activity measurements. This is because the peak is hard to differentiate from the background, which means the counts in a single detector will be inaccurate. These last two peaks are again due to a *false trigger*.

5.4.2 Obtaining the EOC activity

Once the activities are obtained from chaining of data files, their mean times at which the activity was recorded are calculated, similar to the method used in Chapter 4. The data points are subsequently fitted using an exponential with a fixed half-life. The obtained fitting parameters are given in Table 5.1 and the fit itself is shown in Figure 5.9. Here A_0 denotes the EOC activity. The error on the activity obtained from the ^{213}Bi coincidences is dominated by the uncertainty on the intensity of the transitions, while the activity obtained from the ^{209}Tl coincidences is dominated by the uncertainty on the branching ratio.

Table 5.1: Fitting results for the activity of the coincidence measurements

Parameter	M108 (^{213}Bi)	M108 (^{209}Tl)	M120 (^{213}Bi)	M120 (^{209}Tl)
A_0 (kBq)	1143	993	938	839
error (%)	8.6	5.3	8.5	5.3
χ^2_{red}	0.49756657	0.50141727	0.52206883	0.50141727

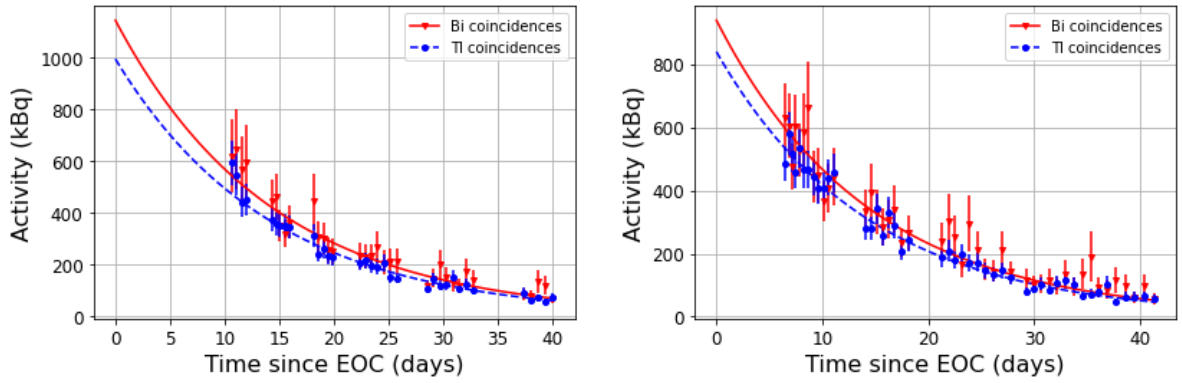

(a) (b)

Figure 5.9: Exponential decay fit for the γ-γ coincidence measurements for (a) M108 and (b) M120.

There is a clear systematic effect between the activities obtained from ^{213}Bi coincidences and ^{209}Tl coincidences. As the multipolarity of the trigger transition is not known and the secondary photon is already a mixed M1-E2 transition, this is likely caused by an angular correlation differing from 1 at 90°. Further studies of this angular correlation could be performed using specialized setups with high solid angle coverage. As the precision of the EOC activity obtained by the ^{213}Bi coincidences could not be guaranteed, the mean EOC activity was taken to be the one obtained from the ^{209}Tl coincidences. The residues and relative residues of the exponential decay fitting are shown in Figure 5.10.

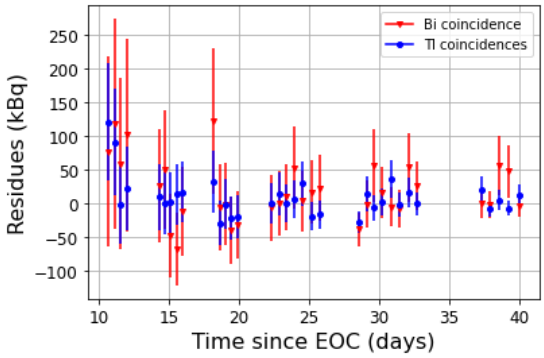

(a) Residues M108

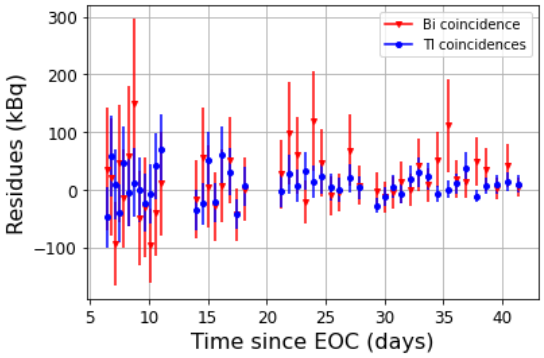

(b) Residues M118

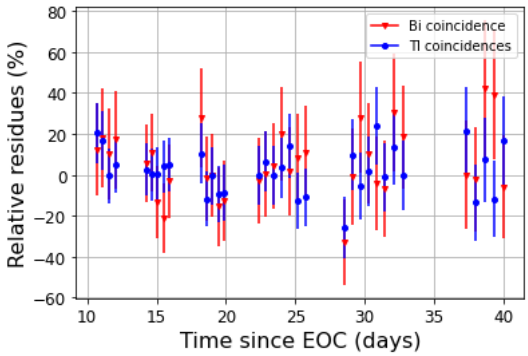

(c) Relative residues M108

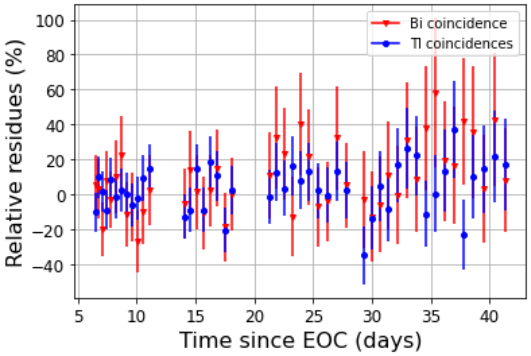

(d) Relative residues M118

Figure 5.10: Residues and relative residues for the exponential decay fitting of data from the coincidence setup.

The first batch of measurements of M108 has a systematically higher activity, which might be caused by inaccurate geometric arrangement. Besides that, the behavior of the residues is as expected. That is, slightly reducing in magnitude for the absolute residues while slightly increasing for the relative residues. For the final measurements using the ^{213}Bi coincidences, there are more outliers in the high activity region, which is due to the low number of coincidences at that time. The final EOC activities are shown in Table 5.2.

Table 5.2: EOC ^{225}Ac activity estimates from the coincidence setup, obtained via fitting with a fixed half-life

Foil	Initial activity (kBq)	Relative error (%)
M108	993	5.3
M120	839	5.3

6 Alpha-spectroscopy of a Long Decay Chain

6.1 Geometric Efficiency Simulations

For certain experiments where the intrinsic efficiency limits the total efficiency, such as γ spectroscopy, it is usually acceptable to work with a simple point source approximation. However, when particle detectors with near 100% intrinsic efficiency are used, such as silicon detectors in α-spectroscopy, or when more accurate results are needed, the geometric efficiency must be more accurately characterised. The geometric efficiency corresponds to the fraction of particles that are emitted compared to the amount of particles that reach the detector. In other words, the solid angle can be used to calculate the geometric efficiency, compared to an isotropic emission around 4π. For the experiments of this project, the geometry consisted of a foil and a circular detector. In the foil itself, there is some distribution of ^{225}Ac and its progeny. A picture of the foils is shown in Figure 6.1 (a), while a graphic representation of the geometry is shown in Figure 6.1 (b). The sample is a zinc coated gold foil with implanted ^{225}Ac. The surface of the foil was a $15(1)\,mm \times 25(1)\,mm$, while the thickness t of the gold and zinc layer were 0.25(3) mm and 500(5) nm respectively. The detector was a Si(Li) PIPS detector with a circular surface of $300\,mm^2$. For several of the models, the distance between the sample and the detector r, was kept as a free parameter.

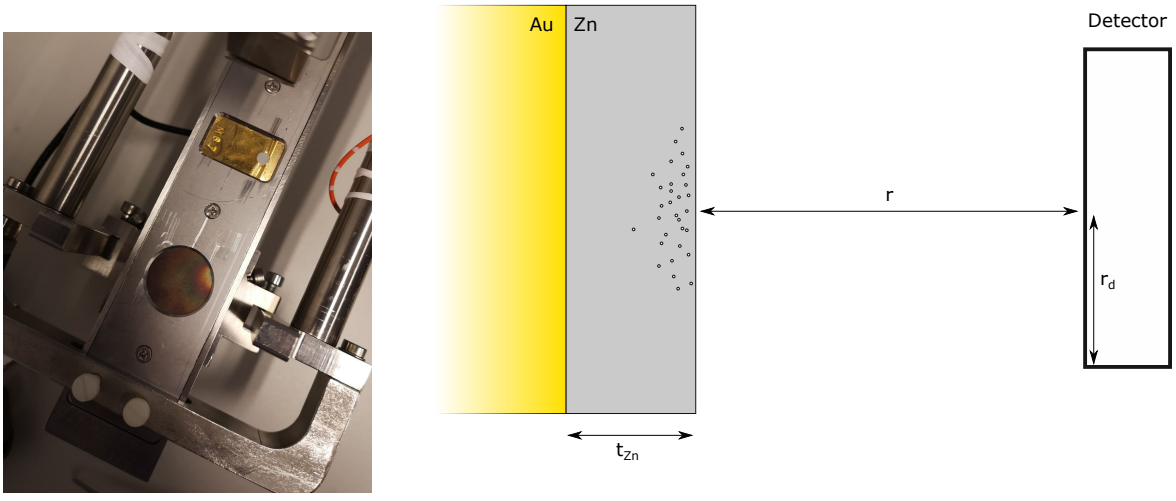

(a) (b)

Figure 6.1: (a) Picture of the foil placed inside the ladder and (b) Graphic representation of the considered source-detector geometry. The foil is shown on the left and the detector is shown on the right. For illustration purpose only, not to scale.

Three different types of models were created, each with their own advantages and disadvantages. All of the created models used a circular detector and a sample that was assumed to be completely parallel to this detector. Furthermore, the mean of the implantation spot was taken to be directly centered with respect to the detector. While the initial geometry assumptions are the same for all models, the treatment of the sample is drastically different.

Making an assumption about the type of the distribution of radioactive nuclei in the foils allows for analytic techniques to be used. Realistically, this can only be done quantitatively for simple geometries where stopping effects are minimal. In scenarios where no analytical solutions are readily found, numerical techniques can be applied. This is done in the first part of this chapter by using Monte Carlo integration after the integral form of the geometric efficiency is obtained. The advantage of this technique is that when the assumptions are met to sufficient precision, the solutions are universal. On the downside, stopping and decay chain effects will be impossible to study. There are also other numerical methods, which simulate a large sample size of incoming and outgoing particles by modeling the slowing and redirection of particles, which was done using SRIM. The power of this technique lies in the fact that most of the physical phenomena are taken into account, such as the slowing and complete stopping of particles. This also implies that a simulated energy spectrum can be obtained, which is not possible for the semi-analytical models. Furthermore, the model has the ability to account for the different distributions of the recoiling daughter nuclei in the decay chain. This is important, as each isotope in the decay chain will have a different geometric efficiency.

For the purpose of this thesis, two of these numerical models were created. The first is discussed in Section 6.1.2, while the other one is treated in Section 6.1.3. In the first model, SRIM (stopping and range of ions in matter) [34] was used to describe the trajectories of the particles. These are both α-particles and recoiling nuclei moving deeper within, or being emitted from the foil. Once this was done, the path vector and final position inside the foil of particles that leave the foil was tracked to extrapolate whether or not the particle hits the detector. Since the alphas coming from daughter nuclei decaying on the detector surface turn out to be a major contribution of the total signal, a recoil analysis was performed. This is a simplified way of dealing with the particles, that assumes which physical effects are acting on the particle with corresponding probability. This model will be referred to as the Numerical Recoil Analysis Model (NRAM). Its advantage over the second numerical model lies in the possibility of studying the distance dependence as well as allowing a separate evaluation of the different contributions, which can be used to compare them to each other. Those can be either simple differences, such as decays of atoms from in the foil and decays from recoiling particles caught onto the detector, or more complicated processes, as will be mentioned in the NRAM. Following this, the other numerical representation, namely the Full Numerical Model (FNM), is explained. This model describes the entire geometry of the system in SRIM, such that there is no distinction in *escape mechanisms*. Since less assumptions have to be made about physical processes that the daughter nuclei can undergo, the model should describe the overall geometric efficiency better. Therefore, the geometric efficiencies obtained from the FNM were used for the α-spectroscopy analysis.

Although it was not performed for this project, it is also possible to use a hybrid of the two numerical models. This could simulate the α-particles and recoiling daughters from an initial distribution in the foil. Following this, the path vectors are taken as input for radiation incident on the detector. In this way, the detector can be treated separately. This includes dead layer effects and the energy loss in the active region of the detector. Although this type of model can be made to represent reality in a very accurate manner, the complexity of the modelling increases rapidly due to the long decay chain.

6.1.1 Semi-analytical model

6.1.1.1 Simulation method

When the energy losses and redirection of particles are neglected, some approximations can be made. To zeroth order, the distribution is approximated as a point source, but besides this models were made for a uniform circular and a 2-d Gaussian source which shall from now on be referred to as the uniform and Gaussian models respectively. These distributions correspond to a surface density of radioactive particles. The mathematical derivations for these models can be found in Appendix D. It should be noted that the integrals that arise from the solid angle are impossible to solve analytically since the integrand diverges as the integration variable k approaches zero. Therefore Monte Carlo integration based on Riemann sums was used for a range of distances as is briefly explained in Appendix D. In general, the integral can be obtained by using Eq. (6.1). Here N denotes the number of randomly generated points and $W(x)$ represents a normalised distribution out of which the random numbers are chosen. The latter of these should only be nonzero inside the interval $[a,b]$.

$$\int_a^b f(x)dx = \frac{1}{N}\sum_{i=1}^{N}\frac{f(x_i)}{W(x_i)} \tag{6.1}$$

This distribution function can be a uniform distribution for slowly varying functions, but if this is not the case, increasing amounts of random numbers will have to be used. To accommodate for this, a different distribution can be used, for which $\frac{f(x)}{W(x)}$ is slowly varying. This corresponds to picking more numbers in the fast varying part of the function. This concept is referred to as *umbrella sampling* [35]. Given the form of the integrands, namely having exponential and Gaussian factors, a logical choice is to use exponential and Gaussian random number generators (RNG). In general, this remainder is indeed quite slowly varying but for the k-integration at short distances compared to the detector radius, the standard deviation on the integral is still quite large. To accommodate for this, the number of used points is increased to 10 times and 100 times the normal amount when the distance becomes less than 0.5 and 0.05 of the detector radius respectively. If even closer distances have to be considered, this would have to be increased again to guarantee a sufficiently low error margin. A more general method might be to multiply the chosen amount of numbers by a dsitrbution function proportional to $\frac{r_s}{r}$ which will not give an abrupt step-like behavior.

While the simulation itself was performed with the detector dimensions that would be used in the experiments ($300\,mm^2$), it is useful to perform a rescaling to units of the detector radius. When this is applied to obtain dimensionless values for the source radius/standard deviation and the source-detector distance, the obtained geometric efficiency functions are valid for all circular detector systems. To check the validity of the results, the value of the geometric efficiency can be checked near and far from the source, as it is possible to solve analytically for the used source models.

6.1.1.2 Results and discussion

Now that the concept of the model has been explained, it is time to look at the results. The resulting graphs comparing the uniform model to the point source approximation are given in Figure 6.2. It is clear that for positions far from the source, the efficiency should converge to that of the point source approximation as the radius of the source becomes negligible compared to the distance between the source and the detector. In the uniform model, the efficiency should converge to $\varepsilon_{geo} = \frac{1}{2}$ as long as the circular source is smaller than the detector. Once this is no longer the case, its convergence value is given by Eq. (6.2). This happens because only the part of the source with a distance to the center of the source smaller than the detector radius can contribute. In this formula, A_d and A_s denote the area of the detector and the source respectively.

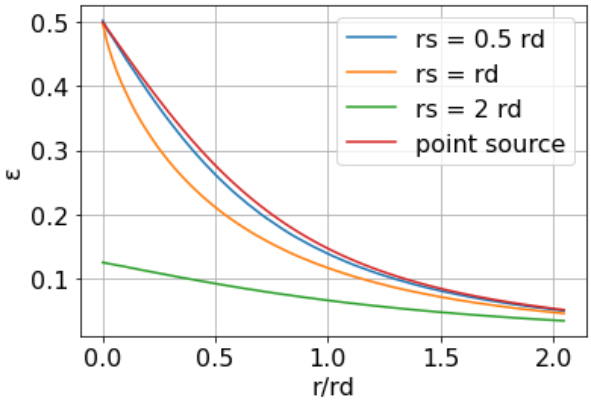

Figure 6.2: Geometric efficiency as a function of distance from the detector in units of the detector radius r_d, for different source radii r_s, of a circular uniform source on a circular detector. The results were obtained by Monte Carlo integration using at least 10^7 randomly generated numbers per point.

$$\varepsilon_{geo} = \frac{A_d}{2A_s} \tag{6.2}$$

It can be seen that the behavior in the extreme points follows the expectations adequately. When the source radius is less or equal to the detector radius, $\varepsilon_{geo} \to 0.5$. For the case where the source radius is twice that of the detector radius, ε_{geo} has a maximum value that is about $\frac{1}{8}$, which is equal to the prediction for large sources in Eq. (6.2). In fact, the only thing limiting the precision of a specific distance is the computation time. As the distance increases, the required amount of random numbers for a given precision does so as well. After a distance of a couple of r_d, even the green curve ($r_d = 2r_s$) is quite close to the point source approximation. After initially starting at 25% of the point source approximation, it has increased to 66% of the point source approximation in only $2\,r_d$. For the case where the source radius is less or equal to that of the detector radius, the region of maximal discrepancy occurs for distances between 0.05 and 1.2 r_d (efficiencies between 10% and 45%). Even though this calculation is only approximative, since uniform circular distributions are not practically realisable with infinitely sharp edges, it can give a general idea in what region the point source approximation can be used.

Alternatively, this approach could be useful in circumstances where the spread of particles in the source is not known accurately. Staying within an absolute error of about a percent on the geometric efficiency, the point source approximation can always be used for sources with a radius less than half of that of the detector. An important thing to realize in these graphs is that a distance 0 is not defined for the integrand which means Monte Carlo integration breaks down. To account for this, the range was limited to values above $10^{-2}\,mm$ corresponding to about $10^{-3}\,r_d$. Finally, an interesting observation is that the point source approximation always overestimates the geometric efficiency for a circular uniform sample. To make the model a bit more realistic, a circular Gaussian distribution was used as a surface density $\rho(r)$, as shown in Eq. (6.3). Here r is the distance from the center and σ is the standard deviation, which is assumed to be symmetric with respect to the polar angle.

$$\rho(r) = \frac{1}{2\pi\sigma^2} e^{-\frac{r^2}{2\sigma^2}} \tag{6.3}$$

A Gaussian surface distribution is quite a good approximation to the realistic cases, in which beams of near-Gaussian profile implant radionuclei. This was also the case for the implantation performed at MEDICIS. However, it still does not incorporate *special effects*, such as backscattering. The general calculations in Appendix D are also valid for more general normalized axially symmetric source distributions which means the model could still be improved for specific circumstances as long as the distribution function does not diverge. The resulting graphs comparing the geometric efficiency to that of the point source approximation are shown in Figure 6.3. Henceforth, the radius of the source will be estimated to be 2 standard deviations of the 2-d Gaussian.

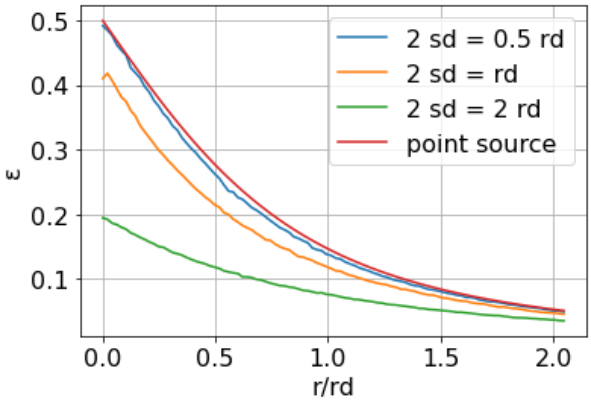

Figure 6.3: Geometric efficiency as a function of distance from the detector in units of the detector radius r_d, for different source spreads r_s, of a circular Gaussian surface distributed source on a circular detector. The results were obtained by Monte Carlo integration using at least 10^2 and 10^6 random numbers for the r- and k-integration respectively.

It can be observed that the behavior is relatively similar to the uniform circular source. The main difference that can be seen in this plot is that for all possible standard deviations of the Gaussian (larger than 0), there is always a piece of the source that will not be in contact with the detector when the source-detector distance goes to 0. This causes the maximal efficiency to drop below 50%, even for sources smaller than the detector. However for sources that are larger

than the detector, the efficiency at small $\frac{r}{r_d}$ increases compared to the uniform model. This can be understood by noting that the concentration of particles in the area of interest is slightly higher for the Gaussian compared to the uniform source. In Appendix D, the exact result for the geometric efficiency at a distance 0 is given. The agreement between the theory and the calculations is very good for both small and very large distances, again seemingly only limited by statistical fluctuations and the difference from 0 implemented to counteract divergences. This suggests that the calculations are indeed reliable.

The two models may also be compared with each other. As mentioned earlier, the uniform circle with radius r_s is compared to the Gaussian with standard deviation $r_s/2$. It is then possible to plot the difference between the two models as a function of distance from the detector in Figure 6.4. In this graph, there is a statistical fluctuation of less than a percent (absolute). This is mainly coming from the fluctuation on the Gaussian model as it requires significantly more computation time to due the additional integration over r. A check that can be done is that the difference should go to 0 for large distances as they both converge to the point source approximation. Since it was possible to calculate the theoretical value at $r = 0$ for both models, the difference between the two models at the detector can be done as well.

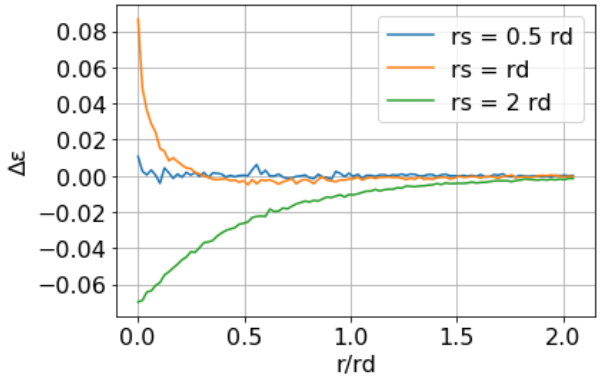

Figure 6.4: Difference of the geometric efficiency of the uniform model and the Gaussian model as a function of distance from the detector in units of the detector radius *rd*. The results were obtained by Monte Carlo integration using at least 10^7 random numbers for the uniform model, while the Gaussian model had at least 10^2 and 10^6 random numbers for the r- and k-integration respectively.

The behavior of the difference between the models for different source radii is quite interesting. For very small source radii the difference is negligible as both models are very well described by the point source approximation. When the source radius increases, the circular source has a higher geometric efficiency while its radius remains less than or equal to that of the detector. However, when the source radius becomes larger than the radius of the detector, the Gaussian source has a higher efficiency than the uniform source. Using the determined geometric efficiency for the distance to the detector going to 0 for both models, it is straightforward to determine the difference between the models, $\Delta\varepsilon(0)$, in this point as a function of source radius. The result is given in Eq. (6.4).

$$\Delta\varepsilon(0) = \begin{cases} \frac{1}{2} e^{-\frac{2r_d^2}{r_s^2}} & \text{for } r_s \leq r_d \\ \frac{1}{2}\left(\frac{r_d^2 - r_s^2}{r_s^2} + e^{-\frac{2r_d^2}{r_s^2}} \right) & \text{for } r_s > r_d \end{cases} \tag{6.4}$$

This theoretical function was plotted in Figure 6.5. It is in a good agreement with the results from Figure 6.4. The function itself indicates that in the interval $r_s = [0.5; 10] r_d$, in which experiments occasionally occur, the Gaussian model adds a correction in the order of a percent to the calculation for very small distances. Depending on the source radius, the contribution can either be positive or negative.

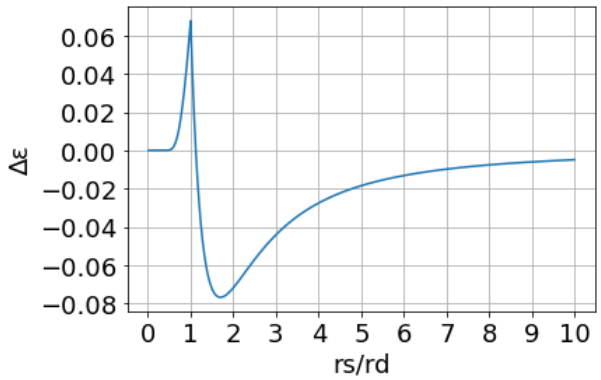

Figure 6.5: Eq. 6.4 plotted for the difference in geometric efficiency at $r = 0$ as a function of source radius r_s, rescaled to the radius of the detector r_d, for source radii up to 10 r_d.

6.1.1.3 Realistic geometric efficiency estimate

For estimations of the surface distribution of the ^{225}Ac in MED-024, an implantation profile has to be taken into account. Since these processes are by themselves not trivial at all, the ^{225}Ac distribution in the zinc-coated gold foil (Au/Zn) was modelled using SRIM with the add-on SSSM to obtain the result of real beam profile [36]. As SRIM defines the x-direction as parallel to the beam, it was done here as well. The obtained implantation profile is shown in Figure 6.6.

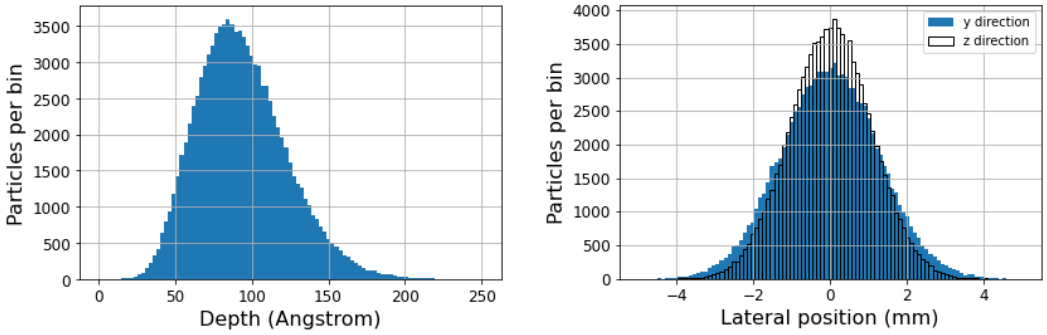

(a) (b)

Figure 6.6: (a) The depth profile and (b) lateral distribution of the implantation of ^{225}Ac at 60 keV using real beam parameters.

It can be observed that the lateral distribution is Gaussian in the y- and z directions, but not symmetric. To make an approximated distribution, the standard deviations in the directions orthogonal to the beam were used to obtain the polar standard deviation as given in Eq. (6.5). This method approximates a yz-asymmetric polar Gaussian by a perfectly symmetric polar Gaussian. Particles that have a y or z component which exceeds the foil are removed from the system. In this equation, σ denotes the polar standard deviation, while σ_y and σ_z represent the y- and z standard deviation respectively.

$$\sigma^2 = \sigma_y^2 + \sigma_z^2 \tag{6.5}$$

In MEDICIS the ^{225}Ac ions were implanted at 60 keV. This implantation profile can then be modeled by the Gaussian distribution or approximated circular distribution. The standard deviations for the y- and z-direction of the beam were 1.28 cm and 1.06 cm, obtained by the beam profiler, while the standard deviations of the ^{225}Ac in the foil were calculated by SRIM with the real beam profile to be the same within about 10 nm. This difference is negligible compared to the source spread from the beam. The polar standard deviation for the implantation is about 1.175 cm. Therefore the models have to be performed for $\sigma = 1.175\,cm$ and $r_s = 2.349\,cm$ for the sources. The resulting difference in geometric efficiency compared to the point source approximation for both models is shown in Figure 6.7. In the region of interest, the difference from the point source is about 0.04% (0.8% relative) while the maximal difference is only about 0.3% (1.5% relative). The Gaussian and circular source are nearly indistinguishable in this geometry. It should be noted that any fluctuation in these graphs is not from physical origin, but are a construct of insufficient calculation time in the numerical technique. If high precision γ-spectroscopy would be performed with similar geometry, this could be used for precise measurements. However, for this project, the effects of stopping power turn out to be more important.

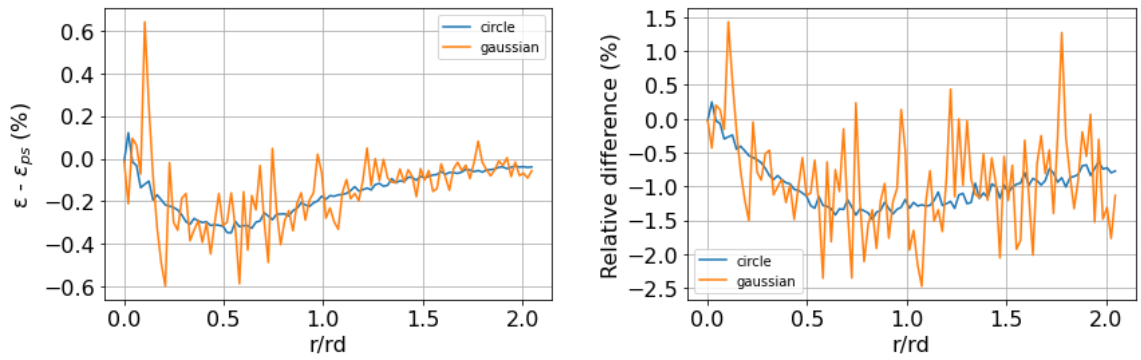

(a) (b)

Figure 6.7: a) Absolute and b) Relative difference between the models and the point source.

The final important remark to make here is that this geometric efficiency estimate is only good for the ^{225}Ac decay, as the other decays will have different spreads. There are two contributions that will induce a spread more significant than the spread due to stopping in the implantation. First of all, the implantation occurs at 60 keV, while the recoiling particles have energies of order 100 keV. Besides this, the decay occurs isotropically, while the implantation doesn't, causing more lateral movement. The obtained standard deviations can either be put directly into the Gaussian model or multiplied by a factor 2 to provide an estimate of the radius of a circular source. As effects caused by particle collisions are more important, it is convenient to move towards more numerical techniques.

6.1.2 Numerical recoil analysis

6.1.2.1 Simulation method

The second model uses several steps to discuss multiple α-decays in the decay chain by using SRIM simulations in multiple layers. Similar to the implantation in the previous part, SSSM was used to simulate the implantation profile for ^{225}Ac on a zinc-coated gold foil. After this, a series of steps were made to turn outputs into new input files to eventually get a simulated energy spectrum and the estimated geometric efficiencies of each decay. Since only α-particles will be detected and the recoil energy for β-decay is small, the recoiling for β-decay can be neglected. Once this is done, a convolution of delta peaks at the detected energies is made with a Gaussian detector response to obtain an expected α energy spectrum. The latter was done by adding random numbers from a normal distribution that matched the resolution of the detector. One of the main advantages of this method over the FNM is that the contributions of different mechanisms can be separated, which can help to understand the physical processes. Besides this, the distance between the source and the detector does not have to be known before the simulation starts. The decay chain is discussed thoroughly in Chapter 3.

The simulation can be divided into several layers for the different decays. Each layer consists of SRIM simulations for the new distribution of the recoils and the transmission of all particles out of the foil, followed by an analysis for the α-particles and the recoiling daughter nuclei. This is done by the generation of the specialized .dat files as input for SRIM. Each of these input files has 4 major components, namely the atomic number of the ion, the energy of the ion, the location it starts at, and its direction. For the first layer, the implantation profile describes the initial positions. The subsequent layers use the final positions of the previous layer as implantation profile. For the first layer, the atomic number is 2 for the α-particle while it is 87 for the recoiling ^{221}Fr atom. The energy for the alpha is given by the Q-value of the decay while the energy of the recoil is determined using conservation of momentum. The fine structure branchings were disregarded for simplicity. Since the linewidth of the state is sufficiently small compared to the energy loss in the material and the detector resolution, it was neglected. The final aspect to put in the file is the initial direction of particle movement. For the α-particles, this is done by creating an isotropic spherical distribution by using the inverse cumulative distribution function method, for which the calculation is shown in Appendix E. For the recoiling nuclei, this is simply the opposite direction of the corresponding α-particle. The isotropic emission is visualized in Figure 6.8 using an implantation of ^{225}Ac in a zinc-coated gold foil starting from a depth of $1\,\mu m$.

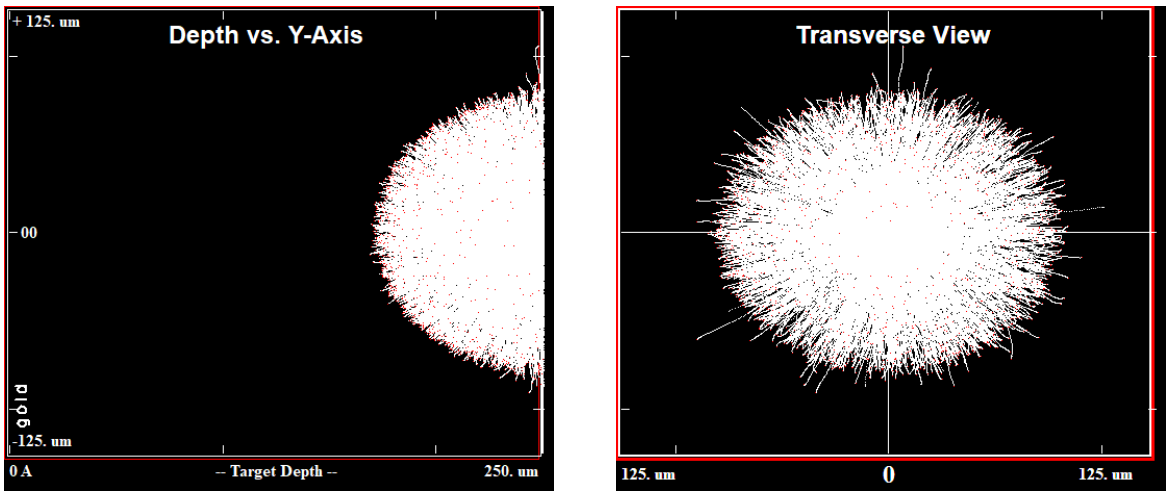

(a) (b)

Figure 6.8: (a) Depth vs y-axis and (b) transverse view of ^{225}Ac being sent out isotropically from inside a zinc-coated gold foil from a depth of $1\mu m$.

The first layer considers the implanted ^{225}Ac decaying to ^{221}Fr. The final position of the recoiling nuclei can then be used for the next layer. Similarly, the subsequent α-decays can be done in succession. Besides keeping track of the α-particles and the final positions of the recoiling daughter nuclei in the foil, a detailed recoil analysis has to be performed. If a recoil exits the foil and is subsequently implanted, or *caught*, on the detector, it can decay and send its α-particle into the detector. This is defined as an *accepted* recoil. Alternatively, the α-particle can be sent away from the detector, which is defined by a *rejected* recoil. The recoils have to be considered using a combination of extrapolation principles and source approximations. For this, methods fully based on Monte Carlo methods were used to decide if a decaying recoil is accepted or not by making simplified mechanisms.

After the first implantation, the foil is flipped, which is done because the SRIM output for the transmission of particles is defined as particles moving out of the foil in the positive x direction, while the implantation was done from the left side. Subsequently, the alpha particles escaping the foil in the direction of the detector are calculated. The final position and direction of the particle are used to extrapolate the position it would have when it reaches the position of the detector. If this is within the radius of the detector, it is assumed the particle will be detected, which can be corrected by using a separate intrinsic efficiency. The energy of the detected α-particle is then given by the energy it had when it exited the foil, which is less than the exact energy of the decay due to stopping effects. A visual aid to understand the different types of processes in this part is shown in Figure 6.9. Notice that particles can penetrate several microns into the gold foil, which caused long simulation times.

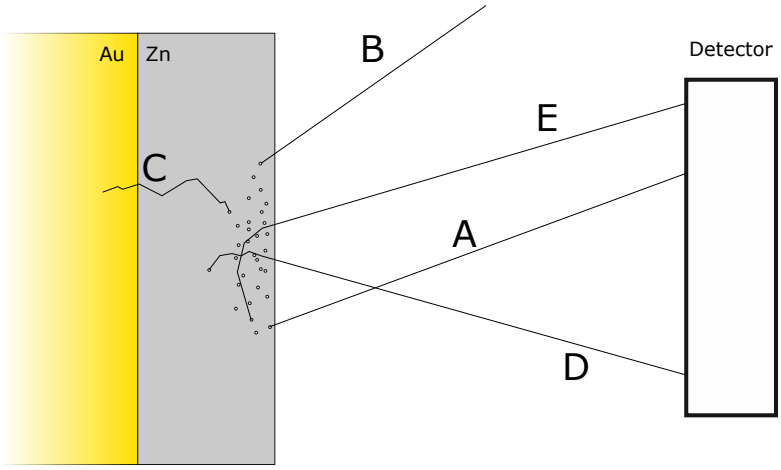

Figure 6.9: Schematic representation of the different alpha particle trajectories. A) Starting shallow, losing only a small amount of energy before being detected. B) Sent out of the foil, but missing the detector. C) Moving away from the detector. D) Starting deep, losing a large amount of energy before being detected. E) Detected after initially moving away from the detector.

The number of particles with corresponding energies are kept, such that the total energy spectrum for the decay-chain can be obtained after all layers are finished. The counts of the different decays can be tracked through the particles that end up in the detector. The geometric efficiency is then equal to the number of particles in the detector divided by the total amount of particles simulated. Later in the discussion of the simulation results, it will become clear that very close to the foil, the geometric efficiency even surpasses 50%. This happens because the direction a particle moves in can be changed drastically. As particles near the surface will move out of the sample before they have a chance to move deeper due to backscattering, the effect is more prominent out of the sample.

As mentioned before, the simulation for the recoiling francium has two main reasons. The first is to find the new positions of the radioactive atoms inside the sample, so another step of alpha decay can be modeled. The second reason is that since the recoiling ^{221}Fr has a much higher energy than the implantation energy (by about a factor 2), it has a high probability to escape the foil. Once this happens, the atom can be implanted on the detector until it α-decays. This is defined as being *caught* onto the detector. To model this, transmission results from SRIM were used similarly as before and the α-decays are accepted into the detector with a probability 0.5, which assumes the particles do not change direction. One has to keep in mind that this is a simplification, however, it should describe the general process. A visual aid for the different processes is shown in Figure 6.10.

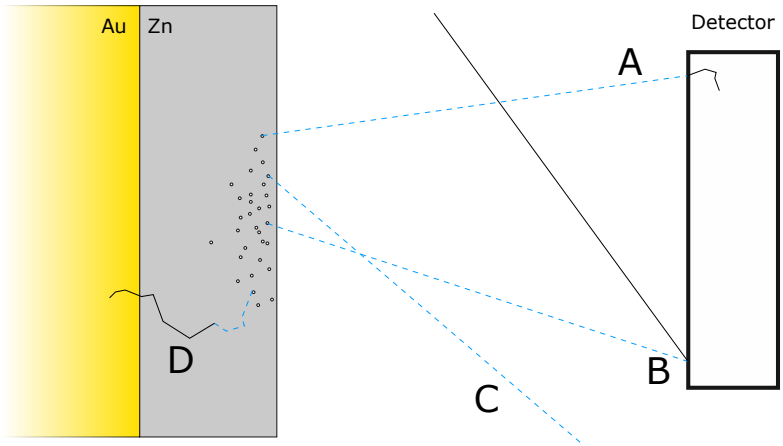

Figure 6.10: Schematic representation of the different ^{221}Fr trajectories. A) Hitting the detector and accepting the α-particle. B) Hitting the detector and rejecting the α-particle. C) Missing the detector. D) Moving away from the detector and sending out an α-particle in a random direction. The solid black lines represent alpha particle trajectories while the dashed blue lines represent ^{221}Fr recoils.

Another contribution for α-particles in these recoiling nuclei is from the secondary recoils, namely ^{217}At. The first process is sending an α-particle inwards after a ^{221}Fr-decay, which makes the ^{217}At recoil deeper into the detector. Besides this, a ^{221}Fr recoil can send a recoiling ^{217}At atom back towards the foil, which subsequently can emit α-radiation from inside the sample. As a simplified model, this was calculated assuming a *ping-pong effect*, in which the ^{217}At is deposited only on the surface of the foil. The α-particles from this process are then calculated by using two point-source approximation for the recoiled ^{221}Fr atoms, which is expected to give a slight overestimation of the effect (from the results of the semi-analytical models). This means the probability of ^{217}At atoms recoiling out of the detector and subsequently being accepted $P_{R,A}$, is given in (6.6). Here r and r_d are the detector-source distance and the detector radius respectively.

$$P_{R,A} = 2\left[\frac{1}{2}\left(1 - \frac{r}{\sqrt{r_d^2 + r^2}}\right)\right]^2 \tag{6.6}$$

This equates to 2 times the point source geometric efficiency squared. The factor 2 comes from the fact that only the ^{217}At that is already going backwards is considered for this process. Besides this, the energy loss of these α-particles is also neglected through the assumption which would be solved by fully modeling the detector in SRIM. A graphic presentation of the trajectories for the astatine from the ^{221}Fr recoils in the detector are shown in Figure 6.11. Initially, it was thought that the ^{225}Ac layer of the simulation ended there, but later it became clear there are still more contributions due to increasingly complex mechanisms that become a worse description of reality.

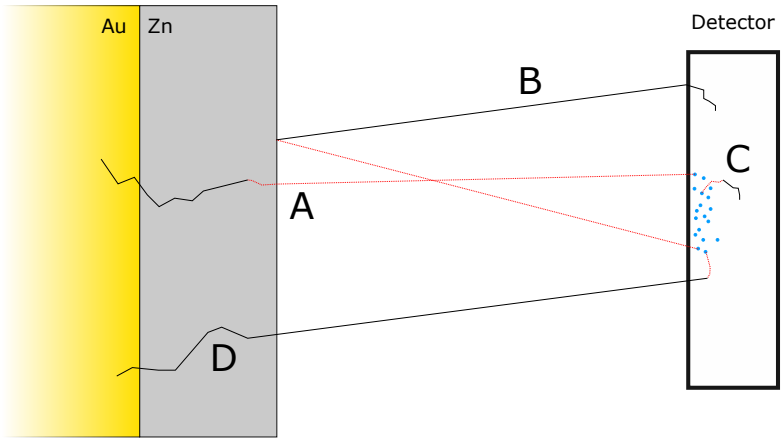

Figure 6.11: Schematic representation of the ^{217}At trajectories. A) Leaving the detector and sending out an α-particle away from the detector. B) Leaving the detector but accepting the α-particle anyway (ping-pong effect). C) Moving deeper into the detector accepting the α-particle. D) Moving deeper into the detector but rejecting the α-particle. The solid black lines represent α-particle trajectories while the dotted red lines represent ^{217}At recoils. The blue dots represent the ^{221}Fr recoils that have been deposited on the detector.

Once the implantation profile of ^{221}Fr in the foil is known, the ^{221}Fr layer of the simulation can begin. The procedure can be executed again but this time for α-particles of the energy of the ^{221}Fr $\rightarrow$ ^{217}At decay and the corresponding ^{217}At recoils. The direct alpha particles are then added to the alpha decays from the exiting ^{221}Fr recoils for the total amount of ^{221}Fr decays. The ^{217}At recoils again undergo a similar recoil analysis as the ^{221}Fr of the previous layer. This obtains a fraction of α-decays coming from the recoiling ^{217}At atoms that are coming out of the foil while the ^{213}Bi and ^{213}Po are treated the same as the secondary recoils in the previous layer of the simulation. Since ^{213}Bi has two branchings (α-decay of 2.2%), an additional random number is used to *choose* the decay path. After this, the process was done again for the ^{217}At layer of the simulation, discussing ^{217}At $\rightarrow$ ^{213}Bi α-decay using the newly obtained ^{217}At-distribution. This step obtains the final contribution of the total number of ^{217}At α-decays. Finally, the ^{213}Bi-distribution was used for the ^{213}Bi and ^{213}Po layers of the simulations. The other steps are completely equivalent to what has been dealt with up until now, which is why it will not be discussed in detail. The only differences arise from the ending decay chain, which means some mechanisms have no contributions.

After the results of the simulations were obtained, it was noticed that the ^{213}Bi and ^{213}Po geometric efficiency was significantly lower than the other isotopes, which is caused by tertiary recoil effects in the ^{225}Ac-layer of the simulation. Two major parts should make up the ^{213}Bi and ^{213}Po part of this layer. First of all, there are general simplistic aspects in the model. This consists of in-flight recoil decay and particles that are considered *out of the system*. The former happens when a recoiling particle decays before coming to a stop which mainly affects short-lived isotopes. Even for these isotopes, the distance the recoiling daughter nuclei move away from the detector before decaying is quite large. Therefore, this contribution should be minor. Furthermore, particles can never be completely out of the system before decaying. In reality, they can be implanted on, or scatter against, the chamber walls or other structures, which could still lead to a detection afterwards. Again, this contribution is not expected to be large.

The second set of contributions is caused by the lack of detail in the recoil analysis for the ^{225}Ac-layer which provided a major difference with the previous results. Within this recoil analysis, there are mechanisms after ^{217}At is implanted on the detector or when it has been again deposited on the surface of the foil within the ping-pong effect. The former again includes a delayed ping-pong effect in which the primary recoiling nucleus comes onto the detector, the secondary stays within the detector and the tertiary is finally sent back to the surface of the foil. After this, an α-particle can be sent back to the detector. The latter, on the other hand, occurs when the ^{217}At α-particle is sent into the foil after undergoing the first part of the ping-pong effect. Finally, there is acceptance of ^{213}Bi or ^{213}Po after rejecting ^{217}At with a probability of 0.5. Even though these processes seem minor, the results show that a quite large contribution arises from them.

6.1.2.2 Simulation results

Now that all the concepts of the simulations have been explained thoroughly, the obtained results can be discussed. The first thing that was checked was the number of particles that come into the detector at a distance 0 which is done to see if stopping or backscattering is in this case the dominant effect. In general, one would expect the geometric efficiencies to be around 50 % at this point. The resulting values for the model not including the tertiary recoil effects in ^{225}Ac are shown in Table 6.1. Here the direct detection is the fraction of the detected α-particles that are released from a nucleus decaying within the foil. Since a decay path was modelled using random numbers for the ^{213}Po and ^{213}Bi, the obtained number of particles was still divided by the branching ratio of the decays.

Table 6.1: Geometric efficiency and direct detection at the surface of the foil obtained via layered SRIM simulations at a 0 source-detector distance.

Isotope	geometric efficiency (%)	direct detection(%)
^{225}Ac	52.576	100
^{221}Fr	51.063	47.6
^{217}At	50.795	35.0
^{213}Bi	22.703	61.4
^{213}Po	23.619	62.9

It can be observed that, besides ^{225}Ac, all isotopes have a large part of the geometric efficiency originating from the nuclei that recoil out of the foil. Since the ^{213}Bi implantation profile was used for ^{213}Po as well, one might wonder why they are different. Even though backscattering is less prominent for higher energies, the smaller energy of the ^{213}Bi might make it harder for backscattered particles to escape the foil. Looking at these results, it becomes clear that the ^{213}Bi and ^{213}Po provide geometric efficiencies much lower than expected. Although it seems at first that these have a much higher direct detection, it should be noted that the ^{225}Ac decay layer of the simulation did not include contributions to them yet. Since these are left out of the system, a quick estimate of the geometric efficiency of the remaining particles in the foil can be made by dividing the geometric efficiencies obtained here by the fraction of ^{221}Fr particles remaining in the foil, which is about 46.4%. The latter brings the geometric efficiencies from ^{213}Bi and ^{213}Po up to 48.9% and 50.9% respectively. However, this is not per particle of ^{225}Ac as the others. As this value should be around 50%, these estimates are a lot more realistic than the first order simulation.

When the recoil analysis is extended to the tertiary effects in the ^{225}Ac-layer, the total geometric efficiencies at the surface of the foil are given in Table 6.2. Since it could provide a better understanding, the different contributions for the geometric efficiency of the isotopes of interest and the fraction of particles that have not yet moved out of the foil up to each simulation layer are also shown. There is a clear decreasing trend of the direction detection fraction, which is because more recoils exit the foil in each layer, leaving fewer atoms to decay from within the foil. The direct detection percentages show just how crucial the inclusion of the recoil analysis is.

Table 6.2: Different contributions of the geometric efficiency at the surface of the foil and remaining implantation fractions obtained via layered SRIM simulations and recoil analysis at a 0 source-detector distance.

Isotope	^{225}Ac	^{221}Fr	^{217}At	^{213}Bi	^{213}Po
ε_{geo} (%)	52.576	51.063	50.795	49.493	50.401
Direct detection (%)	100	47.6	35.0	28.2	29.5
Accepting primary recoil (%)	/	52.4	12.3	5.1	5.0
Accepting secondary recoil after rejection(%)	/	/	26.4	6.3	6.3
Ping pong of secondary recoil(%)	/	/	26.4	6.3	6.3
Tertiary recoil effects (%)	/	/	/	54.1	53.1
Remaining implantation (%)	100	46.4	33.6	28.8	28.8

Consequently, it can be seen that initially a large fraction of daughter nuclei exit the foil. Afterwards, as the average depth of the remaining nuclei increases, fewer nuclei can recoil outwards. While over 53% is ejected in the ^{225}Ac-layer, only 27.6% of the remaining particles are ejected in the ^{221}Fr-layer while only 14.3% of the remaining particles are ejected in the ^{217}At-layer. At this distance, all contributions to the geometric efficiency have a similar order of magnitude. The tertiary recoil effects in the ^{225}Ac-layer of the simulation is a major contribution in the total activity for ^{213}Bi and ^{213}Po, even surpassing 50% of the total efficiency (or an absolute 25%). This is to be expected, as more than half of the recoils move out of the foil and roughly half of them are detected via tertiary recoils. However, the relative contributions do not scale similarly. A simple example of this is that the ping-pong effect essentially jumps three times between the foil and the detector, which is less likely at larger distances than a direct detection or a recoil caught on the detector. A good estimate for the scaling on this term would be r^{-6}, corresponding to the cube of the point source approximation.

To study the distance dependence, the geometric efficiency was plotted as a function of the rescaled source-detector distance. This is of main importance when determining what position has an acceptable count rate that does not cause too much dead time ($\lesssim 10 kHz$). Besides that, it provides a good comparison of the general shape of the geometric efficiency. The resulting graph is shown in Figure 6.12.

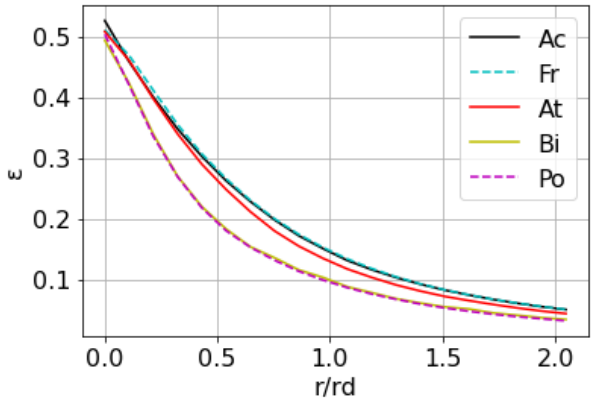

Figure 6.12: Geometric efficiencies of the present α-decays obtained by layered SRIM simulations.

Certain of these geometric efficiency values had a rather high fluctuation on the recoil analysis part due to the small number of specific events at certain distances which is why a loop was made to decrease them and provide a smoother distance dependence. The ^{225}Ac and ^{213}Po curves are rather hard to see as they are very similar to ^{221}Fr and ^{213}Bi respectively in terms of geometric efficiency. For the ^{221}Fr, the recoil analysis scales essentially the same as direct α-particles causing the shape to be very similar to the ^{225}Ac. This is because recoiling nuclei at a shallow depth have approximately the same probability to get caught onto the detector. The ^{217}At curve drops slightly faster than the ^{225}Ac ,and ^{221}Fr, which is because of the more extreme scaling of the ping-pong effect. This effect is then again amplified for the ^{213}Bi and ^{213}Po, in which the complex tertiary mechanisms have a strong dependence on r. Therefore, only the more simple and slower scaling effects, such as accepting a recoil after two rejections, remain. Another interesting observation is that the shape of the curve and the region of maximal discrepancy is similar to the semi-analytical models.

As the count rate would initially cause a large dead time correction (as estimated from the graph), the maximal distance allowed by the alpha measurement setup, namely 20.285 mm (about 2.08 r_d), was used in the experiments. The geometric efficiencies and their individual contributions are shown for this distance in Table 6.3. The table shows that most of the recoils have less effect when the distance increases which is mainly because of the more extreme distance dependence of secondary and tertiary recoils as expected. Especially counts due to ping-pong effects are much less prominent. As there were many complex contributions to the tertiary recoils they will not be individually discussed. The major contribution at this point should be due to accepting an α-particle after two rejections. It is possible to estimate this by taking half of the absolute geometric efficiency coming from the accepting secondary recoils after rejection. This is equal to 0.659%, equivalent to about 98.9% of the total geometric efficiency coming from tertiary recoils (0.667%). It is interesting to see that the direct detection for ^{213}Po is initially higher than for ^{213}Bi, but at a further distance, this is reversed. Another unexpected effect is that the efficiency for ^{221}Fr temporarily surpasses the geometric efficiency for ^{225}Ac. No physical explanation could be found for these effects.

Table 6.3: geometric efficiency and direct detection at a distance of 20.285 mm from the foil obtained via layered SRIM simulations including additional recoil effects.

Isotope	^{225}Ac	^{221}Fr	^{217}At	^{213}Bi	^{213}Po
ε_{geo} (%)	4.863	4.896	4.238	3.284	3.103
Direct detection (%)	100	46.3	39.8	45.6	43.0
Accepting primary recoil (%)	/	53.7	28.6	15.2	15.7
Accepting secondary recoil after rejection(%)	/	/	31.1	18.5	19.5
Ping pong of secondary recoil(%)	/	/	0.6	0.4	0.4
Tertiary recoil effects (%)	/	/	/	20.3	21.4

Due to the high contribution of recoils, it becomes clear from this table that it is justified to use numerical techniques for the geometric efficiency for successive α-decays. The obtained energy spectra for a zero source-detector system and the used distance are shown in Figure 6.13. The peaks are not entirely shaped as the typical response due to the lack of a dead layer in the simulations. The low energy tailing is more pronounced at a zero distance, which is because the α-particles of these energies are mainly coming from backscattering. As these need to change their direction in order to escape the sample, the probability decreases as a function of the angle between the emission angle and the foil. Therefore, increasing distances will reduce the received amount of backscattered particles. Furthermore, it can be noticed that the ^{225}Ac and ^{213}Bi peaks will be indistinguishable with this setup. Finally, it can be noticed that the energy spread increases for the α-particles coming from daughter nuclei later in the decay. This is expected, as the nuclei remaining in the sample will be distributed over a larger depth range.

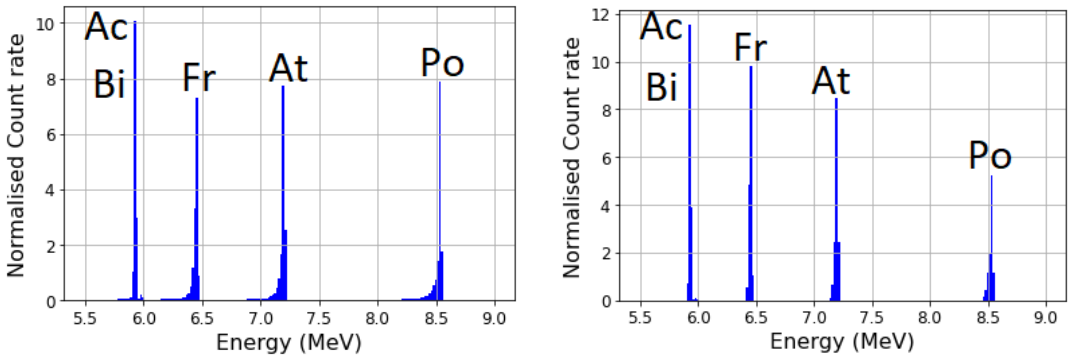

(a) (b)

Figure 6.13: Energy spectrum for a source-detector distance equal to (a) 0 mm and (b) 20.285 mm.

Perhaps the most interesting comparison between the full numerical and semi-analytical models is to compare the geometric efficiency for ^{225}Ac using the implantation profile obtained from simulations. As the difference between the circular and Gaussian model is small compared to the fluctuations on the calculated efficiency (as seen in Section 6.1.1.3), only the comparison was only made for the circular source. The geometric efficiencies are plotted in Figure 6.14 (a), while the difference between the two ($\Delta\varepsilon$) is plotted in Figure 6.14 (b).

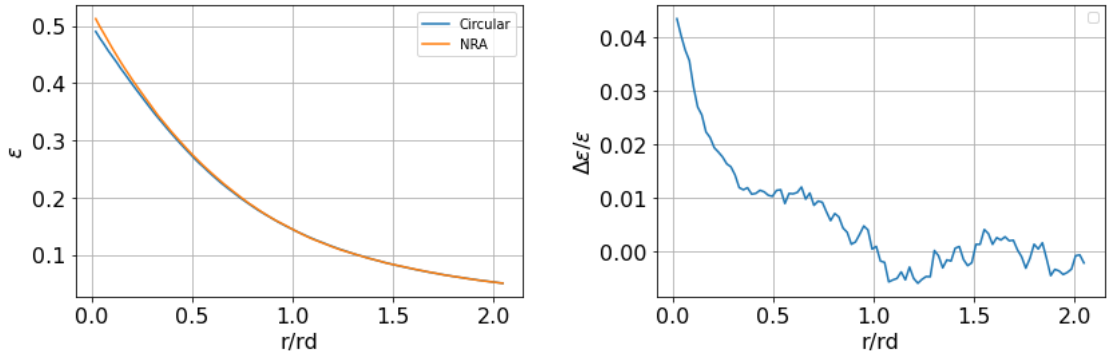

(a) (b)

Figure 6.14: Comparison of the geometric efficiency obtained by the circular semi-analytical model and the NRAM for ^{225}Ac.

As the implanted depth is relatively shallow and only direct detection contributes, the circular semi-analytical model works well. The difference between the models is roughly equal to the contribution coming from backscattering. Initially, it is responsible for about 5% (relative) of the total geometric efficiency. This reduces to less than 0.5% of the total geometric efficiency after $r = r_d$. The fluctuations on this graph are a construct of the finite number of simulated particles, and thus not of physical origin.

This model could still be improved by modeling the Si-detector itself and using the final positions of the recoil on the detector to send out particles isotropically which would completely remove the required source approximations. Potentially, it is even possible to create a dead layer in the detector by adding a second Si layer and modeling the energy lost in the active region per particle. While these are hard to perform, it is also possible to model the geometric efficiency by using the FNM in Section 6.1.3. This requires a known distance between the sample and the detector, which means the simulation of the detector would have to be performed again if a new distance is needed. Because of a combination of backscattering and daughter nuclei recoiling out of the sample, the semi-analytical model is of little use in these experiments. However, the models could in the future be used for β- and γ-decays for the region of maximal discrepancy, or even for the geometry of calibration sources. In the γ-detection experiments performed in this project, the correction compared to the point source approximation is not relevant. For the coincidence setup, the efficiency cancels, while the geometry is not known to sufficient precision to apply it in the lead castle setup.

6.1.3 Full Numerical Model

Although the numerical recoil analysis provides some nice benefits, such as distance dependence and an energy spectrum, the accuracy of the geometric efficiency of decaying isotopes later in the chain is expected to worsen. A solution to this problem is to model the entire system at once. Besides the foil and the detector, a very low-density nitrogen gas is used as the vacuum between them. Similarly to the previous model, each decay (besides ^{225}Ac) requires two simulations, namely the α-particles and the recoils. On the other hand, there is no more need for a recoil analysis. Complicated effects such as the ping-pong effect will still occur, but there is no real differentiation between different mechanisms. Furthermore, these mechanisms are now described better than before as no more approximations have to be made. A first example lies in the 0.5 acceptance probability. Backscattering will similarly reduce the acceptance rate that it increases the number of recoils ejected from the sample. Besides this, accepting a decay after a rejection becomes more likely as the particle has moved deeper into the detector. Effects in which the recoils are sent back and forth between the foil and the detector now also incorporate implantation depth which would again make a small difference.

Contrary to the previous model, no extrapolation procedure is needed to see which particles get caught on the detector. A function can be applied in the .dat file creation that checks for particles with a range inside the detector while the coordinates orthogonal to the direction of the beam are sufficiently small. A similar thing is done with the foil parameters to remove particles missing the foil. To our knowledge, SRIM does not allow objects with finite dimensions in the directions orthogonal to the beam. This will induce some systematic dependency as the number of particles moving into the detector region after missing the foil is smaller than the number of particles moving out of the detector. The trajectories of the ^{221}Fr α-particles are shown in Figure 6.15. While most of the particles are emitted from the sample, some are emitted from inside the silicon layer (detector). As SRIM does not allow vacuum-like densities for nitrogen gas, some stopping effects are present in the nitrogen. However, the particles do not change direction or stop inside the gas significantly.

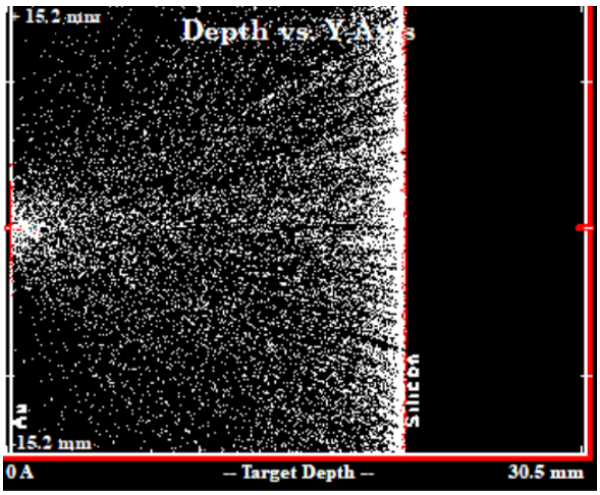

Figure 6.15: The trajectories of α-particles following the ^{221}Fr decay in the FNM. The system is modeled by a gold layer, a zinc layer, a nitrogen gas layer and a silicon (detector) layer.

After each simulation layer, the α-particles that end up in the detector are counted and divided by the total number of simulated particles to obtain the geometric efficiency for that specific decay. Using the new implantation profile, now both on the detector and the foil at the same time, the initial position for the next simulation layer is obtained. The resulting geometric efficiencies are given and compared with the numerical recoil analysis in Table 6.4. These values were used for the α-spectroscopy analysis.

Table 6.4: Comparison of geometric efficiencies obtained via the numerical models with a 20.285 *mm* source-detector distance. The fraction denotes the geometric efficiency of the FNM divided by that of the NRAM.

Isotope	Geometric efficiency(%)	$\frac{\varepsilon_{geo}^{FNM}}{\varepsilon_{geo}^{NRA}}$
^{225}Ac	4.787	0.984
^{221}Fr	4.820	0.984
^{217}At	4.963	1.171
^{213}Bi	4.591	1.398
^{213}Po	4.568	1.472

It becomes clear that the absolute geometric efficiencies, but also the ones relative to each other, changed drastically. This change mainly occurs for isotopes later in the decay chain. As the number of particles that end up in the detector should be estimated better by this model than the previous one, these values were used for the data analysis. There is a slight reduction for the ^{225}Ac and ^{221}Fr efficiency, in the order of 1.5% (relative). This is most likely caused by some form of backscattering out of the detector. Since the different models agree within 2%, it was concluded the primary decay and recoils were treated sufficiently well. Quite a bit more trouble arises for the other decays, as they increase significantly compared to the numerical recoil analysis. It was postulated that this was due to the inaccurate probability estimates from the previous model, although further research would have to be done to confirm this. This would include different probabilities for acceptance after rejection and for the ping-pong effects. As many particles were simulated, the statistical errors should be negligible compared to systematic errors. However, it is not at all straightforward to estimate those.

Certain additional improvements were thought of, but due to a lack of time, these were not simulated. By modeling the detector in itself, it is possible to keep the benefits of the full numerical treatment while also getting the energy spectrum. This detector simulation could even possess a dead layer part which would provide a low energy tailing, which is not accurately portrayed in the NRAM. By using different sublayers, SRIM provides a lot of freedom to its users. Therefore, the possible improvements to the model are numerous. There are 3 ultimate limitations that would continuously provide systematic errors. The first concept was mentioned in the limitations of the NRAM in Section 6.1.2. Simplistic aspects, such as in-flight recoil decay are expected to be very minor. Furthermore, theoretical uncertainties would affect both the branching ratios and energies. Finally, there is to our knowledge no method in SRIM to deal with the channeling of implanted particles. As later in the experiments, more particles were implanted at depths where none were expected, this could add a systematic effect. Even so, this acts on a minor part of the particles. Therefore, the relative geometric efficiencies are expected to remain similar.

6.2 Experimental Setup

The last setup that was used is the α-chamber, which is used for α-spectroscopy of the ^{225}Ac decay chain. The setup itself was designed for an earlier campaign, which investigated the production of actinium from uranium carbide targets. The setup consists of two major components, namely a vacuum chamber and a specially designed ladder system shown in Figure 6 (a) and (b) respectively. The vacuum chamber was pumped to pressures equal to 10^{-6} mbar to avoid scattering or stopping of particles. Connected to this vacuum chamber is the ladder system. Its sole purpose was to hold the foils and move them accurately in the direction parallel to the detector. For the main measurements, a digital DAQ was used. The only electronic components required for this are the DAQ, a preamplifier and a high-voltage supply to reverse bias the PIPS detector. However, when later in the project the foils returned, measurements were made using analog data acquisition. These measurements will not be discussed here, as they go beyond the scope of this thesis. Once the foil was in place, a long measurement was made and saved in time-ordered ROOT files. As the count rate from α-particles being detected is in the order of kHz throughout the measurement period, the memory required to store the data was in the order of terabytes. This data was moved onto a computing cluster awaiting its analysis.

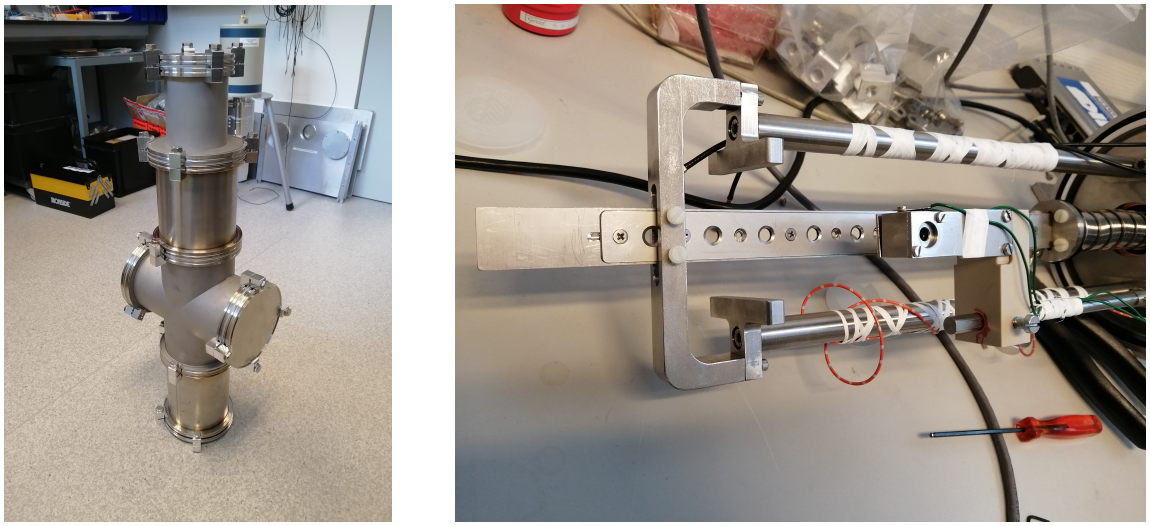

(a) (b)

Figure 6.16: (a) vacuum chamber and (b) old ladder system of the alpha setup.

As the foils for this campaign had a different shape and size than the previous one, the ladder itself had to be replaced. The design of the new ladder is shown in Figure 6.17. Since it is only fixed on the flange, teflon screws were initially used to prevent oscillation of the sample in the direction orthogonal to the detector. Unfortunately, since the ladder design was different from before, the screws moved over the openings made for holding the foils. When this happened, they could tighten themselves when the ladder was moved, causing interference with the motion. Besides just damaging the ladder and the screws themselves, this could mean that in a real measurement, the samples could be scratched, causing severe contamination risks. A system with more stable guiding blocks to keep the ladder in place was thus incorporated.

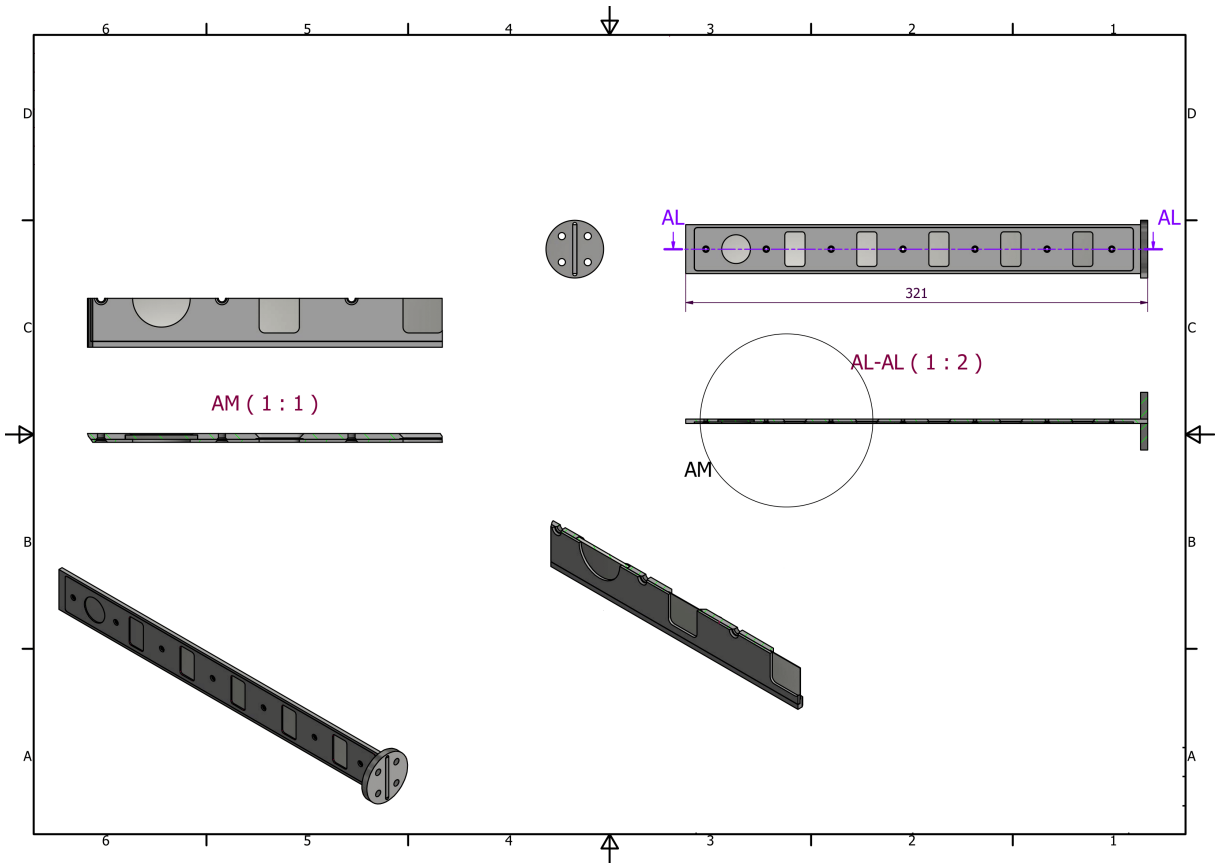

Figure 6.17: Design of ladder required to accommodate the foils received from MEDICIS.

The next step was to measure the distance between the source and the detector as accurately as possible. From the schematics of the ladder, it was known that the distance from the source position to the edge of the ladder is equal to 1 mm for the calibration source, and 1.5 mm for the foils. Besides this, the data sheets from the detector indicate that the distance from the protective ring to the surface is 1 mm [37]. By using a micrometer, the remaining distance was measured. As the main uncertainty lies in these measurements, 10 independent measurements were made (shown in Table 6.5). Before computing the mean and standard deviation, the maximal and minimal values were left out. This way, the resulting value should be less vulnerable to extreme values. The distance is then given by the mean of the remaining values, while the standard deviation provides the uncertainty. If the error on the detector and ladder dimensions is set to 0, the source-detector distance is equal to 20.29(20) mm. For future campaigns, it could be useful to mark specific distances on the part holding the detector. This would allow for a better reproducibility.

Table 6.5: Distances between the edge of the ladder and the protective ring of the detector, obtained via micrometer measurements.

Measurement	Distance (mm)
1	18.10
2	18.00
3	18.67
4	17.45
5	17.62
6	17.64
7	17.47
8	17.84
9	17.75
10	17.86

A final important remark to make about the alpha setup, is that during the measurements, the detector resolution degraded. As it has been used for several other measurements without this occurring, a physical explanation had to be found as to why this happened. A possible cause that was found lies in sputtering of the detector. Many heavy recoils come onto the detector at energies in the order of 100 keV. In this regime, sputtering is generally a significant effect [38]. To avoid this from happening in future campaigns, a thin mask could be created that stops the heavy recoiling nuclei. Using such a mask would require an additional simulation layer for geometric efficiency calculations. Sample spectra from the start and end of the measurements are shown in Figure 6.18. The decreased resolution is mainly visible by looking at the fine structure peaks. The peaks between 10 MeV and 20 MeV are due to summing, and also show this degradation well.

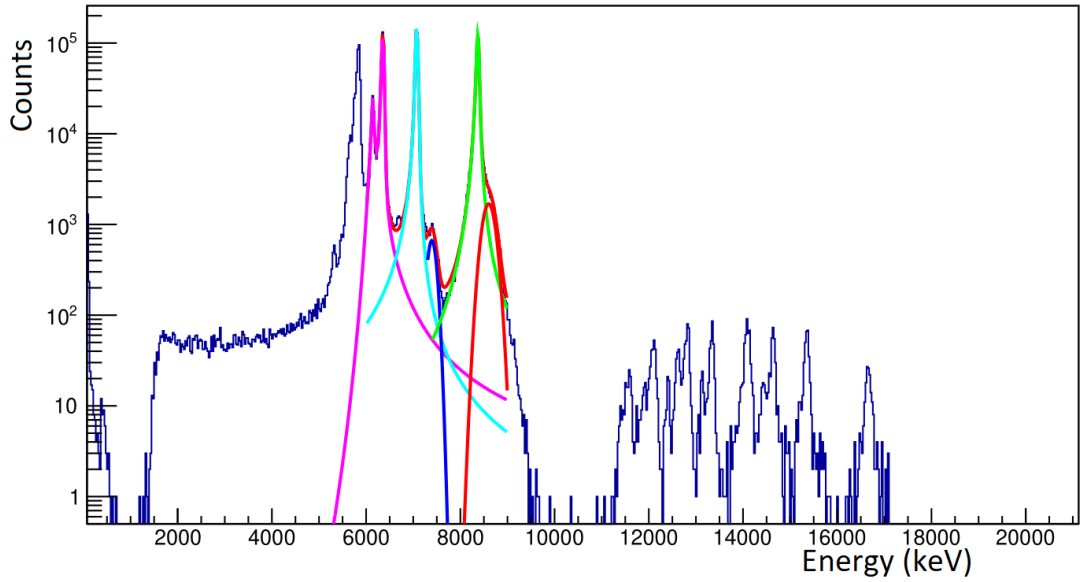

(a)

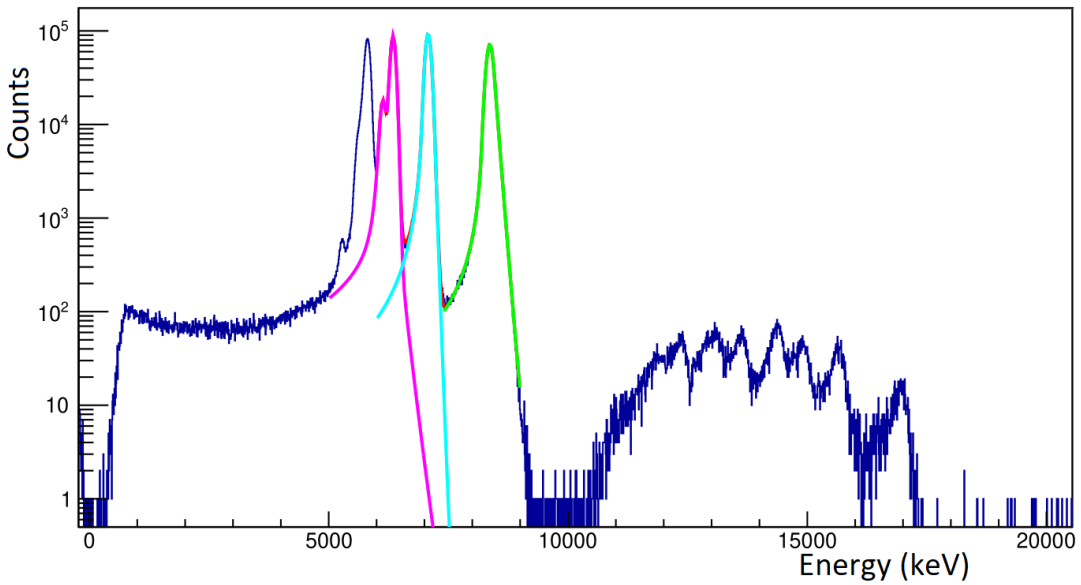

(b)

Figure 6.18: (a) Spectrum in early measurements and (b) spectrum of later measurements, showing the decreased resolution. The Pink curve is the fit for ^{221}Fr, the blue curve is the fit for ^{217}At and the green curve is the fit for ^{213}Po.

6.3 Analysis of the foil data

Due to a lack of time, the α-setup data was not analysed by me personally. Instead, the work presented here is based on the analysis performed by J.D. Johnson. The main aspects and results are treated, while the details are not. This setup relies on many of the same principles as those in Chapter 4 and Chapter 5, such as dead time and ROOT-functions. The non-paralyzable model was used to estimate the dead time, which was now relevant due to higher count rates. Furthermore, a digital data acquisition system was used to write information on the energy and timing of an α-decay event into time-ordered ROOT files. As the peaks of ^{225}Ac and ^{213}Bi overlap, only the ^{221}Fr, ^{217}At and ^{213}Po peaks were used. The only one of these with significant fine structure was ^{221}Fr, which was fitted as two peaks. In contrast to the lead castle setup, no energy response function was fitted, which had two main reasons. First of all, the efficiency response in a PIPS detector is 100% in the range of α-particle energies. Besides that, Section 6.1 clearly showed that the entire decay chain plays a role in the calculation of the geometric efficiency. Short checks confirmed that the detector had a 100% intrinsic efficiency within the uncertainty of the calibration source. Therefore the geometric efficiencies obtained in the FNM (Section 6.1.3) were used as absolute efficiency. The values are shown in Table 6.6. Here the uncertainty was assumed to be 0.10% (absolute).

Table 6.6: Total detection efficiency of α-decays coming from different isotopes.

Isotope	Geometric efficiency (%)
^{221}Fr	4.820(10)
^{217}At	4.963(10)
^{213}Po	4.568(10)

Contrary to γ-spectroscopy, as discussed earlier in this thesis, α-spectroscopy does not deal with near-Gaussian peaks. Due to the effect of the dead layer of a detector, a low energy tail is present. To fit a peak, the so-called *Crystal Ball function* is typically used, as shown in Eq. (6.7). Here A and B are given by Eq. (6.8) and Eq. (6.9) respectively. The fitting parameters are in this case N, μ, σ, α and n.

$$f(x; N, \mu, \sigma, \alpha, n) = \begin{cases} N e^{-\left(\frac{x-\mu}{2\sigma}\right)^2}, & \text{for } \frac{x-\mu}{\sigma} > -\alpha \\ NA(B - \frac{x-\mu}{\sigma})^{-n}, & \text{for } \frac{x-\mu}{\sigma} \leq -\alpha \end{cases} \tag{6.7}$$

$$A(n, \alpha) = \left(\frac{n}{|\alpha|}\right)^n e^{-\frac{1}{2}|\alpha|^2} \tag{6.8}$$

$$B(n, \alpha) = \frac{n}{|\alpha|} - |\alpha| \tag{6.9}$$

Assuming a positive value of α, the first part of the fit function represents the high energy behavior. In this case, the fitting is identical to a Gaussian. That is, N represents the amplitude, μ represents the peak position and σ represents the standard deviation. Once the energy is α standard deviations below the peak centroid, the the function describes the tailing effect. Finally, n determines the magnitude of the tail. A graphic representation of the effect of n on the fitting function is shown in Figure 6.19. It is clear that smaller values of n correspond to a longer tail. As n goes to zero, the fitting function f will go to N in the tail range.

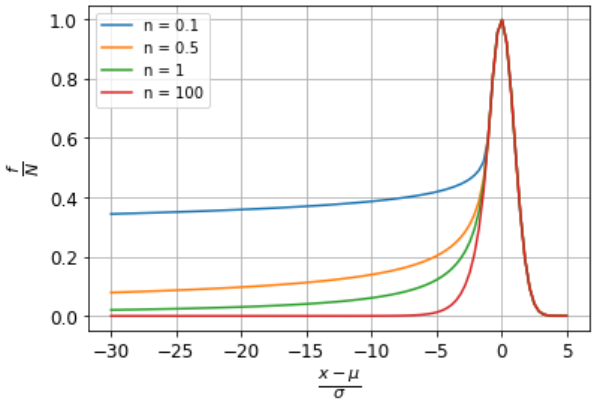

Figure 6.19: Behavior of the Crystal Ball function for changing values of n, using $\alpha = 1$.

As the particles undergo different energy losses inside the sample, there is also a high energy tail present. This tail was accounted for by modifying the Crystal Ball function such that it has both a low- and high energy tail. The new fitting function is given by Eq. (6.10). Here A_L, A_U, B_L and B_U are given by Eq. (6.8) and Eq. (6.9) respectively with the indices of α and n matching that of A and B.

$$f(x; N, \mu, \sigma, \alpha_L, n_L, \alpha_U, n_U) = \begin{cases} Ne^{-\left(\frac{x-\mu}{2\sigma}\right)^2}, & \text{for } -\alpha_L < \frac{x-\mu}{\sigma} < \alpha_U \\ NA_L(B_L - \frac{x-\mu}{\sigma})^{-n_L}, & \text{for } \frac{x-\mu}{\sigma} \leq -\alpha_L \\ NA_U(B_U + \frac{x-\mu}{\sigma})^{-n_U}, & \text{for } \frac{x-\mu}{\sigma} \geq \alpha_U \end{cases} \tag{6.10}$$

Using this fitting function provides 7 fitting parameters for each peak. As 4 peaks were fitted, a total of 28 fitting parameters were used. Sample spectra of the measurements are shown in Figure 6.18. The pink, blue and green fits are for ^{221}Fr, ^{217}At and ^{213}Po respectively. The peaks with an energy slightly lower than the ^{221}Fr are from ^{225}Ac and ^{213}Bi, while the peaks at energies between 10 and 20 MeV are caused by summing effects. The latter are insignificant compared to the counts in the actual peaks.

6.4 Experimental results

6.4.1 Dead time and spectral resolution correction

For this experiment, two correction factors were used. The first of these is the dead time, which again uses the decaying source method for the determination of the dead time and the non-paralyzable model for the correction factors. In comparison with the lead castle setup, there are many more data points that can be used for the fitting. Besides this, the count rate in the detector of the M108 and M120 samples was sufficiently high for dead time to influence the count rates significantly ($t_{dead} \sim \frac{1}{countrate}$). The fits for the decaying source method are shown in Figure 6.20.

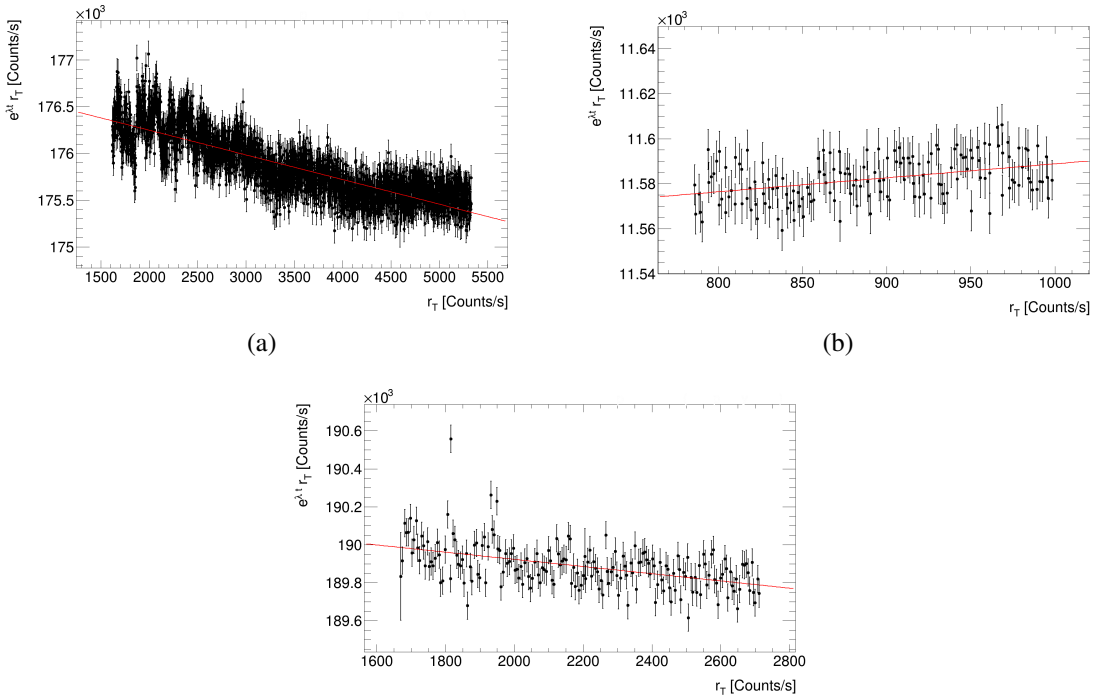

Figure 6.20: Linear fits for estimating the dead time using the decaying source method for (a) M108, (b) M118 and (c) M120.

The resulting dead time for M118 is $-5.4(1)\,\mu s$, but this is negative due to the near-constant value of the function, and not physical. Therefore the dead time was set equal to 0. M108 and M118 obtained a dead time of 1.49(2) μs and $1.0(1)\,\mu s$ respectively. In contrast to the lead castle setup, the dead time is positive within several standard deviations.

Furthermore, as the bin integral was taken within a domain around the peak centroids, a correction was made to extrapolate what the total integral would be. This is called the spectral resolution correction. It is performed by taking the fraction of the bin integral in a small range and the integral of the fitting function in a larger range. The correction factor ξ is given by Eq. (6.11). Here f is the resulting fitting function, $[E_-, E_+]$ is the broad domain and $[E_-^*, E_+^*]$ is the narrow domain.

$$\xi = \frac{\int_{E_-}^{E_+} f(E)dE}{\int_{E_-^*}^{E_+^*} f(E)dE} \tag{6.11}$$

This was performed for a number of sample spectra, for which the reliability of the fit was checked. Afterwards, a linear fit was performed for the correction factor of each peak as a function of time. The obtained fits are shown in Figure 6.21 for the M120 measurements.

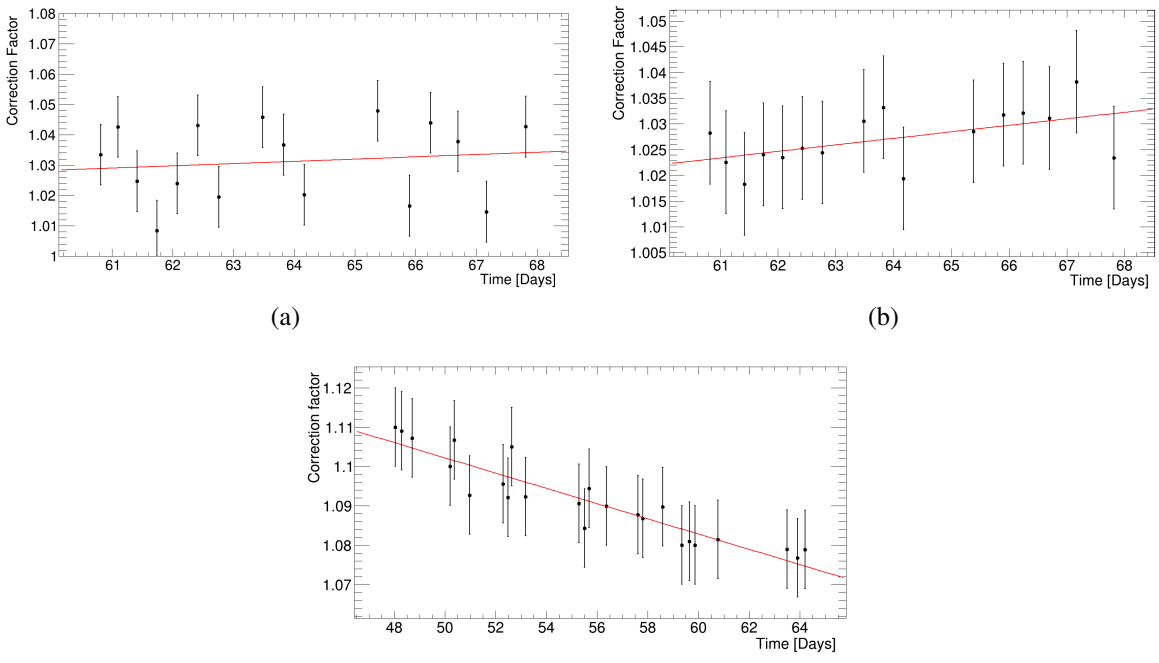

Figure 6.21: Linear fits on the spectral resolution correction of M120 as a function of time for (a) ^{221}Fr, (b) ^{217}At and (c) ^{213}Po.

The correction factors are at least in the order of a percent at any given time, which implies they are important to take into account. Furthermore, these are not the same for the different isotopes. Thus, without this correction, a systematic effect of almost 10% could remain between the activities obtained from the different peaks.

6.4.2 Obtaining the EOC activity

By applying the corrections, the activities at a number of times can be obtained. Using exponential fitting with a fixed half-life, the fits in Figure 6.22 are obtained.

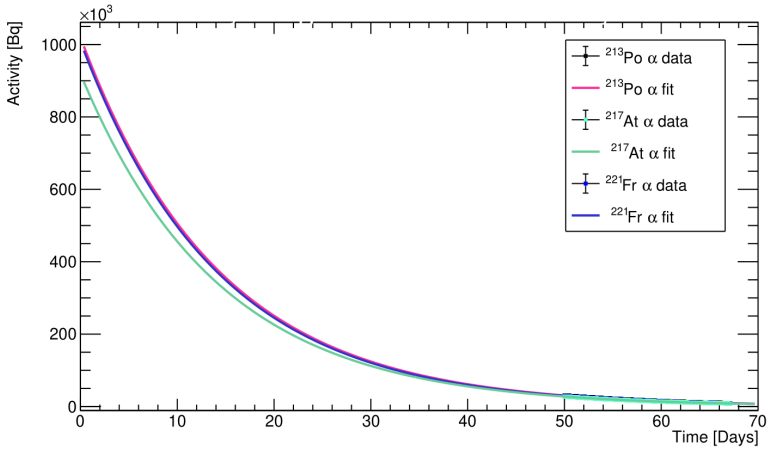

(a)

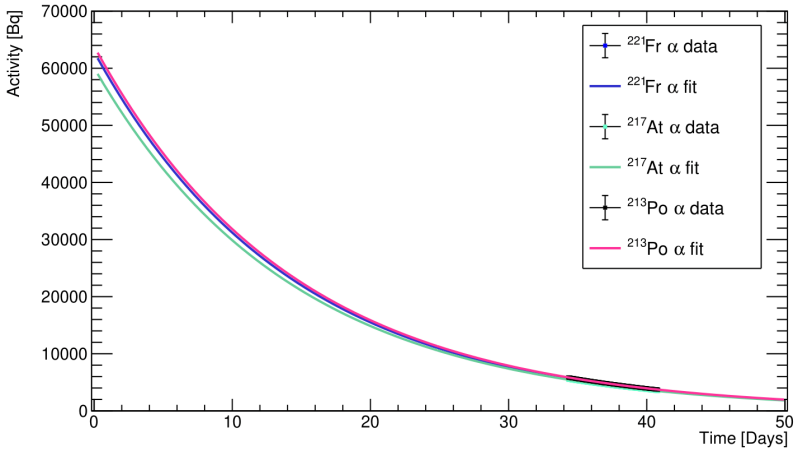

(b)

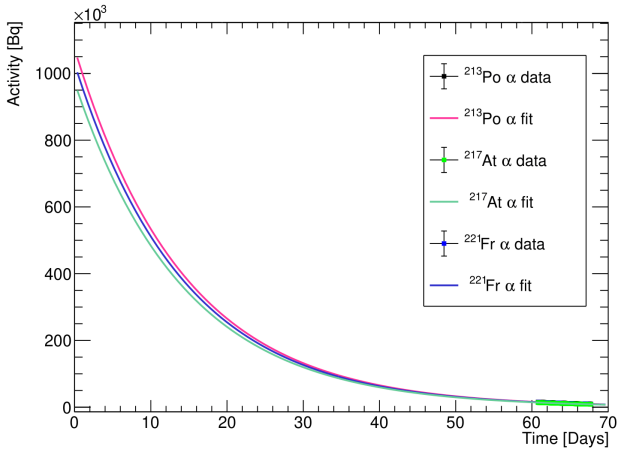

(c)

Figure 6.22: Exponential decay fit for the α-spectroscopy data for (a) M108, (b) M118 and (c) M120.

There is some systematic effect between the activities obtained from the different α-decays. This could partially be caused by the uncertainties of literature values, but could also be caused by systematic effects on the geometric efficiency. The latter is most likely due to inaccurate placement of the detector or the source. The EOC activities for the different samples and the different peaks are provided in Table 6.7. Here the mean activity was calculated similarly as in Chapter 4.

Foil	^{221}Fr (kBq)	^{217}At (kBq)	^{213}Po (kBq)	Mean activity (kBq)
M108	994(24)	1002(30)	920(25)	974(26)
M118	62.8(14)	60.1(13)	63.9(15)	62.1(8)
M120	998(21)	1009(21)	1030(22)	1001(21)

Table 6.7: Activities obtained from the exponential fitting of the α-spectroscopy data.

7 Comparing the different setups

The obtained EOC activities are shown in Table 7.1 for the setups at IKS. All three agree within a single standard deviation for the M108 sample. For M118, the situation is slightly worse, but the values obtained from the lead castle and the α-chamber are still in agreement within 3 standard deviations. Finally, the M120 sample shows some discrepancy, which is potentially related to the degrading of the resolution of the detector for the α-chamber. Another thing that can be noticed, is that the activities from the lead castle are slightly higher than those obtained from the α-chamber. This is likely caused by the uncertainty on the literature intensity and/or due to systematic errors in the efficiency response. Consequently, the α-spectroscopy results of M120 were not used in the mean activity calculation. The overlapping of the probability distributions is shown in Figure 7.1.

Table 7.1: EOC activity (in kBq) for all setups obtained by exponential fitting with a fixed half-life.

Foil	Lead castle	Coincidence	α-chamber	Mean activity
M108	1009(34)	993(54)	974(26)	988(20)
M118	68.2(23)	/	62.1(8)	62.8(8)
M120	/	839(45)	1009(21)	839(45)

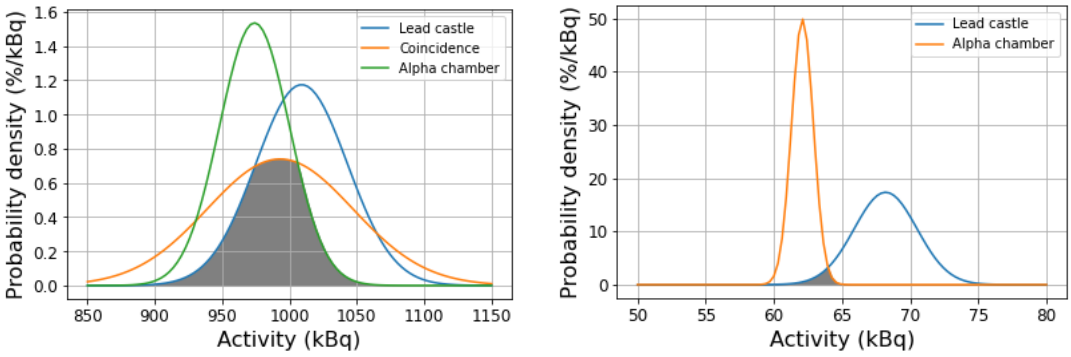

(a)

(b)

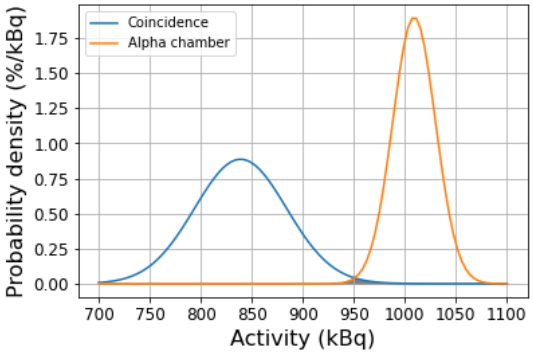

(c)

Figure 7.1: Overlapping fraction of the activity obtained from the different setups for (a) M108, (b) M118 and (c) M120.

The collections started with 10.6 MBq and 9.33 MBq. Using these values, the collection efficiencies were calculated. The resulting values are shown in Table 7.2. It can be concluded that the total collection efficiencies are 9.77(19)% and 8.99(48)% for run 1 and 2 respectively.

Table 7.2: Collection efficiencies (in %) for both runs of MED-024.

Run	Foil	Lead castle	Coincidence	α-chamber	Mean
1	M108	9.52(32)	9.37(51)	9.19(19)	9.31(18)
1	M118	0.643(22)	/	0.586(8)	0.592(7)
2	M120	/	8.99(48)	10.81(23)	8.99(48)

As mass scans were performed during the collection and the setup was not optimized from the start, these values provide a lower bound on the maximal obtainable collection efficiency by using this process. The collection efficiency consists of a transport efficiency and an ionization efficiency. The latter of these will provide an upper limit to the collection efficiency of future collections at CERN-MEDICIS.

8 Conclusion

The purpose of this research was to examine the collection efficiency of ^{225}Ac following mass separation and laser ionization at CERN-MEDICIS. The zinc-coated gold foils, on which the ^{225}Ac was implanted, were sent to IKS for further analysis. The activity was measured using three setups, which focused on different parts of the decay chain. The first setup examined the strong γ-lines in the spectrum. The photons that were used for this originated from the relaxation after the ^{221}Fr and ^{213}Bi decays. While this method requires relatively few data points and can be used for low activities, the uncertainty on the efficiency response function is currently a limiting factor on the precision.

The second setup utilizes photons that are emitted in near coincidence. These can be used to perform efficiency-free activity measurements with γ-γ coincidence measurements. Two significant sets of coincidences are present in the decay chain, which are after the β-decay of ^{213}Bi and after the β-decay of ^{209}Tl. The advantage of this technique is that the uncertainty on the efficiency response does not play a role, which removes most of the systematic errors. On the other hand, the setup also has two major downsides. Firstly, the mulitpolarity of the transitions from ^{213}Bi is not complete in literature, which implies angular correlation due to mixing of transition types could shift the activity in a systematic fashion. Furthermore, the low intensity of the coincidences implies that relatively high activity sources should be used for good statistics. The current limits to the uncertainty are limited by literature values of the branchings and intensities.

The final setup measured α-particles in the decay chain of ^{225}Ac. As the ^{225}Ac and ^{213}Bi peaks overlap, only the ^{221}Fr, ^{217}At and ^{213}Po peaks were used. While the intrinsic efficiency is approximately 100% and the literature intensities are known quite accurately, the geometric efficiency had to be modelled separately. For this three sets of models were developed, namely the semi-analytical model, the numerical recoil analysis model and the full numerical model. The last of these was judged to be the most appropriate, and was thus used for the analysis.

The individual setups generally agreed quite well. However, a clear discrepancy is present for the M120 activity measurements. In this case, the reliability of the obtained activity for the α-chamber could not be guaranteed due to the degrading of the detector resolution. As the activity at the start of collection is known, the obtained activities could subsequently be used to investigate the collection efficiency. As mass scans and laser optimization were performed during the collection, it is possible to determine the amount of lost activity by using the ion current measurements. While the first run used a rhenium foil with dried nitrate solution of ^{225}Ac, the second dried this nitrate solution on a felt of thorium-oxide grains. The obtained total collection efficiencies were equal to about 9.77(19)% and 8.99(48)% for the first and second run respectively. The latter of these required a significantly higher temperature. Furthermore, the second collection was ended before saturation was reached, implying the maximal achievable value would be higher. Therefore the effusion efficiency is most likely negligible compared to the ionization efficiency.

A Mean time of an exponential

When a measurement is performed on an exponential decaying function, the time for the data point for the time is not simply the median time, but instead the mean time. The median time is given by $\frac{t_0+t_1}{2}$, where t_0 in the starting time of the measurement and t_1 is the end time of the measurement. The mean time has to be calculated via the mean value theorem for integrals. The derivation is shown below. For this project, the decay constant is that of ^{225}Ac.

$$
\begin{aligned}
(t_1-t_0)e^{-\lambda t_m} &= \int_{t_0}^{t_1} e^{-\lambda t}dt \\
\implies (t_1-t_0)e^{-\lambda t_m} &= -\frac{1}{\lambda}\left[e^{-\lambda t_0}-e^{-\lambda t_1}\right] \\
\implies -\lambda t_m &= \ln\left(\frac{1}{\lambda(t_1-t_0)}\right)+\ln\left(e^{-\lambda t_0}-e^{-\lambda t_1}\right) \\
\implies -\lambda t_m &= -\ln[\lambda\Delta t]+\ln\left[e^{-\lambda t_1}\left(e^{-\lambda t_0}e^{\lambda t_1}-1\right)\right] \\
\implies \lambda t_m &= \ln[\lambda\Delta t]-\left[-\lambda t_1+\ln\left(e^{\lambda\Delta t}-1\right)\right] \\
\implies t_m &= t_1+\frac{1}{\lambda}\ln(\lambda\Delta t)-\frac{1}{\lambda}\ln\left(e^{\lambda\Delta t}-1\right)
\end{aligned}
$$

$$
\implies t_m-t_0 = \Delta t+\frac{1}{\lambda}\ln(\lambda\Delta t)-\frac{1}{\lambda}\ln\left(e^{\lambda\Delta t}-1\right)
$$

B Vial geometry

This appendix covers the correction factor for the vial geometry in the lead castle setup. The goal is to write the height of the center of the foil as a function of the diameter of the vial, the length of the foil, the width of the foil and the thickness of the vial bottom. A top view of the vial is given in Figure B.1. Here l and w are the length and width of the foil respectively and d is the diameter of the vial.

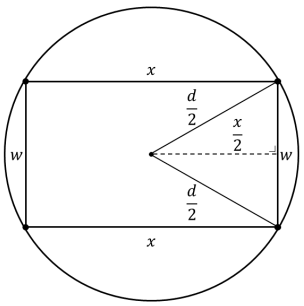

Figure B.1: Top view geometry of the vial

For the top view, the foil is a rectangular shape inside a circle. Using simple trigonometry, it can be seen that

$$\left(\frac{x}{2}\right)^2 = \left(\frac{d}{2}\right)^2 - \left(\frac{w}{2}\right)^2$$
$$\implies x^2 = d^2 - w^2$$

The height of the center of the foil corresponds to half of the height of the top part of the sample. In turn, this can be calculated with Pythagoras theorem on the triangle with the height of the foil and x as sides, and the length of the foil the hypotenuse. Therefore,

$$(2h)^2 = l^2 - x^2$$
$$\implies h = \frac{1}{2}\sqrt{l^2 + w^2 - d^2}$$

Adding the thickness of the vial bottom t, to this height provides the additional *effective distance* h'.

$$h' = t + \frac{1}{2}\sqrt{l^2 + w^2 - d^2}$$

C Dead time in efficiency-free activity measurements

To show that the dead time cancels in efficiency-free activity measurements, it is convenient to define the *live time* t_{live}. This is the part of the total measurement time t, that does not experience any dead time. The live time of a specific detector i, is given by Eq. (C.1). Here d_i is the dead time fraction.

$$t_{live,i} = t(1 - d_i) \tag{C.1}$$

The two-detector dead time fraction consists of three parts, namely detector 1 experiences dead time and detector 2 doesn't, detector 2 experiences dead time and detector 1 doesn't, and both detectors experience dead time. Therefore the coincidence dead time fraction is given by Eq. (C.2).

$$\begin{aligned} d_{coinc} &= d_1(1-d_2) + d_2(1-d_1) + d_1 d_2 \\ &= d_1 + d_2 - d_1 d_2 \end{aligned} \tag{C.2}$$

This implies that the live time for the coincidence events $t_{live,c}$, is equal to Eq. (C.3).

$$\begin{aligned} t_{live,c} &= 1 + d_1 d_2 - d_1 - d_2 \\ &= (1-d_1)(1-d_2) \end{aligned} \tag{C.3}$$

The effect on the activity measurements will be given by a fraction of live times, as given in Eq. (C.4).

$$\frac{t_{live,c}}{t_{live,1}\, t_{live,2}} = \frac{(1-d_1)(1-d_2)}{(1-d_1)(1-d_2)} \tag{C.4}$$

$$= 1 \tag{C.5}$$

Therefore, dead time cancels out and does not effect the coincidence setup measurements.

D Geometric efficiency calculations

To obtain reliable and precise results, one of the most important things to take into account is the geometric efficiency. This is the ratio of the solid angle covered by the detector to the solid angle of the sphere over which the source is assumed to isotropically emit radiation. In our case the detector had a circular surface. For the source three different models were used, as mentioned in the text.

The point source approximation can be done relatively quickly as it can use the spherical symmetry of the problem to its fullest, providing us with Eq. (D.1) referring to the geometry shown in Figure D.1. Finally Eq. (D.2) is obtained by inserting θ_{max} that is calculated using simple trigonometry.

$$\varepsilon_{geo} = \frac{1}{4\pi}\int_0^{2\pi} d\phi \int_0^{\theta_{max}} \sin\theta d\theta \tag{D.1}$$

$$= -\frac{1}{2}\left[\cos\theta\right]_0^{\theta_{max}}$$

$$= \frac{1}{2}\left[1-\cos\theta_{max}\right]$$

$$= \frac{1}{2}\left(1-\frac{z}{\sqrt{R^2+z^2}}\right) \tag{D.2}$$

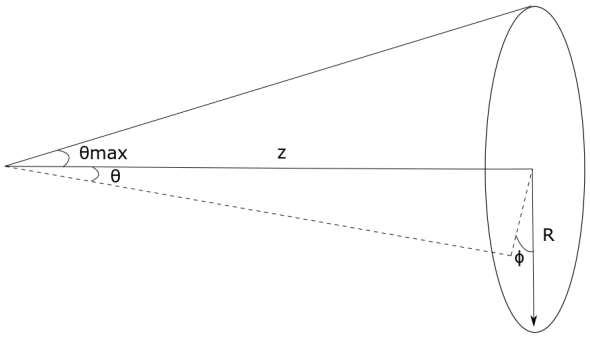

Figure D.1: Geometry of the point source case.

Using polar coordinates and some tricks such as the Fourier-Bessel integral and properties involving Bessel functions, it was shown in [39] that the geometric efficiency for a circular flat source is given by Eq. (D.3). Where R_D and R_S are the detector and source radius respectively, z is the distance between the center of the source and the center of the detector and J_1 denotes the first Bessel function of the first kind. This integral is not analytically solvable, thus we either have to approximate it or use numerical methods. The numerical methods used in this project are based on Riemann sums in combination with importance sampling, sometimes referred to as umbrella sampling. These are explained thoroughly in [35] and [40].

$$\varepsilon_{geo} = \frac{R_D}{R_S}\int_0^{\infty} \frac{e^{-kz}}{k} J_1(kR_S)\,J_1(kR_D)\,dk \tag{D.3}$$

However, the source will actually have a Gaussian surface distribution rather than a circular one. Therefore, a relation was obtained by using some normalized density distribution in polar coordinates (with angular symmetry), which in theory can be any normalized function of r. The normalization of the polar Gaussian is shown in Eq. (D.4), but it can also be obtained by multiplying 2 normalized Cartesian Gaussian functions. Eventually the Gaussian surface distribution can be inserted and the efficiency is obtained. The geometry was taken near identical to the one in Figure D.2 with the only difference being the source to be replaced to a 2-d Gaussian in r.

$$
\begin{aligned}
\rho(r) &= Ae^{-\frac{r^2}{2\sigma^2}} \\
\implies 1 &= \int_0^{2\pi} d\phi \int_0^{\infty} rdrAe^{-\frac{r^2}{2\sigma^2}} \\
&= 2\pi A\sigma^2 \\
\implies A &= \frac{1}{2\pi\sigma^2} \qquad \text{(D.4)}
\end{aligned}
$$

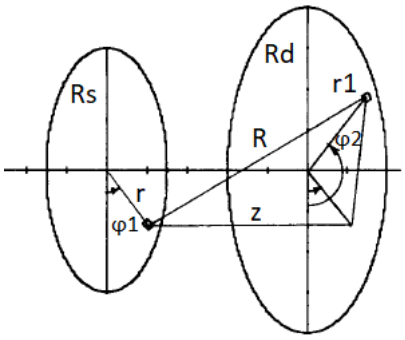

Figure D.2: Geometry for a flat disk detector source system. Adapted from [39]

Here follows a derivation along the lines of that from [39] and using similar methods such as using the Fourier-Bessel integral and rewriting as a derivative. This obtains a general form with a normalized density in Eq. (D.5) and for specifically the Gaussian distribution in Eq. (D.6). In practise the final integral over r often does not run to infinity because of the use of collimators in the implantation process. However it is possible to put this effect into the density distribution later works.

$$
\begin{aligned}
\varepsilon_{geo} &= \int_{\Omega_1}\int_{\Omega_2} \rho(r)\, dS_1 \frac{dS_2}{4\pi R^2}\frac{\vec{n}\cdot\vec{R}}{R} \\
&= \frac{1}{4\pi}\int_{\Omega_1}\int_{\Omega_2} dS_1\, dS_2 \frac{z}{R^3}\rho(r) \\
&= -\frac{1}{4\pi}\int_0^{2\pi} d\phi_1 \int_0^{2\pi} d\phi_2 \int_0^{\infty} r\,dr \int_0^{R_d} r_1\, dr_1 \frac{\partial\left(\frac{1}{R}\right)}{\partial z}\rho(r) \\
&= \pi\int_0^{\infty} r\,dr \int_0^{R_d} r_1\, dr_1 \left[\int_0^{\infty} J_0(kr)\, J_0(kr_1)\, e^{-kz} dk\right] \\
&= \pi R_d \int_0^{\infty} dk J_1(kR_d)\, e^{-kz} \int_0^{\infty} r\,dr\,\rho(r) J_0(kr) \qquad \text{(D.5)} \\
&= \frac{R_d}{2\sigma^2}\int_0^{\infty} dk \int_0^{\infty} dr\, r J_0(kr) J_1(kR_d)\, e^{-kz} e^{-\frac{r^2}{2\sigma^2}} \qquad \text{(D.6)}
\end{aligned}
$$

It is obvious that for large values of z, the efficiency should converge to that of the point source approximation. However, since a Gaussian (at least in theory) has an infinite range, the value in limit to 0 will be less than 0.5. This is in contrast to the circular uniform surface distribution in the case of a source radius smaller than the detector radius. It is possible to determine what the efficiency should be in the limit of z to 0. Since isotropic emission is assumed, only a maximum of 0.5 efficiency can be obtained. In the limit of z to 0, all particles emitted from a point in the source with a distance from the center of the source less than the radius of the detector will come into the detector. This results in the integral in Eq. (D.7). For which it is easy to show that the result is given by Eq. (D.8).

$$\varepsilon_{geo}(z=0) = \frac{1}{2}\int_0^{2\pi} d\phi \int_0^{R_d} r\,dr\,\frac{1}{2\pi\sigma^2}\,e^{-\frac{r^2}{2\sigma^2}} \tag{D.7}$$

$$= \frac{1}{2}(1 - e^{-\frac{R_d^2}{2\sigma^2}}) \tag{D.8}$$

E Isotropic distribution

The generation of a spherical isotropic distribution is crucial when assigning initial directions for α-particles in an α-decay. The first thing that has to be done, is to find the distribution for the spherical angles θ and ϕ. This is shown in Eq. (E.1).

$$\begin{aligned} f(\vec{r})dA &= \frac{dA}{4\pi} = f(\theta,\phi)d\theta d\phi \\ \implies f(\theta,\phi) &= \frac{\sin\theta}{4\pi} \end{aligned} \tag{E.1}$$

To get the distribution for each individual components, this has to be integrated between the boundaries of the other components. As expected this means ϕ is a uniform random number in the interval $[0; 2\pi]$ while the distribution for θ is then given by $f(\theta) = \frac{\sin\theta}{2}$. Following this, the cumulative distribution function, also known as the quantile function, is calculated using its definition in Eq. (E.2).

$$\begin{aligned} F(\theta) &= \int_0^{\theta} f(\theta)d\theta \\ &= \int_0^{\theta} \frac{\sin\theta}{2} d\theta \\ &= \frac{1}{2}[-\cos\theta]_0^{\theta} \\ &= \frac{1}{2}(1 - \cos\theta) \end{aligned} \tag{E.2}$$

Letting u be the probability to find an azimuthal angle that is equal or smaller than θ, the inverse cumulative distribution function is given in Eq. (E.3).

$$F^{-1}(u) = \arccos(1 - 2u) \tag{E.3}$$

Thus the desired distribution can be made by using the inverse cumulative distribution function method, also referred to as the inversion method. A detailed explanation of this process is provided in [41]. It is possible to obtain the isotropic distribution for θ by picking a random number uniform between 0 and 1 for u.

References

[1] Andrew KH Robertson, Caterina F Ramogida, Paul Schaffer, and Valery Radchenko. Development of ^{225}Ac radiopharmaceuticals: TRIUMF perspectives and experiences. *Current radiopharmaceuticals*, 11(3):156–172, 2018.

[2] Mike Sathekge, Frank Bruchertseifer, Otto Knoesen, Florette Reyneke, Ismaheel Lawal, Thabo Lengana, Cindy Davis, Johncy Mahapane, Ceceila Corbett, Mariza Vorster, et al. 225 Ac-PSMA-617 in chemotherapy-naive patients with advanced prostate cancer: a pilot study. *European journal of nuclear medicine and molecular imaging*, 46(1):129–138, 2019.

[3] Clemens Kratochwil, Frank Bruchertseifer, Hendrik Rathke, Markus Hohenfellner, Frederik L Giesel, Uwe Haberkorn, and Alfred Morgenstern. Targeted α-therapy of metastatic castration-resistant prostate cancer with ^{225}Ac-PSMA-617: swimmer-plot analysis suggests efficacy regarding duration of tumor control. *Journal of Nuclear Medicine*, 59(5):795–802, 2018.

[4] RA Kuznetsov, PS Butkalyuk, VA Tarasov, A Yu Baranov, IL Butkalyuk, EG Romanov, VN Kupriyanov, and EV Kazakova. Yields of activation products in ^{226}Ra irradiation in the high-flux SM reactor. *Radiochemistry*, 54(4):383–387, 2012.

[5] Hannah Ritchie and Max Roser. Energy. *Our World in Data*, 2020.

[6] P-H Rebut et al. ITER: the first experimental fusion reactor. *Fusion engineering and design*, 30(1-2):85–118, 1995.

[7] Elizabeth Gibney. Fuel for world's largest fusion reactor ITER is set for test run. *Nature*, 591(7848):15–16, 2021.

[8] Barry J Allen. A comparative evaluation of ^{225}Ac vs ^{213}Bi as therapeutic radioisotopes for targeted alpha therapy for cancer. *Australasian physical & engineering sciences in medicine*, 40(2):369–376, 2017.

[9] Michael R McDevitt, Dangshe Ma, Jim Simon, R Keith Frank, and David A Scheinberg. Design and synthesis of ^{225}Ac radioimmunopharmaceuticals. *Applied Radiation and Isotopes*, 57(6):841–847, 2002.

[10] Kim A Deal, Ila A Davis, Saed Mirzadeh, Stephen J Kennel, and Martin W Brechbiel. Improved in vivo stability of ^{225}Ac macrocyclic complexes. *Journal of medicinal chemistry*, 42(15):2988–2992, 1999.

[11] Phillip Koo. ^{223}Ra the only approved Targeted Alpha Therapy (TAT) in mCRPC-outcomes, opportunities and lessons learned. *EVERYDAY*, page 22.

[12] Dirk NJ Wyndaele. ^{223}Ra voor gemetastaseerd castratieresistent prostaatcarcinoom: stand van zaken en toekomstperspectief. *Tijdschrift voor Urologie*, 10(6):131–140, 2020.

[13] Liam Paul Gaffney, Peter A Butler, Marcus Scheck, Adam B Hayes, Frederik Wenander, Michael Albers, Beyhan Bastin, Christopher Bauer, Andrey Blazhev, Sabine Bönig,

et al. Studies of pear-shaped nuclei using accelerated radioactive beams. *Nature*, 497(7448):199–204, 2013.

[14] E Verstraelen, A Teigelhöfer, Wouter Ryssens, F Ames, A Barzakh, Michaël Bender, Raphael Ferrer, Stéphane Goriely, P-H Heenen, Mark Huyse, et al. Search for octupole-deformed actinium isotopes using resonance ionization spectroscopy. *Physical Review C*, 100(4):044321, 2019.

[15] C Apostolidis, R Molinet, G Rasmussen, and A Morgenstern. Production of ^{225}Ac from ^{229}Th for targeted α therapy. *Analytical chemistry*, 77(19):6288–6291, 2005.

[16] M. Heines. Code for master thesis. `https://github.com/MichaelHeines/Thesis`.

[17] Ricardo Manuel dos Santos Augusto, Leo Buehler, Zoe Lawson, Stefano Marzari, Monika Stachura, Thierry Stora, CERN-MEDICIS collaboration, et al. CERN-MEDICIS (medical isotopes collected from ISOLDE): a new facility. *Applied Sciences*, 4(2):265–281, 2014.

[18] VM Gadelshin, V Barozier, TE Cocolios, VN Fedosseev, R Formento-Cavaier, F Haddad, B Marsh, S Marzari, S Rothe, T Stora, et al. MELISSA: Laser ion source setup at CERN-MEDICIS facility. blueprint. *Nuclear Instruments and Methods in Physics Research Section B: Beam Interactions with Materials and Atoms*, 463:460–463, 2020.

[19] Pierre De Marcillac, Noël Coron, Gérard Dambier, Jacques Leblanc, and Jean-Pierre Moalic. Experimental detection of α-particles from the radioactive decay of natural bismuth. *Nature*, 422(6934):876–878, 2003.

[20] MS Basunia. Nuclear data sheets for A= 213. *Nuclear Data Sheets*, 108(3):633–680, 2007.

[21] J Chen and FG Kondev. Full evaluation for ^{209}Pb. *Nuclear Data Sheets*, 126:373, 2015.

[22] Ashok Kumar Jain, Sukhjeet Singh, Suresh Kumar, and Jagdish K Tuli. Nuclear data sheets for A= 221. *Nuclear Data Sheets*, 108(4):883–922, 2007.

[23] YA Akovali. Nuclear data sheets for a= 217. *Nuclear Data Sheets*, 100(1):141–178, 2003.

[24] J J.Chen and FG Kondev. Nuclear data sheets for a= 209. *Nuclear Data Sheets*, 126(1):373–546, 2015.

[25] Harry Bateman. The solution of a system of differential equations occurring in the theory of radio-active transformations. *Proc. Cambridge Phil. Soc., 1908*, 15:423–427, 1908.

[26] M Martini. HPGe schematics. `https://www.ortec-online.com/products/radiation-detectors`. Last checked on 18 april 2020.

[27] PhysicsOpenLab. PMT pulse processing. `http://physicsopenlab.org/2016/04/21/pmt-pulse-processing/`. last checked on 17 December 2020.

[28] Hesham MH Zakaly, Mohamed A Uosif, Shams Issa, Mujahed Saif, Mahmoud Tammam, and Atef El-Taher. Estimate the absolute efficiency by MATLAB for the NaI (Tl) detector using IAEA-314. In *AIP Conference Proceedings*, volume 2174, 1, page 020248. AIP Publishing LLC, 2019.

[29] Karsten Kossert, Marcell Péter Takács, and Ole Nähle. Determination of the activity of ^{225}Ac and of the half-lives of ^{213}Po and ^{225}Ac. *Applied Radiation and Isotopes*, 156:109020, 2020.

[30] Glenn F Knoll. *Radiation detection and measurement*. John Wiley & Sons, 2010.

[31] Canberra. A practical guide to high count rate germanium gamma spectroscopy. `https://www.uio.no/studier/emner/matnat/fys/nedlagte-emner/FYS4510/h05/High_count_rate_systems.pdf`, 2002. last checked on 13 May 2021.

[32] Caen. N6724 4 channel 14 bit 100 ms/s digitizer. `https://www.caen.it/products/n6724/`. Last checked of 17 May 2021.

[33] Jiancheng Yang, Gregory J Koller, Chaker Fares, F Ren, SJ Pearton, Jinho Bae, Jihyun Kim, and David J Smith. ^{60}Co gamma ray damage in homoepitaxial $\beta - Ga_2O_3$ schottky rectifiers. *ECS Journal of Solid State Science and Technology*, 8(7):Q3041, 2019.

[34] James F Ziegler, Matthias D Ziegler, and Jochen P Biersack. SRIM–the stopping and range of ions in matter. *Nuclear Instruments and Methods in Physics Research Section B: Beam Interactions with Materials and Atoms*, 268(11-12):1818–1823, 2010.

[35] S Yakowitz, JE Krimmel, and F Szidarovszky. Weighted monte carlo integration. *SIAM Journal on Numerical Analysis*, 15(6):1289–1300, 1978.

[36] Márius Pavlovič and Ivan Strašík. Supporting routines for the srim code. *Nuclear Instruments and Methods in Physics Research Section B: Beam Interactions with Materials and Atoms*, 257(1-2):601–604, 2007.

[37] Mirion Technologies. Passivated Implanted Planar Silicon Detectors. `https://www.mirion.com/products/passivated-implanted-planar-silicon-detectors`.

[38] Terry L Alford, Leonard C Feldman, and James W Mayer. *Fundamentals of nanoscale film analysis*. Springer Science & Business Media, 2007.

[39] Lawrence Ruby. Further comments on the geometrical efficiency of a parallel-disk source and detector system. *Nuclear Instruments and Methods in Physics Research Section A: Accelerators, Spectrometers, Detectors and Associated Equipment*, 337(2-3):531–533, 1994.

[40] Glenn M Torrie and John P Valleau. Nonphysical sampling distributions in monte carlo free-energy estimation: Umbrella sampling. *Journal of Computational Physics*, 23(2):187–199, 1977.

[41] Richard C Larson and Amedeo R Odoni. *Urban operations research*. Number Monograph. 1981.

Institute for nuclear and radiation physics
Celestijnenlaan 200D
3001 LEUVEN, BELGIË
tel. + 32 16 32 72 63
www.kuleuven.be